A STUDY ON PRODUCTIVITY ENHANCEMENT IN HIGH-SPEED, HIGH-PRECISION MICROMILLING PROCESSES

A Dissertation
Presented to
The Academic Faculty

By

Angela A. Sodemann

In Partial Fulfillment
Of the Requirements for the Degree
Doctor of Philosophy in Mechanical Engineering

Georgia Institute of Technology

December, 2009

A STUDY ON PRODUCTIVITY ENHANCEMENT IN HIGH-SPEED, HIGH-PRECISION MICROMILLING PROCESSES

Approved by:

Dr. J. Rhett Mayor, Advisor
School of Mechanical Engineering
Georgia Institute of Technology

Dr. Shreyes Melkote
School of Mechanical Engineering
Georgia Institute of Technology

Dr. Charles Ume
School of Mechanical Engineering
Georgia Institute of Technology

Dr. Jan Shi
School of Industrial and Systems Engineering
Georgia Institute of Technology

Dr. Burak Ozdoganlar
School of Mechanical Engineering
Carnegie Melon University

Date Approved:
11/16/2009

ACKNOWLEDGEMENTS

I would like to thank my colleagues Alex Williams, Andrew Semidey, Jacob Kunz, and Suzanne Price whose unfailing encouragement and friendship has brought joy to my work.

I am grateful to my committee: Drs. Melkote, Ume, Shi, and Ozdoganlar, whose willingness to contribute their time, effort, and thoughtful consideration has made this thesis possible.

I would like to express my heartfelt gratitude to my advisor, Dr. Rhett Mayor, whose skillful guidance has directed both my educational attainment and my personal growth during the course of this research.

Finally, I am grateful to my family: Mom, Dad, Steve, and Jon whose love and support continues to inspire me to pursue my goals.

TABLE OF CONTENTS

LIST OF TABLES

LIST OF FIGURES

Summary

This thesis presents a study into the enhancement of productivity in micromilling processes by considering a fundamental treatment of tool path trajectory generation techniques and process optimization strategies that account for the impact of scale effects present in high-speed, high-precision micromachining operations. Micromilling is increasingly applied to the production of a wide variety of micro components, due to its high precision and flexibility. However, the productivity of micromilling is limited by the low feedrates necessitated by the inherent high precision and small feature size. In this study, several scale effects present at the microscale are identified, in particular the increase of the ratio of tool size to feature size, and the corresponding impact on trajectory generation and process optimization is investigated. The scale effects are shown to cause increased geometric error when the standard method of VF-NURBS is applied to microscale feedrate optimization. The method of Enhanced Variable-Feedrate NURBS (EVF-NURBS) is proposed and shown to successfully compensate for the scale effects leading to reduced geometric error. A key contribution of this study is the construction and experimental validation of the Variable-Feedrate Intelligent Segmentation (VFIS) method for increased feedrates and improved stability. The VFIS method provides a cutting time reduction of more than 50% in some cases, while effectively constraining geometric error. Two tool size optimization schemes are presented for maximizing productivity and minimizing geometric error while accounting for dynamic effects uniquely present at the microscale. Finally, the development of a low-cost, high-precision micro-mesoscale machining center (mMC) is presented.

Chapter 1: Introduction

As miniaturization of products continues to progress in many industries and the broad adoption of miniaturization in consumer products continues to accelerate, the capability to manufacture these miniature products must progress as well in order to meet the growing demand. Since the introduction of the micro-factory concept in the early 1990's by the Japanese MicroFactory Program [1], the field of micro-manufacturing has grown substantially. This research activity has been in response to the need for increased production of micro/meso-scale components and products resulting from the rapidly escalating trend towards increased product miniaturization. The broad scale adoption of miniaturization in the consumer electronics, optics, telecommunications, robotics, defense, and in particular the bio-medical industries is the dominant driver for the increased demand.

Many methods of micromanufacture have been researched and applied to the manufacture of microcomponents. Some common methods of micromanufacturing include micro-EDM, micro-molding, micro-laser ablation, and micro-mechanical machining processes such as micro-turning and micro-milling. Some of the non-mechanical methods have shown promise for mass-production of micro components. However, micro-EDM and micro-molding both require the manufacture of complicated molds or electrodes that must be manufactured by other methods. Micro-laser ablation is limited in the precision that can be achieved by laser pulse duration. Given these drawbacks, micro-mechanical machining methods have shown themselves to be attractive alternatives. These methods can be used to manufacture the molds required

by non-mechanical methods, and have the potential to be useful in mass-manufacture of complex 3D shapes.

Micromanufacturing research has established the feasibility of microscale mechanical machining processes, performed on micromachine tools, as a manufacturing process technology that is capable of addressing the need for the mass production of miniature products and micro/meso-scale components [1, 2]. A survey of global micromachining technology development conducted in 2006 by the World Technology Evaluation Center revealed wide acceptance of micromachining processes as a viable alternative to typical photolithographic and micro EDM processes for microscale component production [2]. Among the micro-mechanical machining methods, micromilling is the most versatile, with the potential for 5 or more axes allowing for the accurate manufacture of complex parts. Micromilling is the preferred method of production for various complex 3D components, such as tooling inserts for microinjection molding [3], and efficient mass-production of various miniature products [1].

Because of the versatility inherent in milling processes and the productivity enhancements provided by improvements in speed and precision, high-speed, high-precision macromachining is now pursued in many industries, including the aerospace, mold and die, and auto industries. Micromilling processes benefit from the same versatility as macromilling. With similar improvements in speed and precision, micromachining has the potential to become a fast and accurate method of production for some high-demand products, such as lenses for small cameras [2].

The primary drawbacks of micromilling as a production method are the relatively high cost, and low productivity of the process. Productivity in micromilling operations, as in

macroscale machining, is simply measured as the rate at which acceptable, high-quality components are produced by the process. The high cost in micromilling is primarily due to short tool life and high cost of machining centers and tools. Low productivity is due to low material removal rates that are limited by the scale of the cutting tool and low feedrates. The typical range of cutting tools for micromilling operations is bounded by a generally accepted upper bound of 1 *mm* diameter, above which the process is no longer considered micro-scale, and the lower bound of 0.005 *mm* [4], which is the smallest commercially available end mill cutter. Tool size is ultimately limited by current cutting tool manufacturing capability. Feedrates in micromilling processes are necessarily low due to limitations on spindle speed imposed by existing spindle technology, coupled with limitations on chipload due to the decrease of stiffness and strength of the cutting tool with decreasing tool diameter.

Due to the inherently high precision level required at the microscale, enhancement of productivity ultimately leads to the need for high-speed, high-precision micromilling processes. Functional decomposition of the high-speed, high-precision objective establishes the following critical functions that must be successfully implemented in high-speed, high-precision micromilling processes: a) optimization of process parameters, b) minimization of cutting instability, and c) accurate and efficient generation of tool-paths that maintain specified precision requirements.

1.1 Optimization of Process Parameters

Values for process parameters must be determined for maximal productivity. These parameters include spindle speed, chipload, and axial and radial depths of cut. Values

for these parameters can be determined empirically, from recommended values [5], or by optimization. Optimization can be carried out for many different possible objectives. Dimov, et al. [3] considered machining strategy to be of utmost importance in the micromilling process optimization. In Dimov's study, machining strategy was chosen for optimal surface finish. In an optimization study by Carpenter and Maropoulos [6], tool size was considered as an optimization constraint that the tool must fit in all features. The determination of optimal values for chipload is primarily an objective for maintaining stability of the chip formation, or cutting, process.

1.2 Minimization of Cutting Instability

Stability of the cutting process at the microscale is widely recognized to be dependent on adherence to the minimum chip thickness requirement [7-10]. For feeds below the minimum chip thickness, the process is dominated by plowing and rubbing mechanics which lead to intermittent chip formation and can cause dynamic instability. For minimal error, it is vital that the process not pass into the plowing/rubbing operating region even for a short time, to avoid the vibrations caused by large perturbations in the cutting force as the minimum chip thickness boundary is crossed [7]. These vibrations may be severe due to reduced stiffness in the tool at the microscale, leading to vibrational amplitudes that approach the magnitude of minimum chip thickness [8]. This effect causes the actual cut surface to differ significantly from the desired surface [11]. Furthermore, these vibrations will continue as the uneven cut becomes the cutting surface for the next tooth pass [9, 10]. In order to avoid these detrimental effects, the minimum chip thickness requirement must be maintained over the entire tool path.

Chip thickness is an instantaneous quantity which varies sinusoidally during a single cutting pass of a tooth. In full-slotting operations, the chip thickness will vary from zero at the tooth entrance, to maximum at a rotational angle of 90°, back to zero at 180°. Here, the term 'chip thickness' will be used to refer to the maximum chip thickness during a tooth pass, corresponding to a rotational angle of 90°.

Since chip thickness decreases as feedrate decreases, the minimum chip thickness requirement imposes a minimum bound on feedrate for stable operation. The minimum chip thickness, t_{min}, depends on many factors, including tool and workpiece materials and other cutting conditions [8]. However, t_{min} can be estimated to depend exclusively on tool cutting edge radius, r_e, as in Eq. (1) [8, 12].

$$\frac{t_{\min}}{r_e} \approx 0.3 \tag{1}$$

Using the conventional chip-load calculation establishes an inequality determining the minimum allowable feedrate for stable cutting mechanics in terms of spindle speed *N*, feedrate *f*, number of teeth *n*, and minimum chip thickness. This inequality is shown in Eq. (2).

$$t_{\min} = \frac{f}{nN} > 0.3 r_e \tag{2}$$

1.3 Tool Path Generation

The improvement of tool-path generation has been identified as a key objective necessary for the advancement of micromilling technology [13], and will be specifically addressed in this research. This step defines the length, shape, and method of representation of the path which the tool must traverse, as well as the trajectory

generation necessary to follow the path. Length of the path is integral to productivity because it defines the distance the tool must travel. Shape is also significant because shape defines the acceleration profile for the tool path. Tool path representation and trajectory generation have control implications for precision. A key aspect of productivity, therefore, is to generate a tool path that allows for both high precision and high material removal rate.

Precision can be defined as the constraining of process error to within acceptable bounds. Two sources of error, chord error and interpolation error, become dominant in high-speed micromilling due to the high feedrates, small features, and limitations on the servo control loop update rate. These two sources of error are illustrated in Figure 1.1.

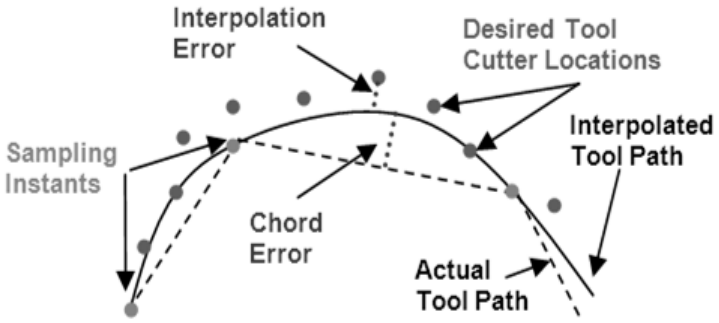

Figure 1.1: Two primary sources of error, interpolation error and chord error, relative to desired tool cutter locations

Chord error was first defined Stoker in 1969 [14], then later applied to milling processes by Sun, et al in 2006 [15]. According to these sources, chord error is defined as the maximum Euclidean distance between the interpolated tool path and the linear segments of the actual tool path. The amount of chord error incurred is dependent upon the radius of curvature of the interpolated tool path and the length of the corresponding actual tool path segment. The length of the actual tool path segment is proportional to

the trajectory generation loop update rate and feedrate during the time between sampling time nodes. Decreased radius of curvature of the tool path, decrease of feature size, decrease of trajectory generation loop update rate, and increase of feedrate all contribute to increased chord error. As a result, increasing feedrate and decreasing chord error are mutually exclusive objectives.

Interpolation error is defined as the Euclidean distance between the actual desired cutter locations and the interpolated tool path defined by a parametric description of the desired cutter locations, as illustrated in Figure 1.1. The parametric description of the tool path need not be limited to one parametric equation, and can include multiple equations defined across specified domains of the parameter space. Interpolation error can be reduced by obtaining higher-order parametric equations or decreasing the length of individual segments.

The tool-path generation objective consists of three stages: (a) tool-path construction, (b) vector fairing, and (c) CNC code generation.

The tool-path construction stage consists of identifying an ordered set of position vectors as the desired cutter location (CL) vectors required to produce the specified part geometry. This is typically done by offsetting the part geometry either along the normal vector at each point, or along the vector normal to a 4-point plane at each point [16]. Once a set of desired cutter location vectors has been identified, the CL vectors are 'faired' to remove or change regions which will have undesirable results, such as regions of undercut or gouging. Fairing is often accomplished by identifying points where the cutter location path crosses itself and then truncating the loop that is defined by the intersection in the tool-path. Zhang, et al. [17] proposed a fairing method in which

curvature is used to identify points which exceed limits of acceleration and jerk. Curvature specifications determined from acceleration and jerk limits are applied to calculate new CL vectors to replace the points that have violated the acceleration and jerk limits. The new points are chosen to approximate the original points as closely as possible without violating specified maximum acceleration and jerk limits.

The final step in tool path generation is the generation of CNC code. The research presented in this thesis will focus particularly on this aspect of tool path generation. This step consists of three components: interpolation, segmentation, and feedrate optimization.

1.3.1 Interpolation

The primary goal of interpolation is to provide a parametric description of the desired cutter location points which approximates the required workpiece geometry, accounting for tool offsets, with acceptable shape fidelity with a minimal set of parametric equations. A parametric description of the cutter location points is necessary for implementing the desired tool-path on a CNC machining center. The parametric description may consist of a single parametric equation or many parametric equations, depending on the interpolation method employed, the interpolation accuracy required, and the complexity of the geometry. Fewer equations are desirable in order to decrease CNC code length, thus reducing data transmission errors and lost data due to noise perturbation [18]. Additionally, a long CNC code typically results from many very short segments. This is undesirable due to discontinuities which occur between segments and due to the reduction in feedrate necessary to accurately track a rapidly-changing parametric

description. Good shape fidelity of the interpolation is critical in order to reduce error due to interpolation in the final product.

Three interpolation methods most commonly employed are linear/circular interpolation, polynomial spline, and more recently, the non-uniform rational B-spline, or NURBS, method. Linear/circular interpolation, or "reference word interpolation" [19], is the most common method of the three, due to its computational simplicity [20], however, the low order of linear and circular equations results in a large number of equations (segments) required for a parametric description of the tool path. There has been a move away from use of this type of interpolation, due to the required large data file [21], feedrate fluctuation between segments [22], slow implementation due to the large number of segments [23], and large amounts of interpolation error in some cases [24]. Polynomial spline interpolation, typically third or fifth order, is commonly employed because of the simplicity in implementation [25]. The NURBS method is able to represent closed or high-order curves with a high degree of continuity with a single line of NC code, and may be applied either as a method of extrapolation or interpolation [20]. Use of a single parametric description of the entire tool path results in minimal CNC code length requiring less memory in the CNC system [25-27]. The NURBS method is also known to allow high feedrates and be computationally stable [26].

Despite these key advantages of NURBS, there exist specific limitations in the approach that must be considered. A NURBS equation can be an overly complex description of the desired path. For example, a NURBS definition of a circle requires 38 parameters, while a circular interpolation block requires only 7 parameters by using a center, radius, and normal vector [20]. As a result of this excessive complexity, a NURBS equation

requires additional time for real-time computation of trajectory vectors during the machining process.

NURBS and polynomial spline interpolation have an additional drawback, in that these types of curves must be parameterized by arc-length in order to reduce feedrate fluctuation along the path. Parameterization by time, or other variable, does not provide for control of the feedrate, since arc length between values of the parameterization variable along the path is unknown. For feedrate control, the distance between consecutive equation evaluation points must be known. Thus, parameterization by arc-length is necessary. Due to the complex, nonlinear nature of both NURBS and polynomial splines, the process of parameterization by arc-length with these methods introduces additional interpolation error and increases the computation time [28]. Arc-length parameterization is straightforward with linear/circular interpolation, since arc-length of a line/circle is well-defined. Thus, no new error or computation time is introduced by arc-length parameterization for linear/circular techniques.

It is possible to interpolate an entire tool path with a single line of CNC code with the NURBS method. However, this is usually not possible with polynomial spline or linear/circular interpolation. A closed or high-order curve cannot be interpolated with a single polynomial spline. The capability of the NURBS method to interpolate a high-order curve with minimal interpolation error has resulted in the wide popularity of this method.

1.3.2 Segmentation

In the case that the tool path is too complex to be interpolated to within interpolation error tolerance limits with a single parametric equation, the set of tool cutter locations must be divided into smaller groups prior to interpolation [20]. This common method of interpolation error reduction is known as 'segmentation.' Because one equation is necessary for each segment, a larger number of segments results in lower interpolation error. However, a larger number of segments also results in a larger CNC code, and consequently the disadvantages discussed previously.

There are several common segmentation methods. The most common method is to determine segmentation limits by some form of numerical optimization. This can be done either by a numerical procedure such as Breyden's method [29], which is an offshoot of the secant method or, more commonly, by iterative, gradient descent techniques to reduce segmentation error to the set tolerance [30, 31]. Another common segmentation scheme is to distribute the segmentation limits evenly along one axis [32, 33]. At the completion of the segmentation process, each segment is individually interpolated.

1.3.3 Feedrate Optimization

After segmentation and interpolation are completed, the final component necessary to generate CNC code is to determine feedrate. The objective of maximizing feedrate is popularly pursued due to the advantages of achieving high material removal rate. Maximizing feedrate within error bounds along the tool-path is typically achieved through a method known as feedrate optimization. Feedrate optimization techniques have been

extensively studied at the macroscale and are well-documented in the literature [15, 32, 34, 35]. Feedrate optimization reveals that it is often necessary to reduce the feedrate in areas of high curvature in order to reduce chord error to within acceptable process tolerances. Yeh et al. [32] and Sun et al. [15] suggested varying feedrate based on radius of curvature in order to limit chord error to within a specified bounds. By imposing a limit on chord error, a varying maximum feedrate is established. Feedrate *f* is varied with radius of curvature *ρ*, sampling time *Ts*, and maximum allowable chord error $\delta_{\max}$, as shown in Eq. (3) [32].

$$f \leq \frac{2}{T_s}\sqrt{\rho^2 - (\rho - \delta_{max})^2} \tag{3}$$

The method of feedrate optimization according to Eq. (1) applied to NURBS-interpolated curves is known as the method of Variable-Feedrate NURBS. This method has been studied extensively for application to macroscale milling. New advancements in this method include the introduction of acceleration limiting and jerk limiting [24, 36, 37].

Typically for micromachining the allowable error must conform to high-precision, repeatability and accuracy requirements in the sub-micron range. Of the three components of tool path generation, the CNC code generation step is the least-well understood at the microscale and holds most promise for further advancement. This research will specifically address this aspect of micromilling.

1.4 Research Objectives

Productivity enhancement through tool path generation, optimization of process parameters, and minimization of cutting instability has been widely studied at the macroscale. However, productivity enhancement at the microscale has not been

sufficiently addressed due to poor understanding of the impact of scale effects in micromachining. These effects must be identified and incorporated into microscale productivity enhancement in order to sufficiently improve the process for feasibility of mass-manufacture of micro components. Specifically, the following limitations in the existing knowledge and research base will be considered in this study:

- Current methods of trajectory generation and parameter optimization are applicable at the macroscale only, and do not take into account key scale effects.
- Current methods of productivity enhancement do not take into account the avoidance of cutting instability that occurs at the microscale.

This research will seek to improve productivity in micromilling and fill the stated research gap by addressing the three primary objectives for productivity in micromilling: accurate and efficient generation of trajectories, optimization of process parameters, and minimization of cutting stability. The research presented in this thesis will specifically address the following four objectives:

Objective 1: To attain new knowledge which promotes increased understanding of key considerations for process optimization in high-speed, high-precision micromilling

Objective 2: To utilize new knowledge to develop new methods which can be applied to improve process optimization in high-speed, high-precision micromilling

Objective 3: To apply knowledge of scale effects in micromilling to develop a trajectory generation scheme which enhances productivity

Objective 4: To implement optimal parameters in a manner which is mechanically stable and robust, cost-effective, and industry-feasible

1.5 Hypotheses

It is hypothesized that scale effects affect the maximum productivity achievable in micromilling. In order to effectively perform trajectory generation for the microscale, these scale effects must be taken into account. A new method of trajectory generation for the microscale process is necessary. Trajectory generation algorithms have been developed and applied to macroscale process planning, and these methods have been applied in various software packages. These algorithms are targeted to macroscale milling processes without application of microscale considerations. A thorough understanding of these algorithms and the underlying models is necessary to identify shortcomings in application of the methods to the microscale.

Furthermore, it is hypothesized that feedrate optimization techniques developed for application at the macroscale are not applicable at the microscale due to the sensitivity of these techniques to scale effects. If this is so, then the optimal feedrate determined by application of existing methods is inaccurate when applied to the microscale. Productivity enhancement can then be achieved through the increased feedrates possible with modified optimization techniques.

Five hypotheses have been identified to be tested to achieve the previously-stated objectives:

Hypothesis 1: Trajectory generation methods applied to the macroscale do not apply to the microscale due to scale effects

Hypothesis 2: Existing feedrate optimization techniques are sensitive to scale effects.

Hypothesis 3: Enhanced optimization at the microscale can be achieved by incorporating key parameters which are sensitive to scale effects.

Hypothesis 4: Information contained within the tool path description can be utilized to enhance feedrate optimization.

Hypothesis 5: Tool path representation can be manipulated to enhance cutting stability.

1.6 Thesis Overview

In Chapter 2, scale effects will be identified which impact trajectory generation at the microscale. In Chapter 3, the scale effects will be applied in the creation of the new feedrate optimization method of Enhanced Variable-Feedrate NURBS as a modification of the current of Variable-Feedrate NURBS. The new method shows enhanced accuracy and applicability to the microscale in light of the scale effects. The scale effects will be applied in Chapter 4 in the derivation of a new segmentation algorithm, Variable-Feedrate Intelligent Segmentation, for trajectory generation at the microscale. An experimental evaluation of the methods of Enhanced Variable-Feedrate NURBS and Variable-Feedrate Intelligent Segmentation is presented in Chapter 5. The experimental evaluation process and results are presented. Chapter 6 will describe a preliminary investigation into microscale tool size optimization. Conclusions will be presented and future work will be outlined in Chapter 7. The Appendix describes the mechatronic enhancement of a low-cost micro mesoscale machining center employed in the experimental evaluation.

Chapter 2: Scale Effects Impacting Trajectory Generation in Microscale Milling

Microscale milling requires a marked reduction in tool size and part size relative to macroscale milling, with three orders of magnitude reduction in length scales being commonly encountered. In this chapter, this scaling will be examined to determine effects on precision and productivity. Three key scale effects will be identified. Initially, a modified definition of the term "feature size" is introduced to facilitate understanding of scale-related phenomena in micromilling. This modified definition is then applied in the derivation of the first key scale effect to be presented in this chapter: the increased ratio of tool-size to feature-size (Λ). This scale effect will be shown to impact the micromilling process through the introduction of tool-size error and by causing the convergence of the maximum and minimum feedrate limits. This convergence necessitates a modification of the traditional method of feedrate optimization. A second key scale effect is then presented: the increased significance of sampling rate at the microscale. Finally, the third scale effect: the impact of the geometry scaling factor on the rate of change of radius of curvature with respect to arc length ($\partial\rho/\partial s$) is derived.

2.1 Definition of Feature Size

Feature size is a term often used in micromanufacturing practice and literature as a measure of the difficulty of producing a feature and as a measure of the extent of miniaturization required to produce the feature. Thus, microscale features are considered to be features that are smaller than 1 *mm* [37]. Feature size is

conventionally defined to be the nominal dimension of a feature, such as the diameter of a circular protrusion or the width of a wall. Figure 2.1 is an illustration of the traditional understanding of the meaning of the term 'feature size'.

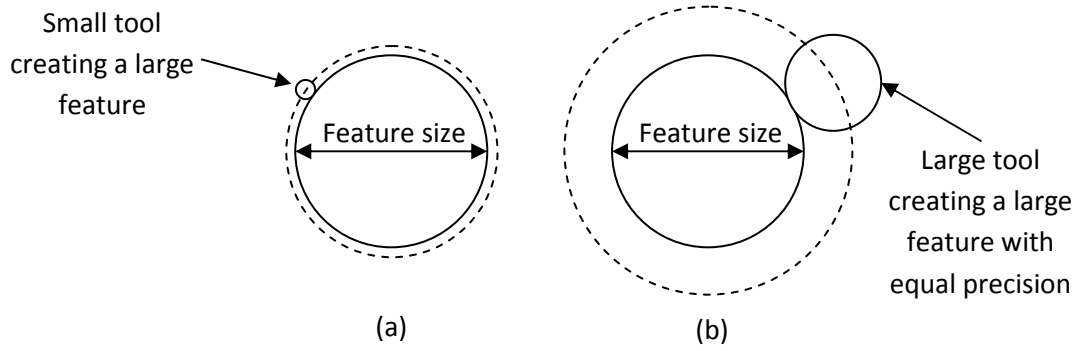

Figure 2.1: Illustration of the traditional meaning of the term 'feature size' as the diameter of a circular protrusion. With this understanding, precision is independent of tool size.

The nominal dimension definition of feature size accurately describes the extent of the precision and accuracy requirements necessary to produce the feature. A feature of 1 *mm*, for example, requires a positioning accuracy of 50 *μm* in order to produce the feature to within a 10% error limit, while a smaller feature of 1 *μm* requires a positioning accuracy within 0.05 *μm* in order to produce the feature within the same 10% error limit. However, this definition of feature size does not take into account possible tool size effects on error magnitude. A 1 *mm* feature of the conventional definition can be produced with equal accuracy given a 1 *mm* tool as with a 10 *mm* tool, providing that the positioning mechanism is sufficiently precise.

For microscale operations, in which the minimum feature size can be arbitrarily small, available tool size does not decrease arbitrarily with feature size, but is limited to a minimum of 5 *μm* [4]. Due to this limitation on tool size reduction, it is beneficial at the microscale to adopt a definition of feature size that takes into account the effect of tool

size on error magnitude. The limitation on tool size has significant effect on the magnitude of error along a target geometry in relation to tool-side radius of curvature. Sections of the geometry with large radius of curvature reveal little or no dependence of error on tool size, while sections with small tool-side radius of curvature exhibit much dependence of error on tool size. This phenomenon is illustrated in Figure 2.2.

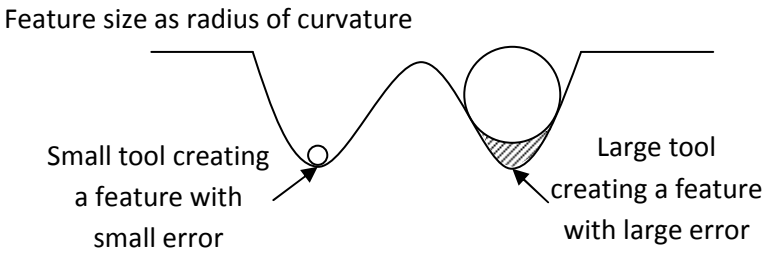

Figure 2.2: Illustration of the dependence of error magnitude on tool size and tool-side radius of curvature, leading to the use of tool-side radius of curvature as a revised definition of feature size

In order to express the significant dependence of error on tool size at the microscale, it is proposed that tool-side radius of curvature is a more useful definition of feature size for the purposes of micromilling analysis.

2.2 Increased Tool Size/Feature Size Ratio at the Microscale

For macroscale operations, in which the minimum feature size is 1 *mm*, tools ranging from 100 *mm* to 5 *μm* are available. For microscale operations, in which the minimum feature size can be arbitrarily small, available tool size does not decrease arbitrarily with feature size, but is limited to a minimum of 5 *μm* [4]. Figure 2.3 illustrates the range of tool sizes available at the macroscale and at the microscale.

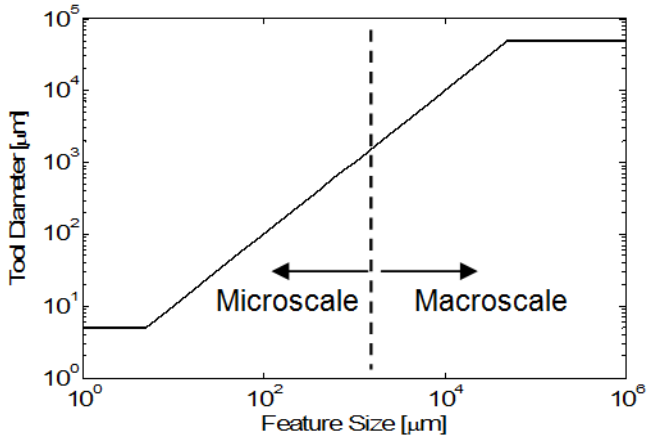

Figure 2.3: Scale effects impose a constraint on the available minimum tool size for micro-milling operations that is not encountered at the macroscale, conventional milling process

The value of r/ρ (Λ) at the macroscale can always be maintained at a near-zero value because of the range of cutting tools available. At the microscale, however, smaller tools are not available as feature size decreases near the tool diameter limit. This limit on tool size at the microscale causes the value of Λ to increase dramatically as feature size decreases to and beyond the 5 *μm* tool size limit. Because these operations with small features are considered microscale operations, the tool-size to feature-size ratio is much larger at the microscale than at the macroscale. Figure 2.4 demonstrates the trend of Λ as feature size decreases over the range of the macroscale and the microscale.

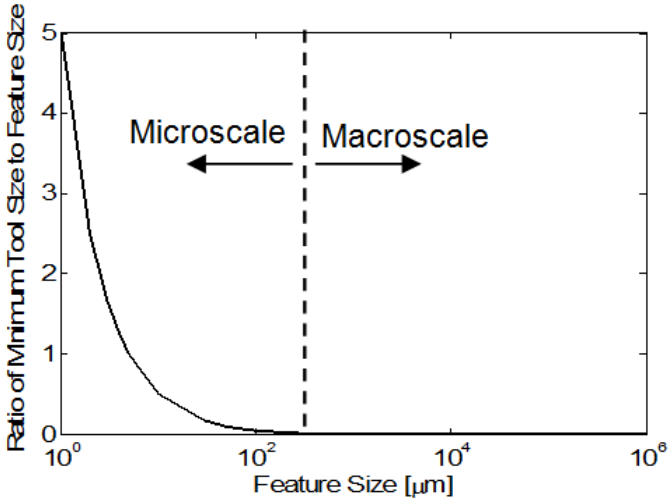

Figure 2.4: The ratio of tool size to minimum feature size becomes large at the microscale due to the limit on available tools and arbitrarily decreasing feature size.

2.3 Tool Size Error

The increase of Λ at the microscale causes several error-increasing effects. One effect is the possibility that a tool may not fit in the feature to be created, as illustrated in **Error! Reference source not found.**.

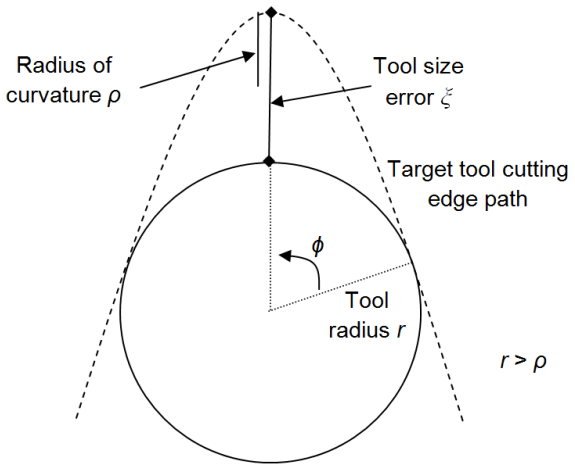

Figure 2.5: An illustration of tool size error resulting from a tool that is larger than the feature to be created

When this occurs, the cutting edge of the tool will either overshoot a portion of the desired curve or, if a gouge avoidance algorithm is in place, produce a large undercut, causing pronounced error. This type of error will be referred to in this paper as *tool size error*. This should be distinguished from the error source previously addressed by Tunea-Fatan et al. [38], and Liang et al. [39], which is caused by the changing angle of the tool from point to point on a 5-axis machine.

Tool size error can be calculated as the maximum distance between the desired tool cutting edge path and the cutting edge of the tool along the tool radius at the point where the radius is orthogonal to the desired tool cutting edge path. An analytical form for tool size error is presented in Eq. (1).

$$\xi = \rho + r\cos\phi\tan^2\phi - \frac{\rho}{\cos\phi} + r\cos\phi - r \tag{1}$$

Tool size error occurs only in locations where the tool radius is larger than the radius of curvature of the desired tool cutting edge path. This occurs when Λ is greater than 1. These locations can be identified as crunodes along the tool-offset path, or spindle path.

2.4 Modified Feedrate Optimization Inequality

Chord error calculation is affected by the high value of Λ at the microscale. Macroscale chord-error calculation techniques rely upon the assumption that the difference between the radius of curvature of the path of the spindle and the radius of curvature of the path of the tool cutting edge is negligible, given that the spindle path and the path of the cutting edge are arbitrarily close, as illustrated in Figure 2.6.

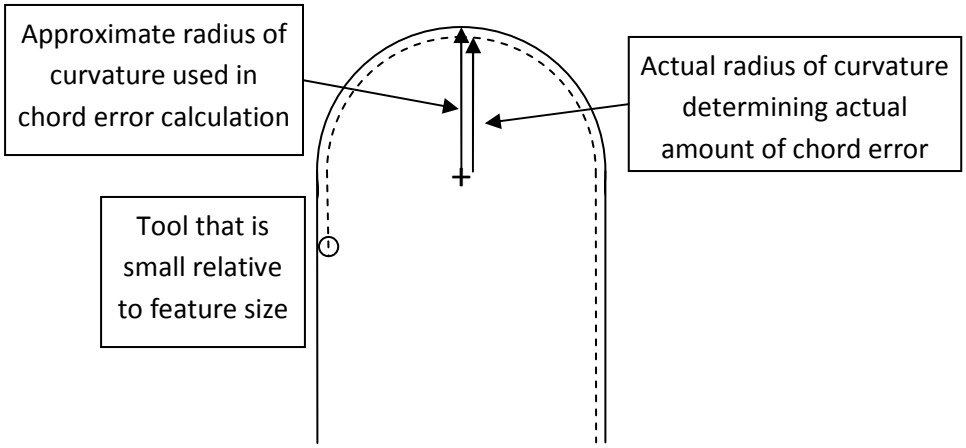

Figure 2.6: Approximate radius of curvature in relation to actual radius of curvature, valid at macroscale where Λ is small

This approximation is accurate when the value of Λ is small. When the ratio is high, however, the approximation is no longer valid, and consequently the conventional chord error calculations used at the macroscale are no longer accurate at the microscale. In this case, the radius of curvature of the path of the tool spindle is significantly smaller than the radius of curvature of the tool cutting edge. The error in radius of curvature approximation causes an error in chord length approximation. Chord error calculation, which is based on knowledge of chord length, is then in error as well. The difference between the sampling length approximation and the actual sampling length at the microscale is illustrated schematically in Figure 2.7. Since this difference is significant at the microscale, the chord error calculation techniques, and consequently the feedrate optimization approach utilized at the microscale must be adapted to consider the scaling effects.

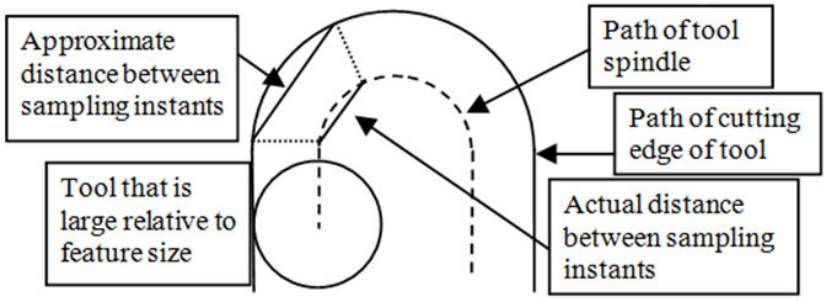

Figure 2.7: Difference between actual and approximate chord length becomes significant at the microscale, where Λ becomes large.

In accordance with the goals of minimizing error and minimizing dynamic effects, maximum and minimum limits of feedrate have been previously established in Sections §1.2 and §1.3, and are reported again in Eq. (2).

$$0.3 r_e n N < \hat{f}_E \leq \frac{2}{T_s}\sqrt{\rho^2 - \left(\rho - \delta_{\max}\right)^2} \tag{2}$$

Violation of the upper bound on feedrate will cause the allowable chord error to be exceeded, and violation of the lower bound will cause instability in the cutting mechanics and ultimately of the entire process. The bounds described in Eq. (2) are an accurate guide for operation at the macroscale. However, due to the high value of Λ at the microscale, Eq. (2) must be modified to account for the inaccurate chord error calculation. At the microscale, chord error must be calculated from the radius of curvature of the spindle path. Eq. (3) shows the modified version of the feedrate limitation for constrained chord error, assuming that positive radius of curvature is tool-side.

$$0.3 r_e n N < \hat{f}_E \leq \frac{2}{T_s}\sqrt{(\rho - r)^2 - \left((\rho - r) - \delta_{\max}\right)^2} \tag{3}$$

If positive radius of curvature is opposite tool-side, then the modified feedrate optimization equation is as in Eq. (4).

$$0.3r_e nN < \hat{f}_E \leq \frac{2}{T_s}\sqrt{(\rho + r)^2 - \left((\rho + r) - \delta_{\max}\right)^2} \tag{4}$$

2.5 Convergence of the Maximum and Minimum Feedrate Limits

A varying maximum feedrate is established by imposing a limit on chord error. Feedrate, f, is varied with radius of curvature ρ, sampling time T_s, and maximum allowable chord error δ_{max}, as in Eqs. (3) and (4). As radius of curvature and maximum allowable chord error decrease, maximum feedrate decreases. Furthermore, the size of the cutting edge radius does not scale proportionally with tool size. Consequently, the minimum chip thickness necessary for stable cutting mechanics does not reduce proportionately, resulting in the increase in the allowable minimum feedrate for microscale processes. At the macroscale, the lower feedrate limit is rarely approached, due to low spindle speeds and a cutting edge radius that is small relative to tool size.

Scale effects at the microscale cause a high minimum feedrate and a low maximum feedrate, to the extent that the minimum allowable feedrate may exceed the maximum allowable feedrate in certain regions of the process space. Figure 2.8 illustrates this occurrence as the ratio of tool size to feature size becomes large at the microscale.

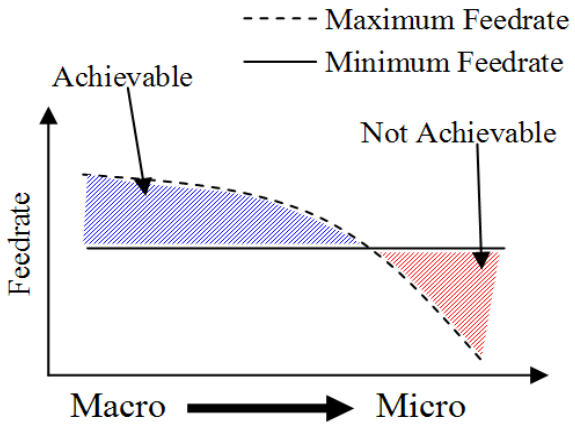

Figure 2.8: The maximum feedrate may fall below the minimum feedrate in microscale milling processes due to the presence of scale effects that increase the minimum feedrate

By inspection, the maximum allowable feedrate decreases significantly with increasing value of Λ. For microscale machining processes, where the value of Λ approaches or exceeds a value of 1 (ref. to Figure 2.4), the maximum feedrate is significantly lower than the maximum feedrate for equivalent processes where the value of Λ approaches 0, typically encountered in conventional, macroscale processing.

The minimum feedrate requirements in microscale process optimization are similarly impacted by scale effects. As a result of the marked reduction in scale of the cutting tool, the spindle speed in microscale processing must be increased proportionately to maintain sufficient surface speed for the cutting operation. The increase in spindle speed without decrease in cutting edge radius causes the minimum feedrate limit to increase.

A preliminary parametric study was conducted to investigate and quantify the feedrate constraints in microscale milling processes. The study considered the effects of three parameters: a) tool size to feature size ratio, b) spindle speed and c) cutting edge radius, on a full-slotting operation using a 50 *μm* two-flute endmill. Tool size to feature size ratio

was varied between 0 and 1 in increments of 0.1. Spindle speeds from 500,000 *rpm* to 1,000,000 *rpm* were considered, and the cutting edge radius varied between 1 *μm* and 5 *μm*. Although current spindle technology cannot reach these values, the need for such high-speed spindles has been recognized [13, 40] and is currently a popular thread of research [41-44]. The parameters for the study are shown in Table 2.1.

Table 2.1: Parameters tested to evaluate the convergence of maximum and minimum feedrate limits

Variable	Values
r [μm]	50
n	2
r_e [μm]	1,2,3,4,5
N [krpm]	500, 750, 1000
ρ [μm]	55.5, 62.5, 71.4, 83.3, 100
Λ	0.5, 0.6, 0.7, 0.8, 0.9

Figure 2.9 illustrates the trends of minimum and maximum feedrates with spindle speed and ratio of tool size to feature size across the domain of interest identified in the study. The converging feedrate trends result in regions in the process space at the microscale where the allowable maximum feedrate drops below the required minimum feedrate for stable chip formation, and the process becomes unstable.

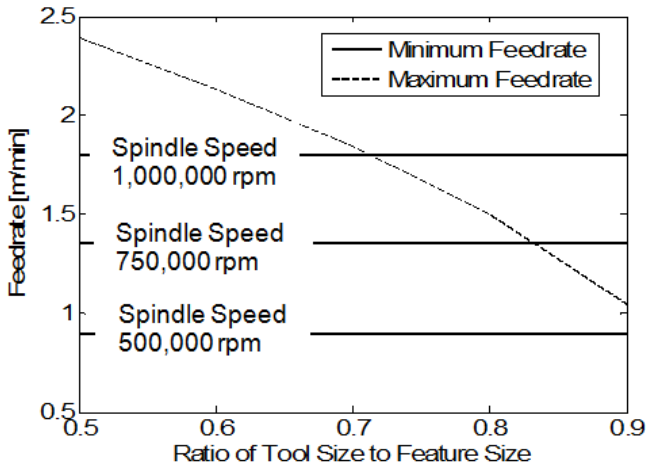

Figure 2.9: Minimum and maximum feedrate trends with ratio of tool size to feature size and spindle speed

Microendmills are prone to higher wear rates relative to macroendmills, adding additional complexity to feedrate optimization for microscale processes. Rapid tool wear has the same effect as increasing the cutting edge radius, resulting in the dynamic increase of the allowable minimum feedrate during the cutting process. As a result, if a feedrate is maintained near the lower-bound feedrate, the process may become unstable during the course of the operation as tool wear increases. Instability may begin during the operation, resulting from the minimum feedrate limit exceeding the maximum feedrate limit during the cut. The cutting edge radius of sharp microendmills have been estimated to range from 1-5 *μm* [45]. Assuming a value of 0.7 for Λ in the maximum feedrate calculation, minimum feedrate will exceed the maximum feedrate over the typical range of cutting edge radii, as illustrated in Figure 2.10.

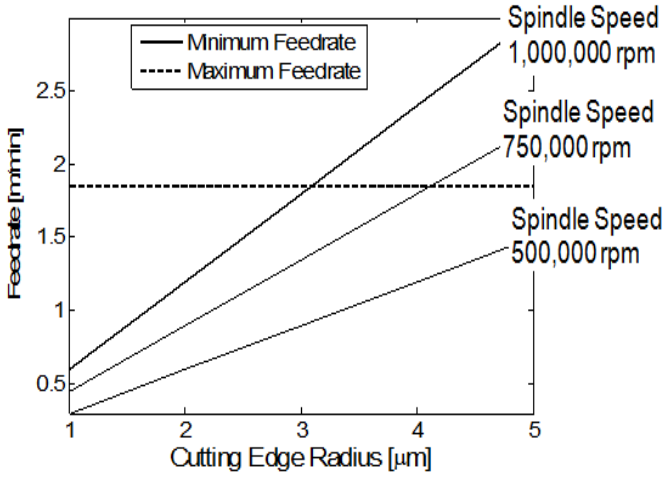

Figure 2.10: Minimum feedrate increases with increasing cutting edge radius as the tool wears.

In order to maintain stability and constrain error over segments in which the minimum feedrate and maximum feedrate converge, either the minimum feedrate must be lowered or the maximum feedrate must be raised. This can be achieved either by

reducing spindle speed or by increasing the sampling frequency (ref. Eq. (1)). Reduction of spindle speed may have the effect of unacceptably increasing surface roughness and will violate recommended surface speeds [5]. Therefore, this study proposes that the preferred solution is to increase the sampling frequency. However, both possibilities will be investigated. The solution of increasing sampling frequency to increase the maximum feedrate limit also results in increased productivity due to higher allowable feedrates.

2.6 Increased Significance of Sampling Rate at the Microscale

The dominant restriction on achievable sampling frequency is trajectory computation time [26, 46]. In order to increase the sampling frequency, trajectory computation must be made faster. Table 2.2 presents computation times for NURBS with various arc-length parameterization methods obtained by Cheng, et al. [46] and the computation time for circular interpolation calculated by the authors. The calculation for circular interpolation time was computed on a PC with a 3GHz Pentium 4 processor using Matlab software. The calculated time was then rounded up to the nearest tenth of a millisecond to determine the fastest achievable sampling rate. Note that computation time for circular interpolation is significantly faster than computation time for NURBS even when the simplified Taylor first-order approximation is made for arc-length calculation. As the NURBS arc-length calculation method becomes increasingly more accurate, required calculation time increases significantly. NURBS calculation with the Runge-Kutta arc-length approximation is more than 40 times slower than circular calculation. Note that where NURBS interpolation requires additional computation time for variable feedrate calculation, no additional calculation time is required for variable

feedrate calculation for circular interpolation. Since radius of curvature is constant along a circular segment, maximum allowable feedrate is constant (ref. Eq. (3)). These factors result in a much shorter allowable sampling time for segments interpolated with circular interpolation than for those interpolated with NURBS interpolation.

Table 2.2: Computation times for NURBS and circular trajectory generation

Interpolation Method	Computation Time [ms]	Variable Feedrate Calculation [ms]	Number of Function Calls	Sampling Time [ms]
Second-order NURBS with Taylor's first-order approximation [33]	0.350	0.200	161	1.0
Second-order NURBS with Taylor's second-order approximation [33]	0.900	0.330	483	2.0
Second-order NURBS with Runge-Kutta approximation [33]	1.450	NA	NA	3.0
Circular	0.030	0.000	1	0.1

The effects of sampling rate and increased Λ contribute together to reduce maximum feedrate, limiting productivity and exacerbating the problem of minimum/maximum feedrate convergence. Figure 2.11 illustrates this interdependence. The values in Figure 2.11 are based on a tool size of 20 *μm* with a maximum allowable chord error of 0.1 *μm*.

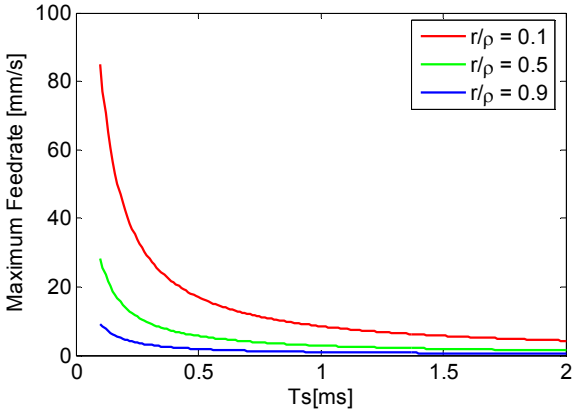

Figure 2.11: The maximum feedrate limit is lower for all values of Ts at greater values of Λ.

Figure 2.11 shows that the effects of increased sampling time on maximum feedrate are greater for greater values of tool size to feature size ratio. Thus, the effects of sampling rate on feedrate optimization must be considered in microscale operations, where Λ becomes large.

2.7 Impact of the Geometry Scaling Factor on $\partial p/\partial s$

In this section, the geometry scaling factor *a* will be introduced, and it will be shown that this factor causes a dramatic increase in the rate of change of radius of curvature with arc length. In Chapter 3, it will be shown that this increase causes inaccuracy in chord error estimation at the microscale, resulting in a failure of traditional feedrate optimization to constrain chord error.

A curve parameterized by arc length can be written as in Eq. (5). In this chapter and following, a single bar over a variable indicates a macroscale value, while a double bar indicates a microscale value.

$$\bar{\boldsymbol{x}}(s) = \{x(s), y(s), z(s)\} \tag{5}$$

Eq. (5) assumes a curve in 3-dimensional space, parameterized by arc length s. Radius of curvature along a curve parameterized by arc length is defined as the inverse of curvature, which is defined as the magnitude of the second derivative of the curve with arc length as in Eq. (6).

$$\bar{\rho}(s) = \frac{1}{\|\bar{\boldsymbol{x}}''(s)\|} \tag{6}$$

Eq. (5) is substituted into Eq. (6) to get Eq. (7).

$$\bar{\rho}(s) = \left(x''^2(s) + y''^2(s) + z''^2(s)\right)^{-1/2} \tag{7}$$

Then the derivative of radius of curvature with arc length is as in Eq. (8).

$$\frac{\overline{\partial\rho}}{\overline{\partial s}} = \frac{-\left(x''(s)x'''(s) + y''(s)y'''(s) + z''(s)z'''(s)\right)}{\left(x''^2(s) + y''^2(s) + z''^2(s)\right)\sqrt{x''^2(s) + y''^2(s) + z''^2(s)}} \tag{8}$$

Considering the geometry scaling factor *a*, a microscale version of the macroscale curve described in Eq. (5) can be simply formulated as shown in Eq. (9).

$$\bar{\bar{\boldsymbol{x}}}(s) = \{ax(s), ay(s), az(s)\}, \quad \textit{where} \quad 0<a<<1 \tag{9}$$

It will be shown here that the derivative of radius of curvature with arc length becomes large as the geometry scaling factor becomes small.

Eq. (9) is substituted into Eq. (8) resulting in Eq. (10), the derivative for the micro case.

$$\frac{\overline{\overline{\partial\rho}}}{\overline{\overline{\partial s}}} = \frac{-a^2\left(x''(s)x'''(s) + y''(s)y'''(s) + z''(s)z'''(s)\right)}{a^3\left(x''^2(s) + y''^2(s) + z''^2(s)\right)\sqrt{x''^2(s) + y''^2(s) + z''^2(s)}} \tag{10}$$

Thus, the relationship between the derivative of curvature at the macroscale and the derivative of curvature at the microscale is as in Eq. (11).

$$\frac{\overline{\overline{\partial\rho}}}{\overline{\overline{\partial s}}} = \frac{1}{a}\frac{\overline{\partial\rho}}{\overline{\partial s}} \tag{11}$$

Eq. (11) indicates that the rate of change of radius of curvature with arc length is much greater at the microscale than at the macroscale. Figure 2.12 illustrates that the magnitude of the rate of change of radius of curvature with arc length, independent of curve geometry, becomes large as the scaling factor *a* becomes small at the microscale.

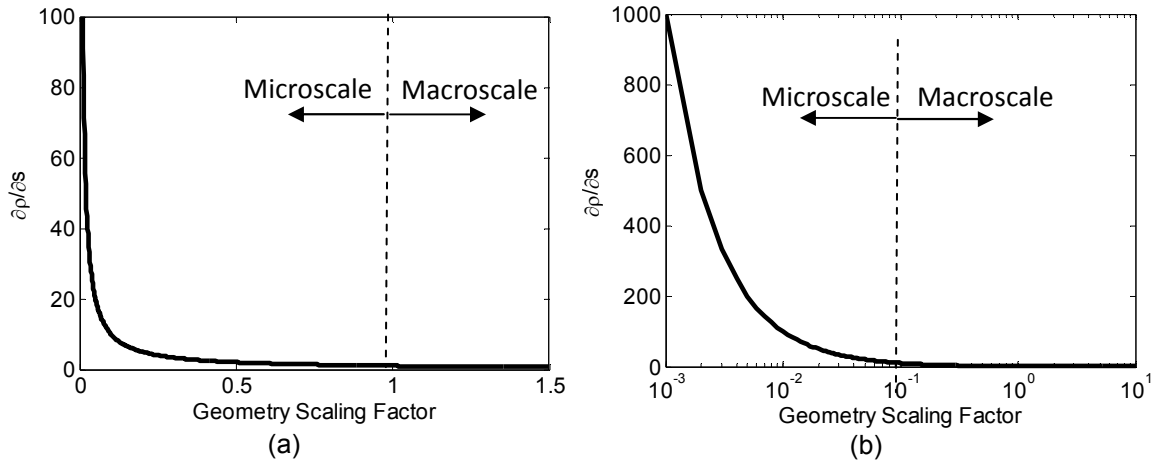

Figure 2.12: Relationship between ∂ρ/∂s and the geometry scaling factor at the microscale and the macroscale, shown against (a) a linear scale, and (b) a log scale

Summary

A revised definition of the term 'feature size' was introduced as the tool-side radius of curvature in order to account for tool size effects present in microscale processes. Three scale effects were identified which impact productivity at the microscale: the increase of Λ, the increased importance of sampling rate, and the increase of ∂ρ/∂s. The increase of Λ was shown to have significant consequences on microscale precision and productivity by causing tool size error and the convergence of the minimum and maximum feedrate limits. Sampling rate was shown to be limited by microscale trajectory generation, and the geometry scaling factor was shown to cause the significant increase of ∂ρ/∂s.

Chapter 3: Enhanced Variable-Feedrate NURBS Trajectory Generation Method

This chapter will examine the impact of two key scale effects: the tool size to feature size ratio, Λ, and the rate of change of radius of curvature with arc length, $\partial\rho/\partial s$, on the application of the conventional variable feedrate non-uniform rational B-spline (VF-NURBS) in microscale feedrate scheduling. These two scale effects, derived in Chapter 2, have a significant impact on the VF-NURBS feedrate optimization technique when applied to the microscale by effecting a marked increase in the inaccuracy of chord error calculation at this scale. As a consequence of the inaccuracy, the traditional method of VF-NURBS feedrate optimization fails to constrain chord error to within prescribed precision requirements. The Enhanced VF-NURBS algorithm (EVF-NURBS) will be presented that will be shown to compensate for the scale effects. The EVF-NURBS algorithm will be evaluated numerically and compared with the standard VF-NURBS algorithm. The numerical evaluation shows the capability of the EVF-NURBS algorithm to reduce miscalculation of chord error by as much as 56% relative to the standard algorithm.

3.1 Inaccuracy in Chord Error Calculation at the Microscale

In the conventional method of VF-NURBS, feedrate is calculated from the equation for maximum feedrate for limited chord error introduced in Chapter 1 and recalled here in Eq. (1).

$$\hat{f}_E = \frac{2}{T_s}\sqrt{\rho^2 - (\rho - \delta)^2} \tag{1}$$

However, the high values of Λ present at the microscale necessitate a modification to this equation. The modified equation for maximum feedrate for constrained chord error, *δ*, at the microscale derived in Chapter 2 is recalled in Eqs. (2) and (3).

$$\hat{f}_E = \frac{2}{T_s}\sqrt{(\rho - r)^2 - (\rho - r - \delta)^2} \tag{2}$$

$$\hat{f}_E = \frac{2}{T_s}\sqrt{(\rho + r)^2 - (\rho + r - \delta)^2} \tag{3}$$

An expression for chord error as a function of feedrate, radius of curvature, and tool size can be obtained from Eqs. (2) and (3) as shown in Eqs. (4) and (5).

$$\delta = \rho - r \pm 0.5\sqrt{(2\rho - 2r)^2 - f^2{T_s}^2} \tag{4}$$

$$\delta = \rho + r \pm 0.5\sqrt{(2\rho + 2r)^2 - f^2{T_s}^2} \tag{5}$$

For details on the derivation of the original chord error expressions, the reader is referred to the chord error derivation first given by Stoker in 1969 [14], then later applied to milling processes by Sun, et al in 2006 [15].

Eqs. (4) and (5) for chord error calculation rely upon the assumption that radius of curvature *ρ* is constant over the chord length covered during the duration of a sampling time. In regions of non-constant curvature, this assumption breaks down and the chord error calculation becomes inaccurate. An illustration of this effect is shown in Figure 3.1.

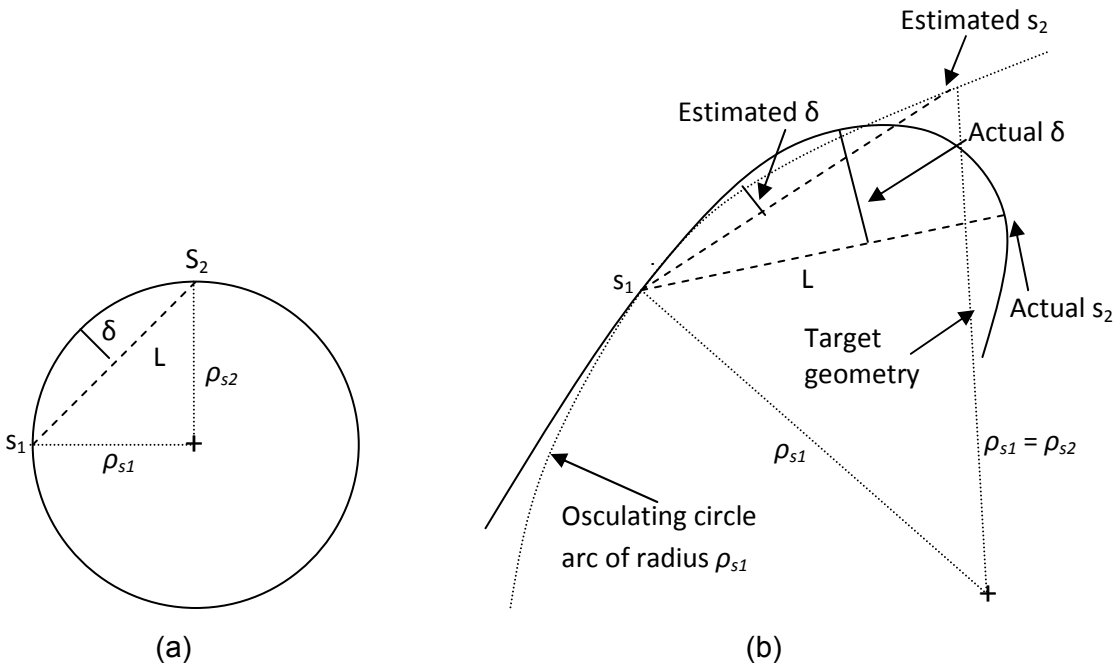

Figure 3.1: Calculation of chord error from estimated radius of curvature is correct for (a) a region of constant curvature but incorrect for (b) a region of varying curvature

Inaccuracy in the chord error calculation results in the inability of the VF-NURBS feedrate optimization method to effectively constrain chord error along the tool path. In such a case, actual chord error can far exceed the specified chord error limit. The discrepancy between calculated chord error and actual chord error becomes large in the application of VF-NURBS to microscale feedrate scheduling, due to the scale effects previously identified. Two independent effects cause this discrepancy: the increase of chord length at the microscale, and the increase of the rate of change of radius of curvature with arc length. This will be shown by comparing key quantities at the macroscale and the microscale. To facilitate this comparison, throughout this chapter a single bar over a variable will indicate the value for the macroscale case, and a double bar will indicate the value for the microscale case.

3.1.1 Impact of the Relative Increase of Chord Length at the Microscale

Figure 3.2 illustrates the relationship between chord error calculation inaccuracy and the chord length L. As the chord length becomes large as in Figure 3.2(a), the difference between estimated chord error and actual chord error also becomes large. The relationship between chord length at the macroscale and chord length at the microscale will now be derived in order to demonstrate the impact of the scale effects on the conventional VF-NURBS approach.

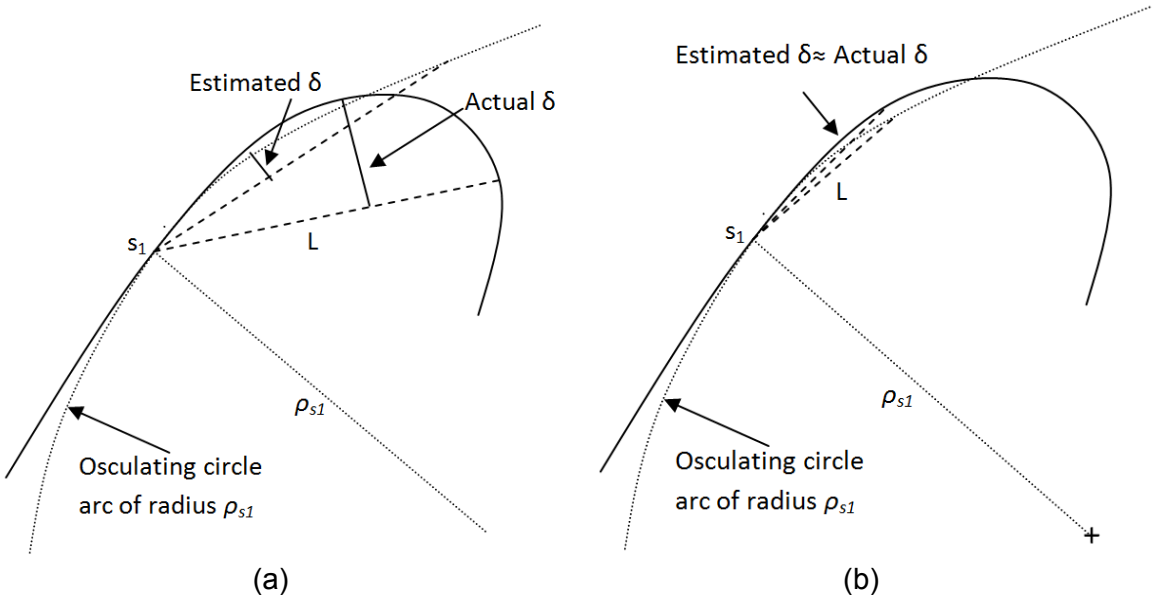

Figure 3.2: The error in the estimation of maximum chord error along the segment increases for (a) long chord lengths and is reduced with (b) short chord lengths

The length of the chord traversed by the spindle during one sampling instant is defined as the product of feedrate and sampling time as in Eq. (6).

$$L = fT_s \tag{6}$$

Sampling time is determined by control hardware, and therefore does not scale. Thus, Eq. (7) holds.

$$\overline{\overline{T_s}} = \overline{T_s} \tag{7}$$

For a given geometry, tool size, and sampling rate, chord error can be minimized by decreasing feedrate. Thus, minimum chord error is achieved with minimum feedrate. Consider the case in which the commanded feedrate equals the minimum feedrate. Minimum feedrate is the product of the minimum chip thickness, number of teeth, and spindle speed as shown in Eq. (8).

$$f = f_{min} = t_{c_{min}} nN \tag{8}$$

Microscale and macroscale relationships will now be derived for each value in Eq. (8) in order to determine the relationship between minimum feedrate at the microscale and minimum feedrate at the macroscale.

Minimum chip thickness depends upon many factors, such as workpiece material, but can be approximately defined as in Eq. (9) [8], where r_e is the cutting edge radius of the tool.

$$t_{c_{min}} = 0.3 r_e \tag{9}$$

Cutting edge radius does not decrease as tool size decreases, due to inherent limits on tool sharpening capability. Thus, cutting edge radius at the microscale and macroscale are equivalent as shown in Eq. (10),

$$\overline{r_e} = \overline{\overline{r_e}} \tag{10}$$

By combining Eqs. (9) and (10), it is determined that minimum chip thickness at the microscale is equal to minimum chip thickness at the macroscale.

$$\overline{t_{c_{min}}} = \overline{\overline{t_{c_{min}}}} \tag{11}$$

The minimum feedrate in Eq. (8) contains two additional parameters, number of teeth *n* and spindle speed *N*. Microtools and macrotools are both commonly constructed with 2 flutes, so that Eq. (12) holds.

$$\bar{n} = \bar{\bar{n}} \tag{12}$$

Micromilling spindle research continues to increase rotational velocities in an attempt to maintain cutting velocities between the macro and micro scales. Consider the case in which this has been achieved, as shown in Eq. (13).

$$\bar{v} = \bar{\bar{v}} \tag{13}$$

Cutting velocity is defined as in Eq. (14).

$$v = 2\pi r N \tag{14}$$

Microscale tool size can be considered to be a scaled factor of the macroscale tool, as in Eq. (15).

$$\bar{\bar{r}} = b\bar{r}, \qquad where\ \ b \ll 1 \tag{15}$$

Eqs. (14) and (15) are substituted into Eq. (13), resulting in Eq. (16).

$$2\pi\bar{r}\bar{N} = 2\pi b\bar{r}\bar{\bar{N}} \tag{16}$$

Eq. (16) reduces to Eq. (17).

$$\bar{N} = b\bar{\bar{N}} \tag{17}$$

A relationship between minimum feedrates at the micro and macro scales is then obtained by substituting Eqs. (11), (12), and (17) into Eq. (8) to arrive at Eq. (18).

$$\overline{f_{min}} = b\overline{\overline{f_{min}}} \tag{18}$$

Finally, the relationship between chord length at the macro and micro scales is determined by substituting Eqs. (18) and (7) into Eq. (6), giving Eq. (19).

$$b\bar{\bar{L}} = \bar{L} \tag{19}$$

Thus,

$$\bar{\bar{L}} \gg \bar{L} \tag{20}$$

The derivation culminating in Eq. (20) indicates that for minimum feedrate, the chord length traversed by the spindle during one sampling time at the microscale is much longer than at the macroscale.

Note that Eq. (20) is true for the case of minimum feedrate, but does not hold true for all comparisons of microscale and macroscale feedrates. For example, macroscale chord length is larger than microscale chord length if the maximum allowable feedrate is considered, since the maximum feedrate increases with decreasing Λ, as was presented in Chapter 2. However, if a large inaccuracy in chord error calculation is encountered for the case of maximum feedrate, the problem can be alleviated simply by decreasing the feedrate. At the macroscale, feedrate reduction is able to solve the problem of inaccurate chord error estimation because of the low value of minimum feedrate. At the microscale, however, the minimum feedrate becomes large and a different solution is needed.

3.1.2 Impact of the Increased Rate of Change of Radius of Curvature with Arc Length

A second scale effect presented in Chapter 2, the increase of $\partial\rho/\partial s$, further aggravates the inaccuracy of chord error calculation at the microscale. This effect is dependent only on the scale of the geometry, and is independent of feedrate.

Consider the case of a spindle following a desired spindle path as shown in Figure 3.3, in which the tool travels from point S_1 to point S_2 during sampling time Ts.

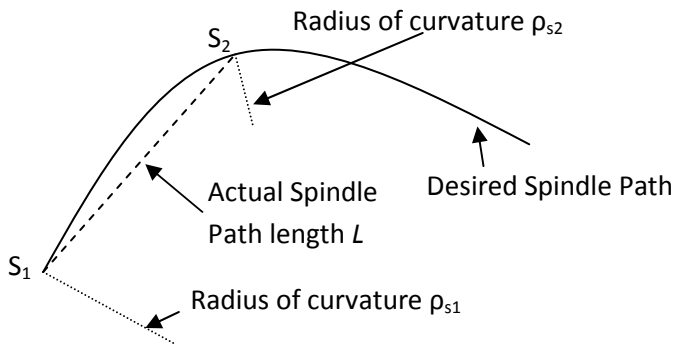

Figure 3.3: Difference in radius of curvature between two subsequent sampling points along a spindle path

The VF-NURBS chord error calculation relies upon the assumption that the radius of curvature of the tool path remains constant between the endpoints of the chord, S_1 and S_2. If this assumption breaks down, the chord error estimation will be inaccurate, resulting in additional error. This assumption is accurate at the macroscale, where $\partial\rho/\partial s$ is small between subsequent sampling instants S_1 and S_2. At the microscale, however, the assumption breaks down due to the high value of $\partial\rho/\partial s$.

The constant curvature assumption implies or, in fact, requires that the segment from S_1 to S_2 can be approximated as a circle segment of radius ρ_{s1} and arc length S_2-S_1. Although the actual amount of additional chord error resulting from the faulty constant-curvature assumption is curve-dependent, a measure of error magnitude can be considered to be the magnitude of the change in radius of curvature between points S_1 and S_2 (ref. Figure 3.1(b)).

Estimated chord error is a function of ρ_{s1}, while actual chord error is a function of radius of curvature at all points between S_1 and S_2. Thus, the approximate chord error, δ, approaches the actual chord error as $\partial\rho/\partial s$ goes to zero, as expressed in Eq. (21).

$$\delta_{\text{approximate}} \rightarrow \delta_{\text{actual}} \text{ as } \frac{\partial \rho}{\partial s} \rightarrow 0 \tag{21}$$

Recall from Chapter 2 that scale effects impact the derivative of radius of curvature as per Eq. (22).

$$\frac{\overline{\overline{\partial \rho}}}{\overline{\overline{\partial s}}} = \frac{1}{a}\frac{\overline{\partial \rho}}{\overline{\partial s}} \tag{22}$$

As a direct consequence of scale effects, the magnitude of change in curvature between successive sampling points along the curve becomes large at the microscale. The discrete form of Eq. (22) is shown in Eq. (23).

$$\frac{\overline{\overline{\Delta \rho}}}{\overline{\overline{\Delta s}}} = \frac{1}{a}\frac{\overline{\Delta \rho}}{\overline{\Delta s}} \tag{23}$$

Arc-length parameterization in the VF-NURBS trajectory-generation method utilizes the approximation in Eq. (24).

$$\Delta s = L \tag{24}$$

Eq. (24) is substituted into Eq. (23) to arrive at Eq. (25).

$$\frac{\overline{\overline{\Delta \rho}}}{\overline{\overline{L}}} = \frac{1}{a}\frac{\overline{\Delta \rho}}{\overline{L}} \tag{25}$$

Recalling the relationship in Eq. (20) and applying it to Eq. (25) gives Eq. (26).

$$\frac{\overline{\overline{\Delta \rho}}}{\frac{1}{b}\overline{L}} = \frac{1}{a}\frac{\overline{\Delta \rho}}{\overline{L}} \tag{26}$$

Then the relationship between change in radius of curvature at the macroscale and the microscale can be found by simplifying Eq. (26) as shown in Eq. (27).

$$\overline{\overline{\Delta \rho}} = \frac{1}{ba}\overline{\Delta \rho}, \qquad where\ b \ll 1\ and\ \ 0 < a \ll 1 \tag{27}$$

And therefore; $\overline{\overline{\Delta \rho}} \gg \overline{\Delta \rho}$

As *b* and *a* decrease at the microscale, inaccuracy in chord error calculation increases.

Eq. (27) was derived under the assumption of minimum feedrate for both the macro and the micro case. If the assumption is made of equal feedrate for both the micro and macro case, then the relationship does not depend upon the *b* factor, but depends only on the geometry scaling factor as shown in Eq. (28).

$$\overline{\overline{\Delta\rho}} = \frac{1}{a}\overline{\Delta\rho}, \quad where \ 0 < a \ll 1 \tag{28}$$

In the next section, a method is proposed for detecting and compensating cases of high inaccuracy in the chord error calculation.

3.2 Enhanced Variable-Feedrate NURBS (EVF-NURBS) Algorithm

This study proposes an Enhanced Variable-Feedrate NURBS method that accounts for unique requirements imposed by the scale effects. Due to the real-time nature of trajectory generation, the following restrictions are placed on the trajectory-generation algorithm:

(1) The algorithm must be minimally computationally intensive in order to minimize trajectory calculation time which is the dominant restriction on achievable sampling rate.

(2) The algorithm must not require multiple iterations of the calculation of point S_2 due to the highly time-consuming nature of the VF-NURBS method of trajectory generation.

(3) Calculation of point S_2 must be the final operation of the algorithm, since only a single iteration of calculation of point S_2 is allowed

Inaccuracy of the chord error calculation occurs because of an inaccurate estimation of the radius of curvature of a segment. The EVF-NURBS algorithm must make this estimation correctly. In application of feedrate optimization within regions of varying curvature, estimated radius of curvature and chord length cannot be decoupled. Therefore, the new algorithm must include a method of accurately estimating both chord length and the radius of curvature simultaneously. If the calculated chord length for constrained chord error is greater than the arc length over which estimated radius of curvature applies, the chord length calculation will be inaccurate.

The problem cannot be solved analytically, because an analytical expression for the radius of curvature of a NURBS curve as a function of arc length does not exist. Therefore, a solution method is proposed here in which a search is made for the chord length which equals the distance over which the estimated radius of curvature is valid. A look-ahead method is proposed to determine the point at which chord error calculation becomes inaccurate prior to establishing the point S_2. A flow chart of the proposed EVF-NURBS algorithm is presented in Figure 3.4.

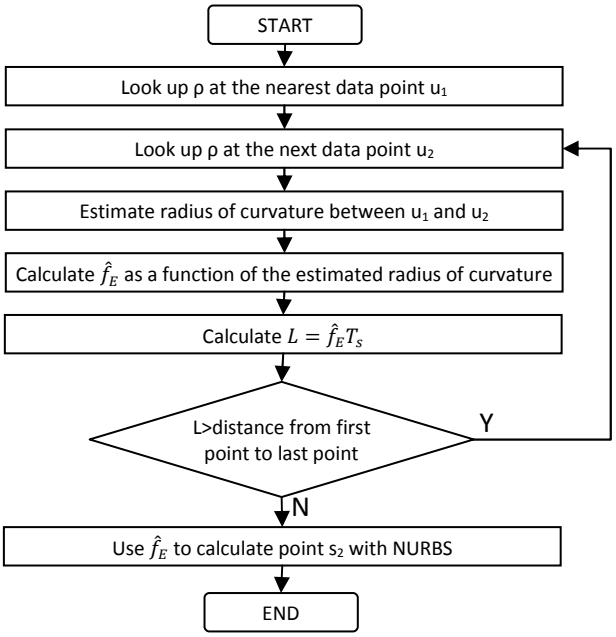

Figure 3.4: Flow chart of the proposed EVF-NURBS feedrate optimization method

This algorithm requires a method of calculating an estimated constant radius of curvature between the two test points u_1 and u_2. The most accurate method to make this estimation is to perform a circular regression over the segment. However, circular regression is a nonlinear problem that requires iteration as a component of the gradient descent method of error minimization. As a result, this process becomes time-consuming due to computational intensity. Furthermore, the number of calculations and, therefore, the time required to complete this computation depends upon the accuracy of an initial solution guess. Thus, the time cost of the regression is highly variable and unpredictable. For these reasons, circular regression is undesirable as a component of trajectory generation, which is a time-constrained real-time operation. It is proposed here that a sufficiently accurate estimation of radius of curvature can be made by computing the mean radius of curvature along the arc.

3.3 Numerical Evaluation of the EVF-NURBS Algorithm

The performance of the EVF-NURBS algorithm was evaluated numerically by considering the total deviation of the output of the trajectory generation from the ideal spindle path. By applying this measure of error, the difference between calculated and actual chord error can be determined and compared between the EVF-NURBS algorithm and the traditional VF-NURBS algorithm.

The geometry chosen for the ideal spindle path must have a well-defined radius of curvature in order that the minimum radius of curvature might be easily set. A geometry has a well-defined radius of curvature if the geometry can be expressed as a parametric equation which is two-times differentiable. This is a direct result of the definition of radius of curvature, defined in parametric form in Eq. (29).

$$\rho(u) = \sqrt{\frac{(\dot{x} \cdot \dot{x})^3}{(\dot{x} \times \ddot{x}) \cdot (\dot{x} \times \ddot{x})}} \tag{29}$$

A second requirement for the test geometry is that the radius of curvature should be continuously variable along the path, in order that the results of the test will be generally applicable. A sinusoidal geometry satisfies both of these requirements. Additionally, radius of curvature for a sinusoidal geometry can be easily set by choice of frequency. Frequency for a specified minimum radius of curvature is derived as follows.

Let the 2-dimensional sinusoidal geometry be defined in parametric form as in Eq. (30).

$$\{X, Y\} = \{u, A\sin(\omega u)\} \tag{30}$$

The radius of curvature at any parameter value *u* is defined as in Eq. (31).

$$\rho(u) = \sqrt{\frac{1 + A^2\omega^2 cos^2(\omega u)}{A^2\omega^4 sin^2(\omega u)}} \tag{31}$$

Eq. (31) is expanded, resulting in Eq. (32).

$$\rho^2 A^2\omega^4 \sin^2(\omega u) = 1 + 3A^2\omega^2 \cos^2(\omega u) + 3A^4\omega^4 \cos^4(\omega u) + A^6\omega^6 \cos^6(\omega u) \tag{32}$$

From Eq. (32), minimum radius of curvature will occur when sin(*ωu*) is equal to 1. Thus, let *ωu=π/2.* Then, Eq. (32) reduces to Eq. (33).

$$\rho_{min}{}^2 A^2\omega^4 = 1 \tag{33}$$

Eq. (33) is then solved for *ω*, giving Eq. (34).

$$\omega = \sqrt{\frac{1}{\rho_{min} A}} \tag{34}$$

Choice of amplitude *A* is arbitrary. For these tests, amplitude was set at *A* = 0.6530 *mm* in order to facilitate experimental validation by ensuring that the actual cutting edge of the cut geometry was contained within the Y-axis of the microscope field of view, reducing the amount of image processing necessary to evaluate the result. Two sinusoidal geometries have been chosen for the simulations. These geometries have different values of curvature and derivative of curvature, in order to evaluate the performance of the modified algorithm in light of the scale effects. Values of ρ_{min} were specified as 150 *μm* and 350 *μm* in order to represent typical values of Λ that might be encountered at the microscale. The amplitudes of *∂*ρ/*∂*s for these two geometries are 100 and 10, respectively. The two resulting sinusoidal geometries are reported in Eq. (35).

$$\begin{aligned} \{X, Y\} &= \{u, 0.653 \sin(3.195u)\} \\ \{X, Y\} &= \{u, 0.653 \sin(2.092u)\} \end{aligned} \tag{35}$$

Values for sampling rate and spindle speed have been chosen to represent projected future PC-based control technology, current real-time control technology, and current PC-based control.

In the current PC-based control setup, sampling rate has been set at 20.0 *ms*, representing the fastest sampling rate possible with a PC-based control system. This value was determined from tests on such a setup. The spindle speed for this setup is set at 80,000 *rpm* representative of a low-cost micromilling electric spindle currently commercially available. The spindle chosen for this setup is the NSK America electric spindle model E800Z.

The setup for current real-time control technology setup includes a sampling rate of 2.0 *ms*, representative of the length of time required to calculate a single VF-NURBS trajectory with current computation hardware. More information on this value was presented in Section §2.6. The spindle speed chosen for this setup is the NSK America high-speed air turbine spindle model HTS1501S with a speed of 150,000 *rpm*. For the future PC-based control technology setup, sampling rate has been chosen to represent two orders of magnitude improvement over the current PC-based control setup, and spindle speed one order of magnitude, representing the current research trend to develop a spindle capable of speeds in the range of 500,000-1,000,000 *rpm* [42, 47, 48].

Two values of allowable error have been chosen to represent high-precision and ultra-high-precision requirements as micron precision and sub-micron precision, respectively. The parameters for all tests to be performed are summarized in Table 3.1.

Table 3.1: Complete set of test parameters to be applied to the verification simulation of the EVF-NURBS trajectory generation. All tests were performed with a 100 *μm* tool.

Test #	Representative Technology State	ρ_{min} [μm]	Ts [ms]	N [rpm]	δmax [μm]
1	Future PC-Based	150	0.2	800,000	0.1
2	Future PC-Based	150	0.2	800,000	1.0
3	Current Real-Time	150	2.0	150,000	0.1
4	Current Real-Time	150	2.0	150,000	1.0
5	Current PC-Based	150	20.0	80,000	0.1
6	Current PC-Based	150	20.0	80,000	1.0
7	Future PC-Based	350	0.2	800,000	0.1
8	Future PC-Based	350	0.2	800,000	1.0
9	Current Real-Time	350	2.0	150,000	0.1
10	Current Real-Time	350	2.0	150,000	1.0
11	Current PC-Based	350	20.0	80,000	0.1
12	Current PC-Based	350	20.0	80,000	1.0

Figure 3.5 is a plot of chord error for Test 6, in which the feedrate limitation from chord error is dominant. This dominance is indicated in that the chord error reaches and exceeds the specified maximum (in this case, 1.0 *μm*) and then levels off. In this case, the EVF-NURBS algorithm provides a moderate benefit of 35.0% reduction in maximum chord error relative to the standard case.

The even-numbered tests have a relaxed chord error constraint, and so the chord error limitation becomes dominant only in the current PC-based control setup. In the current real-time and future PC-based setups, decreased sampling time causes the maximum chipload feedrate constraint to become dominant. Because the chord error feedrate constraint is not reached, conventional VF-NURBS does not fail in this case. This can be seen by examining the plots of chord error, in which chord error does not ever reach the specified limit. Figure 3.6 is a plot of chord error for Test 2, in which the specified chord error limit was set to 1.0 *μm*, but the maximum error value is only 0.1413 *μm*, because of the dominance of the chipload constraint.

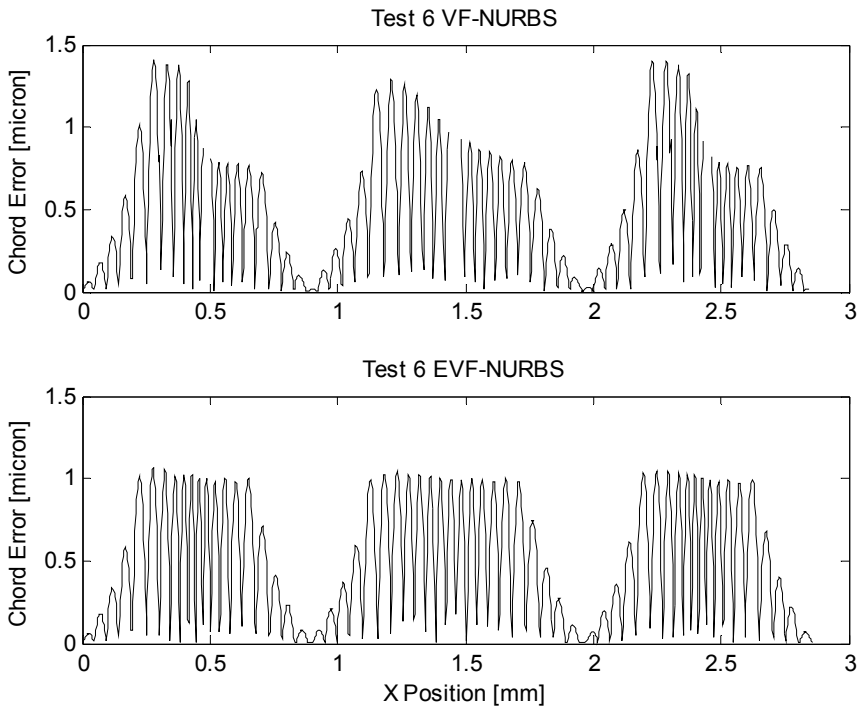

Figure 3.5: Chord error profiles for the standard and EVF-NURBS trajectory generation methods applied to a test sine wave geometry

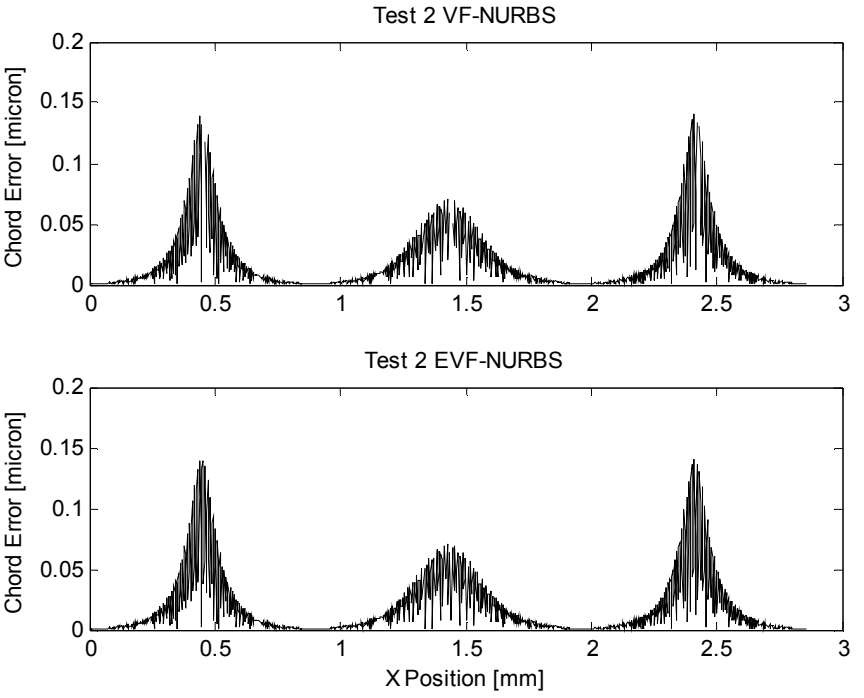

Figure 3.6: Chord error profile for a test in which the maximum chipload feedrate limitation is dominant. The results from both methods are within the specified chord error limit.

For all tests performed, the commanded trajectories were compared to the ideal tool-path to calculate chord error. The maximum values of chord error over the tool-path were calculated for each test case and are reported in Table 3.2 along with the amount of error reduction provided by the EVF-NURBS method relative to the standard VF-NURBS method.

Table 3.2: Results from the EVF-NURBS verification simulation, comparing error between the standard VF-NURBS and the EVF-NURBS algorithm for all tests

Representative Technology State	Maximum Chord Length [μm]	Test #	VF-NURBS Maximum Error [μm]	EVF-NURBS Maximum Error [μm]	Error Limit [μm]	EVF-NURBS Error Reduction [%]
Future PC-Based	10.6	1	0.1060	0.1027	0.1	3.3
		2	0.1413	0.1413	1.0	0.0
		7	0.0473	0.0473	0.1	0.0
		8	0.0473	0.0473	1.0	0.0
Current Real-Time	20.0	3	0.1104	0.1042	0.1	6.2
		4	0.4963	0.4963	1.0	0.0
		9	0.1057	0.1019	0.1	3.8
		10	0.1660	0.1660	1.0	0.0
Current PC-Based	106.6	5	0.1656	0.1098	0.1	55.8
		6	1.4120	1.0618	1.0	35.0
		11	0.1588	0.1074	0.1	51.4
		12	1.2377	1.0302	1.0	20.8

Table 3.2 indicates that the greatest benefit from the EVF-NURBS method occurs in the current PC-based setup, which has the largest value of the chord length $L=f*Ts$. In all cases tested, feedrate f is limited by two considerations: limited chord error and limited chipload. The chord error limitation is the same for all technology states, but the chipload limitation is different for the three cases because this limitation depends on spindle speed.

One aspect of the benefit of the EVF-NURBS method is the reduction of error in cases where the error exceeds the limit. In these cases, standard VF-NURBS under-estimates the radius of curvature and sets a feedrate that is too high and results in excess error. A

second aspect of the benefit is the increase of error in places where the error falls below the maximum. In these cases, standard VF-NURBS over-estimates the radius of curvature and sets a feedrate that is too low. The EVF-NURBS method equalizes both of these cases, reducing feedrates in the former error and increasing feedrates in the latter cases. Figure 3.7 shows both of these error cases. Under-estimation of chord error occurs in places of positive derivative of curvature, and under-estimation occurs in places of negative derivative.

The magnitude of deviation of the standard VF-NURBS chord error profile from the specified maximum limit is less in tests with smaller magnitude of derivative of curvature. This can be seen by comparing Figure 3.8 with Figure 3.7.

When the chord error limitation is dominant, as it is especially in the $\delta = 0.1\ \mu m$ cases (the odd-numbered tests) then the product *f*Ts* is larger by an order of magnitude for current real-time control relative to future PC-based, and an order of magnitude for current PC-based technology relative to current real-time control technology. The tests show a corresponding increase of error as the product *f*Ts* becomes larger for both the VF-NURBS and EVF-NURBS tests. The benefits of the EVF-NURBS method become large as *Ts* becomes large. Figure 3.9 is a plot of the percent error in the odd-numbered tests, and illustrates this trend.

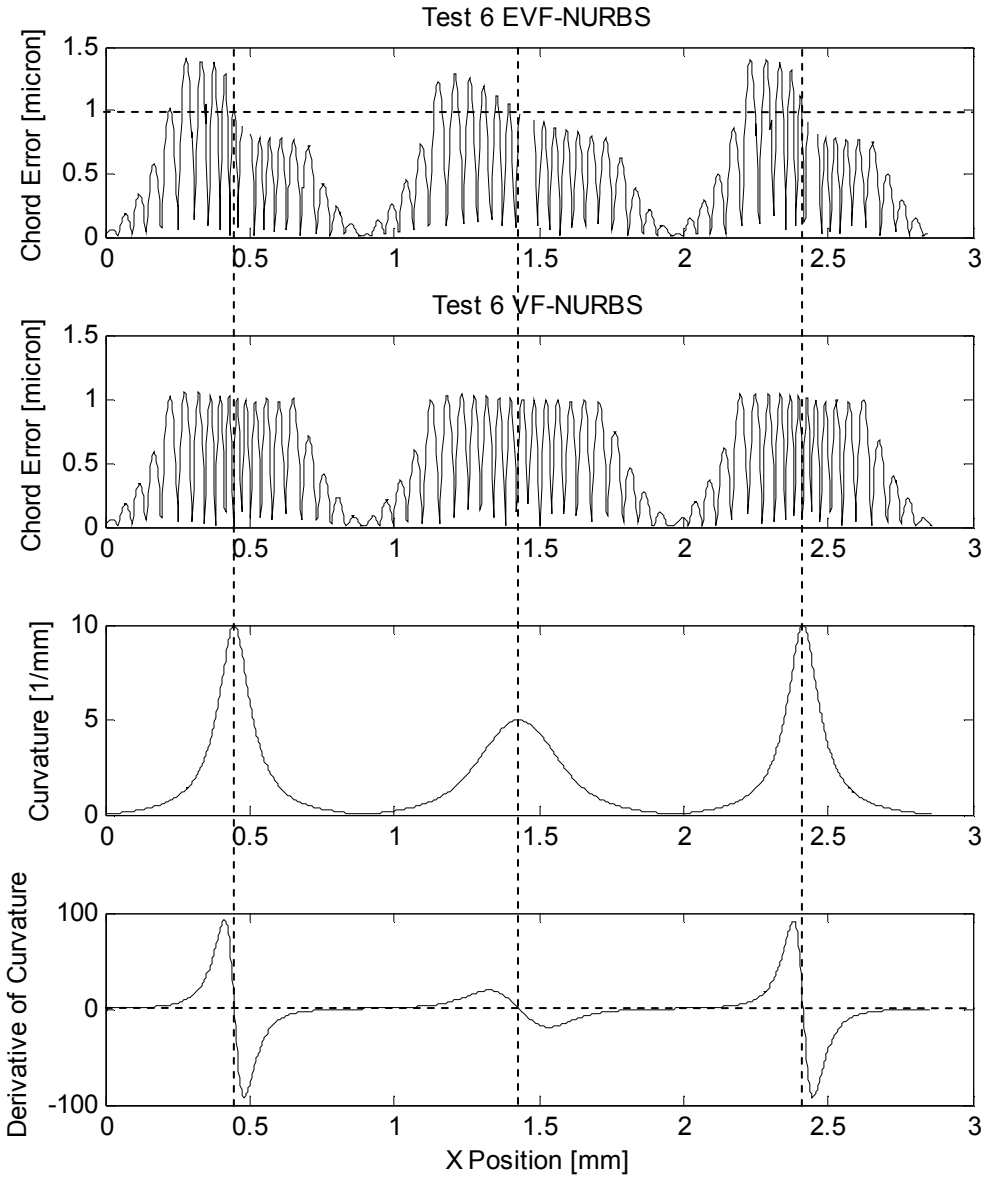

Figure 3.7: Results from Test 6, indicating that positive derivative of curvature causes an excess of chord error with the standard VF-NURBS method; negative derivative causes a decrease of error due to excessively decreased feedrate. The EVF-NURBS method equalized the discrepancies.

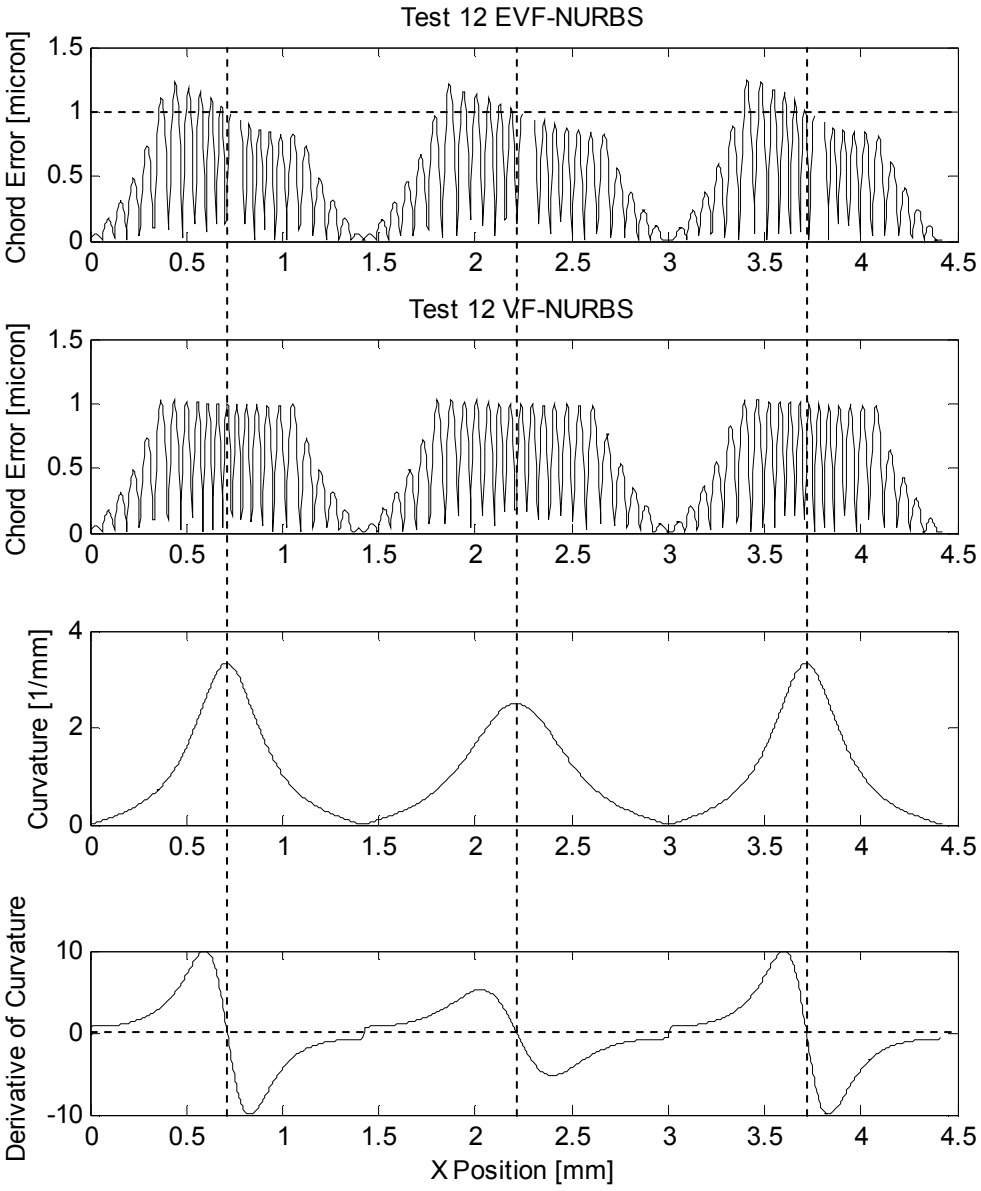

Figure 3.8: Results from Test 12, indicating that the magnitude of derivative of curvature is smaller in this test relative to Test 6, resulting in a smaller magnitude of deviation from maximum allowable error in the standard VF-NURBS case.

The two curves chosen for this test have different values for maximum rate of change of radius of curvature with arc length. The first curve has a high rate of change, and the second curve has a low rate of change. It has been hypothesized that the increase of $\partial\rho/\partial s$ will cause an increase in chord error for the standard VF-NURBS method. Figure 3.9 shows a comparison of the test results for the high $\partial\rho/\partial s$ case with the test results for

the low ∂ρ/∂s case. Points from the high ∂ρ/∂s curve are shown as dots and circles, while points from the low ∂ρ/∂s curve are shown as crosses.

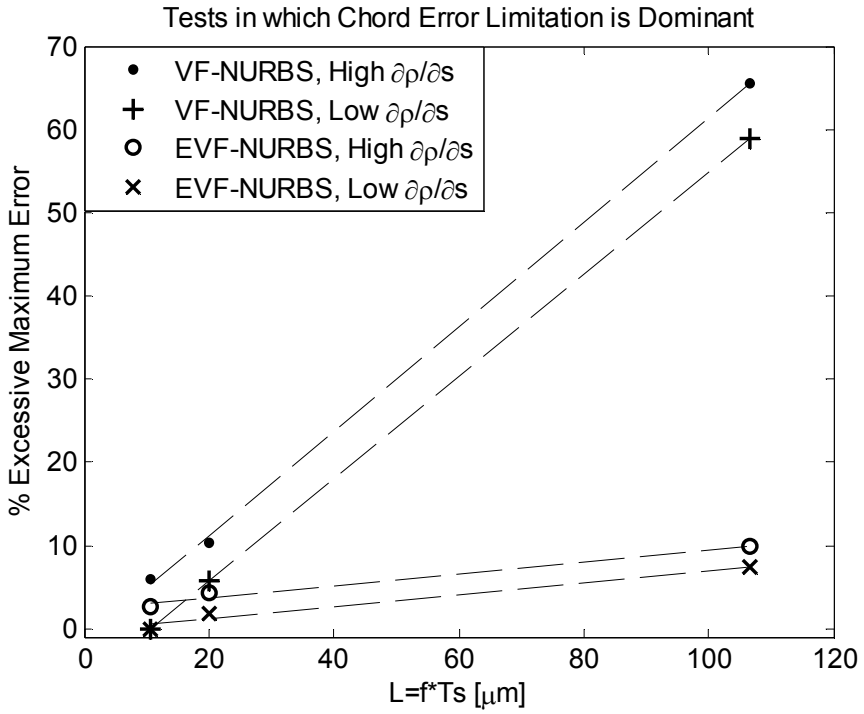

Figure 3.9: EVF-NURBS tests consistently show less error than the VF-NURBS tests. For both EVF-NURBS and VF-NURBS tests, there is a trend of increasing error with increasing sampling rate and with increasing ∂ρ/∂s.

Linear trends are displayed in Figure 11 for each set of data. The R^2 value for each trend is shown in Table 3.3.

Table 3.3: R^2 values for the linear trends seen in the tests in which the chord error feedrate limitation is dominant

Interpolation Method	∂ρ/∂s Value	R^2
VF-NURBS	High	0.9995
	Low	1.0000
EVF-NURBS	High	0.9873
	Low	0.9743

Summary

In this chapter, the impact of scale effects on the traditional method of VF-NURBS was examined. It was found that scale effects cause inaccuracy in the chord error estimation upon which feedrate optimization is based, resulting in excessive chord error when VF-NURBS is applied at the microscale. The new EVF-NURBS method was proposed to more accurately estimate chord error for feedrate optimization at the microscale. The EVF-NURBS method was numerically evaluated and found to provide as much as 56% error reduction relative to the standard VF-NURBS method when applied to the current PC-based control technology setup.

Chapter 4: Variable-Feedrate Intelligent Segmentation

In this chapter, the method of Variable-Feedrate Intelligent Segmentation (VFIS) is proposed to address the problems arising from the convergence of the maximum and minimum feedrate limits by taking advantage of trajectory generation time differences in interpolation methods. The VFIS method consists of two components: curvature-based segmentation and stability-based segmentation. Each component will be derived and numerically evaluated.

4.1 Overview of Intelligent Segmentation

Chord error and interpolation error are linked in interdependence through the trajectory generation rates achievable by different interpolation methods. Circular and NURBS interpolation methods both have advantages and disadvantages as applied to micromilling. Although use of circular interpolation allows a higher sampling rate due to the simplicity of trajectory computation, it also has two drawbacks that must be considered. First, use of circular interpolation is likely to result in more interpolation error than use of the NURBS method. Second, use of circular interpolation is likely to result in a larger number of segments and, hence, a longer CNC code. Thus, use of circular interpolation to decrease the magnitude of chord error at a given feedrate results in increased interpolation error. Decrease of chord error and decrease of interpolation error are mutually exclusive objectives. The goal of error reduction is to reduce total error, which is primarily the sum of chord error and interpolation error.

Because a reduction in chord error causes an increase in interpolation error and vice versa, maximum error reduction can not be achieved by pursuing minimum chord error or minimum interpolation error alone. Rather, minimum total error can be achieved by determining the optimal compromise between chord error reduction and interpolation error reduction.

The VFIS method is based on the proposition that the use of a combination of the NURBS and circular interpolation methods can be used to increase feedrate and improve stability without increase of total error. The NURBS method allows for low interpolation error, due to the ability of NURBS to interpolate a high-order or closed curve accurately. However, the computational complexity of the NURBS method requires a low sampling rate in order to complete trajectory calculations real-time, thus increasing chord error over the NURBS segment. Linear/circular interpolation, on the other hand, may induce large interpolation error in segments which do not resemble circles. The computational simplicity of this method, however, allows a high sampling rate, thus decreasing chord error in these segments. Since circular and NURBS interpolation both have some advantages and some disadvantages, it is proposed that reduced total error and increased feedrates can be achieved by segmenting to make use of the benefits of both methods by applying the appropriate method to each segment. Circular interpolation is used in areas of the curve where the large computational time of the NURBS method requires a large reduction in feedrate which causes instability in the cutting mechanics and chip formation, and in segments that are found to closely resemble circles. NURBS interpolation is used to minimize interpolation error in segments of low curvature that do not require low feedrate to satisfy chord error bounds.

Figure 4.1 is an illustration of the trade-off upon which the variable-feedrate intelligent segmentation algorithm is based. The figure shows the trend of decreasing interpolation error and increasing chord error with increasing trajectory generation time. These trends result in the existence of a minimum value for total error.

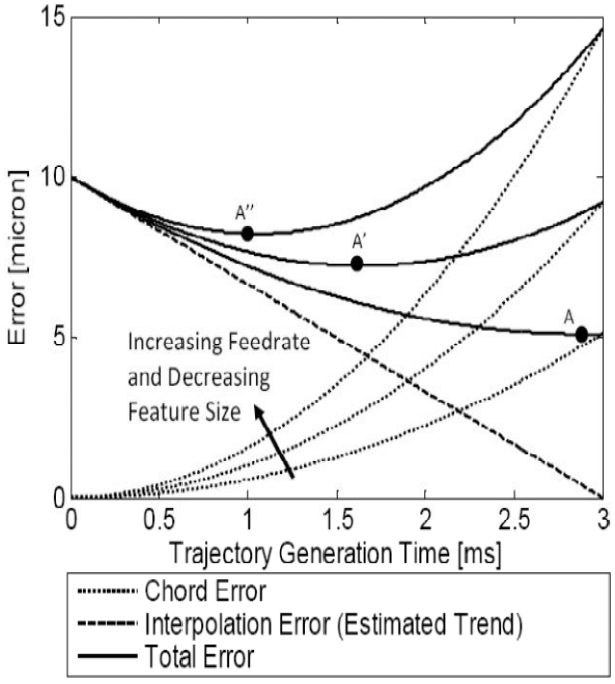

Figure 4.1: Interpolation error and chord error show opposite trends with trajectory generation time, resulting in a global minimum for total error

4.2 Variable-Feedrate Intelligent Segmentation Algorithms

The variable-feedrate intelligent segmentation method consists of combining interpolation methods in the segmentation process to take advantage of the unique benefits of each interpolation method. This study adopts the methodology of minimizing resultant error while maintaining stability, and does not pursue the global minimization of both chord error and interpolation error. Rather, the approach considers the preferred

operating balance of chord error and interpolation error that satisfies the combined error budget for the geometry, but also provides for increased chip formation stability. The VFIS method is composed of two techniques: 1) curvature-based (CB) segmentation and 2) stability-based (SB) segmentation.

4.2.1 Curvature-Based Intelligent Segmentation

The method of curvature-based segmentation is to identify segments along a tool-path which can be circular interpolated with low interpolation error. Circular interpolation can be applied with low interpolation error when the segment to which it is applied closely resembles a circle. Since circles are by definition a constant-curvature shape, approximately circular segments can be identified as segments with nearly-constant curvature, or near-zero slope of curvature. The CB segmentation method consists of identifying and circular-interpolating segments with nearly-constant curvature, while segments with widely varying curvature are NURBS-interpolated. Segment length is determined so that total error limit specifications are not violated.

The CB segmentation method proceeds as follows. First, curvature is calculated at each point along the known geometry. Because this step is done prior to interpolation, before a parametric description of the tool-path has been obtained, curvature k must be calculated numerically. This can be done by assuming a circular approximation for each three consecutive points along the tool-path, as in Eq. (1), where (x_i, y_i) represents geometry point i.

$$k(i) = \frac{2\left|\left(x_{(i-1)} - x_{(i)}\right)\left(y_{(i)} - y_{(i+1)}\right) - \left(y_{(i-1)} - y_{(i)}\right)\left(x_{(i)} - x_{(i+1)}\right)\right|}{\sqrt{\left(\left(x_{(i-1)} - x_{(i)}\right)^2 + \left(y_{(i-1)} - y_{(i)}\right)^2\right)\left(\left(x_{(i)} - x_{(i+1)}\right)^2 + \left(y_{(i)} - y_{(i+1)}\right)^2\right)\left(\left(x_{(i+1)} - x_{(i-1)}\right)^2 + \left(y_{(i+1)} - y_{(i-1)}\right)^2\right)}} \quad (1)$$

Curvature is calculated numerically and geometry points are known to limited accuracy. Thus, there may be noise in the curvature calculation. If the curvature profile is not smoothed, there may be inaccuracy in the later calculation of slope of curvature. To smooth the curvature calculations, the moving average of curvature is calculated and used in place of the curvature calculation, as in Eq. (2), where *w* is the window size for the moving average.

$$k_{avg}(i) = \frac{1}{w}\sum_{j=i-w/2}^{i+w/2} k(j) \quad (2)$$

Slope of curvature can then be calculated from the smoothed curvature calculations, as in Eq. (3), where *s(i)* is the Euclidean distance between points *i* and *i-1*.

$$b_k(i) = \frac{k_{avg}(i) - k_{avg}(i-1)}{s(i)} \quad (3)$$

Slope of curvature is also calculated numerically. Thus, there may be additional noise introduced in the calculation from Eq. (3). To remove this noise, result from Eq. (3) is smoothed by calculating the moving average as in Eq. (4).

$$b_{k_{avg}}(i) = \frac{1}{w}\sum_{j=i-w/2}^{i+w/2} b_k(j) \quad (4)$$

The smoothing component of the CB algorithm is only necessary if the data point precision is low, as might be the case if replicating an object with measurements obtained from a method of physical measurement or image processing. In the general case of geometry generation via CAD, this component can be bypassed.

The result from Eq. (4) is then examined to identify segments with a near-zero value. These are segments which closely approximate circles and lines and can be linear/circular-interpolated with low interpolation error.

Linear/circular interpolation is applied to these segments, then interpolation error for the segment is calculated according to Eq. (5), where ρ_{int} is the radius of curvature of the circular interpolation for the segment, (c_x, c_y) is the center of the interpolation circle, and *dimension(x)* is the number of cutter location points in the segment.

$$\varepsilon = \max\left(\left| \rho_{\text{int}}(i) - \sqrt{\left(x(i) - c_x\right)^2 + \left(y(i) - c_y\right)^2} \right|_{i=1..\text{dimension}(x)} \right) \tag{5}$$

If the error from Eq. (5) exceeds the set error tolerance limit, segment length must be decreased, and the segment re-interpolated. If error is acceptable, the segment information is output. After all linear/circular segments are identified and interpolated, the remaining segments are NURBS-interpolated. A detailed flow chart of the algorithm is given in Figure 4.2.

The CB segmentation algorithm requires specification of a slope of curvature tolerance below which a segment will be recognized as a circle by the CB-segmentation method. The optimal value for this variable is curve-dependent, and so the algorithm includes a subroutine to determine its value for the current curve by gradient descent.

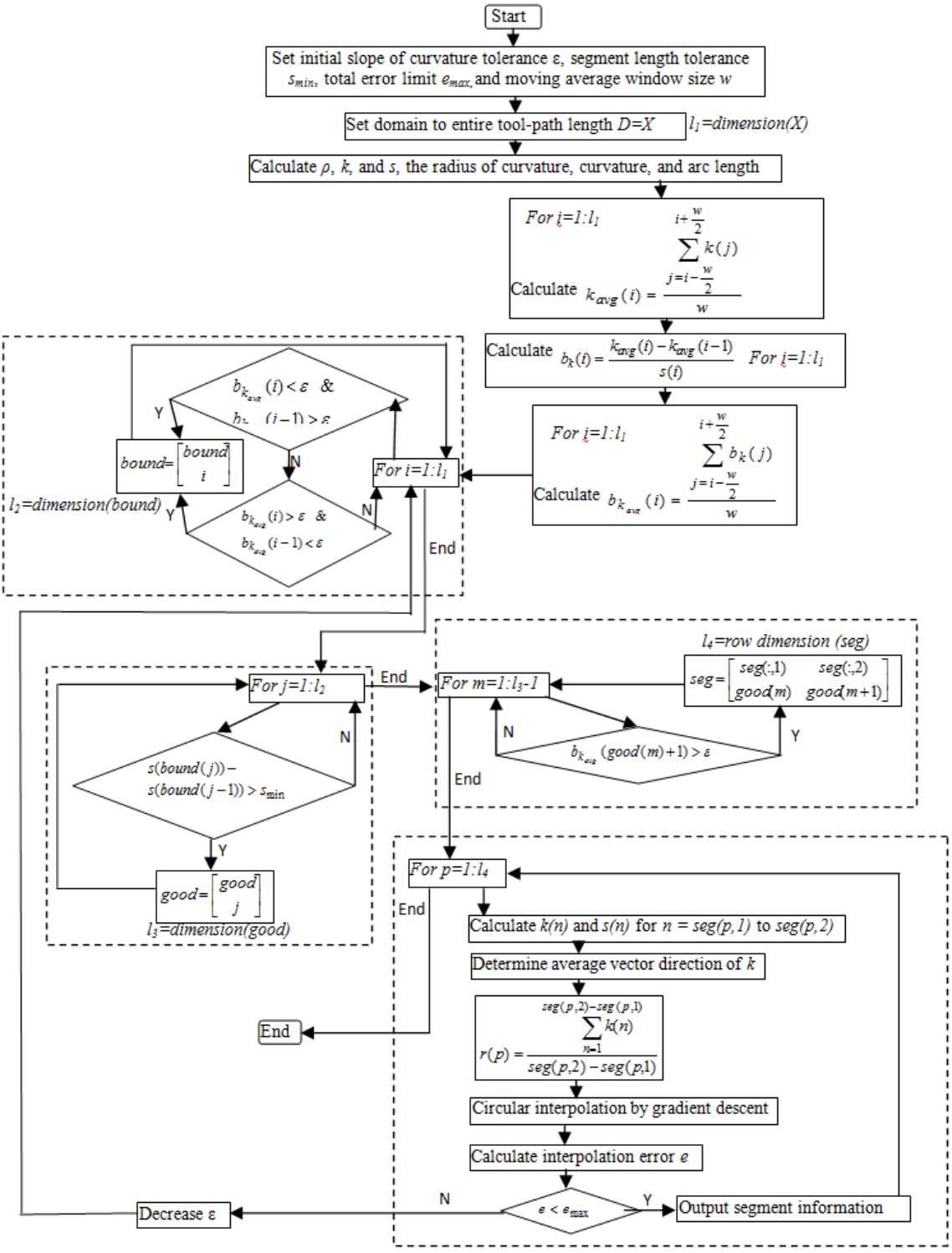

Figure 4.2: Flow chart for the curvature-based segmentation algorithm

The algorithm requires specification of a minimum segment length tolerance for circular segments. If the length of an identified segment falls below this tolerance, it will not be circular-interpolated. Optimal choice for this tolerance is curve-dependent, however, the inequality in Eq. (6) is provided as a guideline. If the maximum feedrate allowable by VF-NURBS according to the chord error limit is greater than the minimum feedrate according to minimum chip thickness, then the minimum segment length tolerance should be set to be greater than or equal to the VF-NURBS maximum feedrate times the fast sampling rate. This will prevent any cases of VFIS performing worse than VF-NURBS. If the maximum feedrate is less than the minimum, however, the minimum segment length should be set equal to the minimum feedrate times the fast sampling rate. This will prevent identification of segments that cannot be cut above the minimum chip thickness feedrate limit.

$$\begin{aligned} S_{min} &\geq \hat{f}_E FastTs \quad \text{if} \quad \hat{f}_E > f_{min} \\ S_{min} &= f_{min} FastTs \quad \text{otherwise} \end{aligned} \tag{6}$$

4.2.2 Stability-Based Intelligent Segmentation

The concept of the stability-based (SB) segmentation method is to identify and circular-interpolate segments in which the maximum feedrate limit falls below the minimum feedrate limit, creating either an unstable or high-error region. By circular interpolating these regions, the sampling rate is increased, thus raising the maximum feedrate limit above the minimum.

The SB segmentation algorithm begins by calculating the maximum and minimum feedrates for each cutter location point according to Eq. (7), which was derived in Chapter 2 and is recalled here.

$$0.3r_e nN < \hat{f}_E \le \frac{2}{T_s}\sqrt{(\rho - r)^2 - \left((\rho - r) - \delta_{\max}\right)^2} \tag{7}$$

Segments are then identified for which the maximum feedrate is lower than the minimum feedrate. Each of these segments is linear/circular interpolated, then the circular interpolation error is calculated. If the error exceeds the set error tolerance limit, point re-distribution is attempted: if there is an adjacent segment with acceptable error, the length of the adjacent segment is increased to shorten the segment with unacceptable error. If the points cannot be re-distributed, the segment with unacceptable error is divided into two segments, and interpolation is repeated. If the error is within the set tolerance limit, segment information is output and the remaining segments are NURBS-interpolated. A detailed flow chart for SB segmentation is shown in Figure 4.3.

The method of variable-feedrate intelligent segmentation consists of applying both CB segmentation and SB segmentation sequentially. The CB method is applied first, in order to ensure that all unstable regions are accounted for. After both methods have been applied, a check is made to determine if any segments have been circular-interpolated twice. If any segment has been circular-interpolated twice, one of the interpolations is eliminated. Finally, any segments not circular-interpolated are NURBS-interpolated.

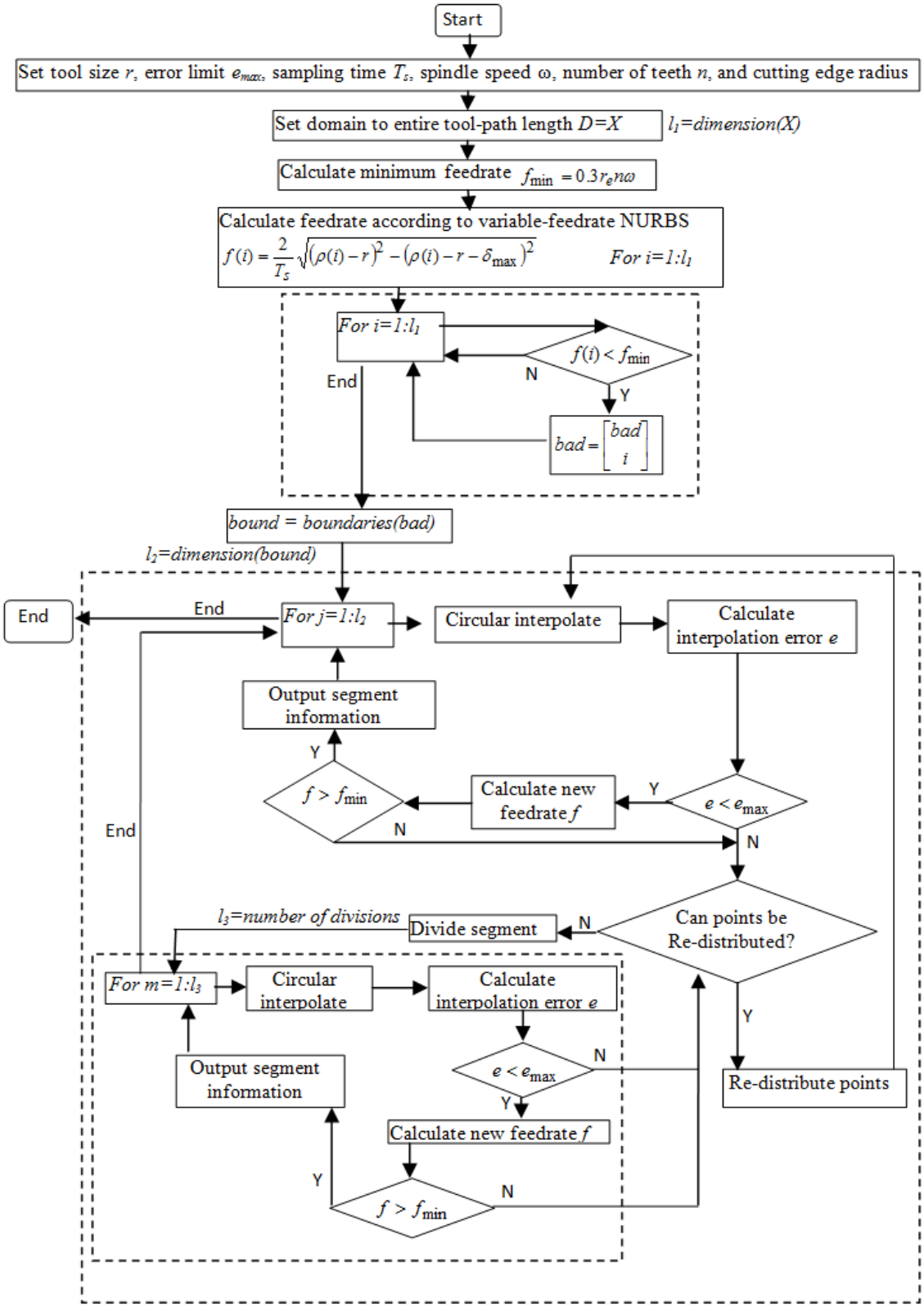

Figure 4.3: Flow chart for the stability-based segmentation algorithm

4.3 Variable-Feedrate Intelligent Segmentation Numerical Simulations

To evaluate the intelligent segmentation methods, two illustrative examples were chosen for simulation. A fan shape was chosen to demonstrate the methods on feature production, and an airfoil shape to demonstrate die production. The geometries for these two examples are shown in Figure 4.4, presented as the XY-plot of the data points extracted from the CAD description of the components. For both geometries, simulated machining performance will be numerically evaluated assuming a 2-flute endmill with a spindle speed of N = 500,000 *rpm* and cutting edge radius r_e = 3 *μm* for three tool sizes: 0.02 *mm*, 0.2 *mm*, and 1.0 *mm.* The data presented in the feedrate plots shown in this section are based on the 0.2 *mm* diameter tool. The sampling time for NURBS-interpolated segments is set at 2 *ms* while the sampling time for circular-interpolated segments is set at 0.1 *ms*, as calculated previously in Chapter 2 and the total error tolerance is set at 0.1 *μm*, characteristic for ultra high-precision micromachining processes.

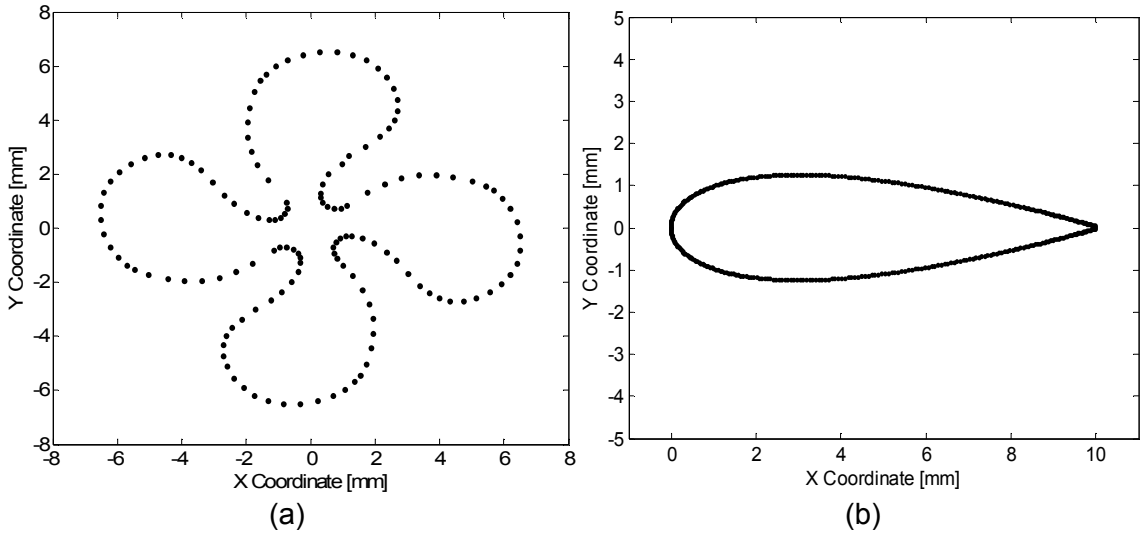

Figure 4.4: Numerical evaluations of the proposed intelligent segmentation approach were performed on two case studies, (a) an externally machined fan shape, and (b) an internally machined airfoil die cavity

First, consider the application of the segmentation methods to the fan shape. To apply CB segmentation to the fan, curvature and slope of curvature are calculated from the given fan geometry data points, and are plotted in Figure 4.5(a). Four circular segments are identified by considering portions of the curve that are of nearly uniform curvature, as illustrated by the shaded bands in Figure 4.5(a). These segments have curvature of approximately 0.5 mm^{-1}, which corresponds to a circular interpolation with radius of 2 *mm*.

The SB segmentation method was then applied to the fan shape. The VF NURBS maximum allowable feedrate for the fan shape was calculated using the microscale feedrate optimization equation shown in Eq. (6). The maximum feedrate periodically drops below the minimum feedrate, as illustrated in Figure 4.5(b). These regions, identified by the gray bands in Figure 4.5(b), are the segments identified by SB segmentation.

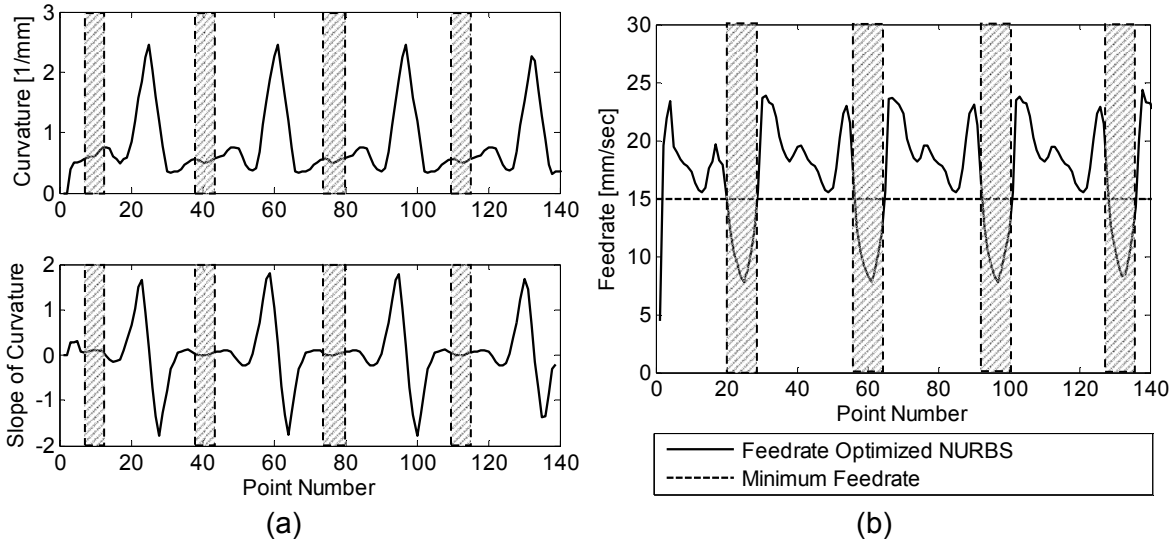

Figure 4.5: Segments identified by (a) curvature-based segmentation and (b) stability-based segmentation for the fan shape feature

Once segments have been identified, the maximum feedrate is recalculated with the faster sampling rate in the circular-interpolated segments. This faster sampling rate allows a much faster maximum feedrate in the segments where circular interpolation is applied, as shown in Figure 4.6(a) for the CB method and in Figure 4.6(b) for the SB method. Note that the high feedrate indicated in Figure 4.6 can be achieved because of the high spindle speed, which maintains a reasonable chipload, or feed per tooth, at the high feedrates. The chord error does not increase with the increased feedrate because the increased feedrate is accompanied by an increased sampling rate. This study assumes an effective thermal management of the cutting process and therefore does not consider thermal softening or weakening of the tool, or related additional error.

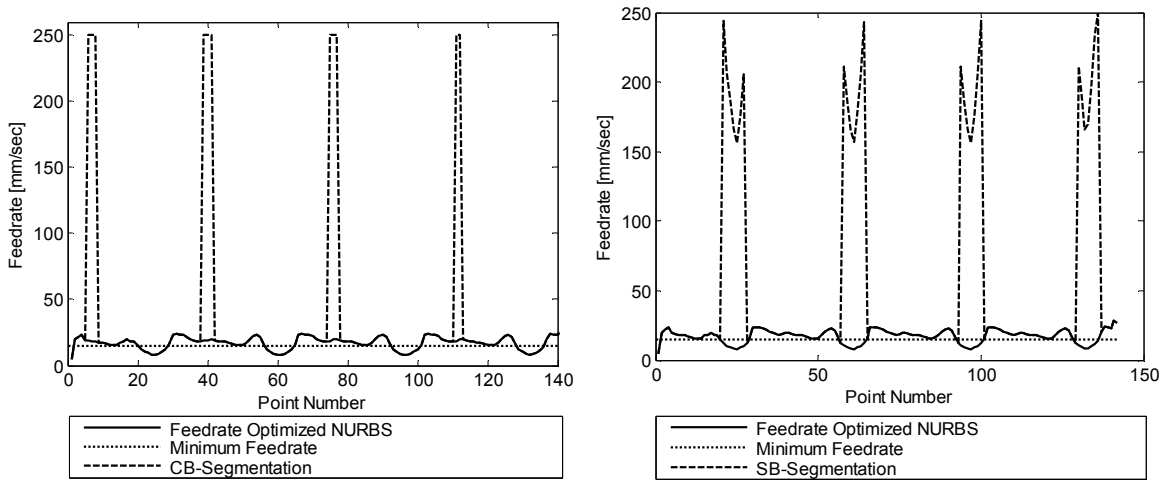

Figure 4.6: Maximum and minimum feedrate limits for the fan shape feature, after (a) curvature-based segmentation and (b) Stability-based segmentation

The machining time determined by each method: CB segmentation, SB segmentation, and the resultant VFIS, was calculated based on maximum feedrate along the path. The calculated machining times were benchmarked against the machining time required for the process implementing variable-feedrate NURBS and are presented in Table 4.1. The CB method was found to provide approximately 5% time benefit for each case, the SB method provided between 16 and 52% time benefit, and the VFIS method combined the time benefits, for 22-55% time benefit. Table 4.1 also indicates the number of segments, length of each segment, and chord and interpolation error for each segment found by each method. Note that in this case, interpolation error is identically zero in every case due to the low point density of the fan shape, which prevents more than three points from being circular interpolated to within error tolerances. As a result, each circular segment is limited to three points, which can be circular-interpolated with no interpolation error. This is not a generic result of the technique and will not exist in geometries with higher point densities, as will be seen in the case of the airfoil geometry.

Table 4.1: Results of Application of CB, SB, and VFIS Segment Methods Compared to VF NURBS for the fan feature shape

Tool Size [mm]	Interp. Method	Segment Length [mm]	Chord Error [µm]	Interp. Error [µm]	Max. Total Error [µm]	Sampling Time [ms]	Total Path Time [s]	% Time Benefit
0.02	CB	[0.9536 1.0609 1.0618 1.0591 58.7079]	0.1	0.0	0.1	[0.1 0.1 0.1 0.1 0.1 2.0]	2.8138	5.51%
	SB	[0.5002 0.4013 0.4376 0.3755 0.4180 0.4363 0.5090 0.4153 0.4310 0.3767 0.4176 58.1228]	0.1	0.0	0.1	[0.1 0.1 0.1 0.1 0.1 0.1 0.1 0.1 0.1 0.1 0.1 0.1 2.0]	2.4768	16.83%
	VFIS	[0.5002 0.4013 0.4376 0.3755 0.4180 0.4363 0.5090 0.4153 0.4310 0.3767 0.4176 0.9536 1.0609 1.0618 1.0591 53.9874]	0.1	0.0	0.1	[0.1 0.1 0.1 0.1 0.1 0.1 0.1 0.1 0.1 0.1 0.1 0.1 0.1 0.1 0.1 0.1 0.1 2.0]	2.3129	22.34%
	VF NURBS	[62.8433]	0.1	0.0	0.1	[2.0]	2.9782	
0.2	CB	[0.9536 1.0609 1.0618 1.0591 58.7079]	0.1	0.0	0.1	[0.1 0.1 0.1 0.1 2.0]	2.9059	5.46%
	SB	[0.5002 0.4013 0.4376 0.3755 0.4180 0.4363 0.5090 0.4153 0.4310 0.3767 0.4176 1.2446 56.8782]	0.1	0.0	0.1	[0.1 0.1 0.1 0.1 0.1 0.1 0.1 0.1 0.1 0.1 0.1 0.1 2.0]	2.4711	20.18%
	VFIS	[0.5002 0.4013 0.4376 0.3755 0.4180 0.4363 0.5090 0.4153 0.4310 0.3767 0.4176 1.2446 0.9536 1.0609 1.0618 1.0591 52.7428]	0.1	0.0	0.1	[0.1 0.1 0.1 0.1 0.1 0.1 0.1 0.1 0.1 0.1 0.1 0.1 0.1 0.1 0.1 0.1 0.1 2.0]	2.3020	25.64%
	VF NURBS	[62.8433]	0.1	0.0	0.1	[2.0]	3.0958	
1.0	CB	[0.9536 1.0609 1.0618 1.0591 58.7079]	0.1	0.0	0.1	[0.1 0.1 0.1 0.1 2.0]	5.0917	3.51%
	SB	[0.5002 0.4013 0.4376 0.3755 0.4180 0.4363 0.5090 0.4153 0.4310 0.3767 0.4176 1.2446 0.7116 0.7071 0.7104 0.7100 54.0391]	0.1	0.0	0.1	[0.1 0.1 0.1 0.1 0.1 0.1 0.1 0.1 0.1 0.1 0.1 0.1 0.1 0.1 0.1 0.1 0.1 2.0]	2.5276	52.10%
	VFIS	[0.5002 0.4013 0.4376 0.3755 0.4180 0.4363 0.5090 0.4153 0.4310 0.3767 0.4176 1.2446 0.7116 0.7071 0.7104 0.7100 54.0391]	0.1	0.0	0.1	[0.1 0.1 0.1 0.1 0.1 0.1 0.1 0.1 0.1 0.1 0.1 0.1 0.1 0.1 0.1 0.1 0.1 0.1 0.1 2.0]	2.3425	55.61%
	VF NURBS	[62.8433]	0.1	0.0	0.1	[0.2]	5.2771	

The interpolation methods were then applied to the airfoil die case. First, segments are identified for CB and SB segmentation methods. These segments are identified by the shaded bands in Figure 4.7(a) for CB segmentation, and in Figure 4.7(b) for SB segmentation.

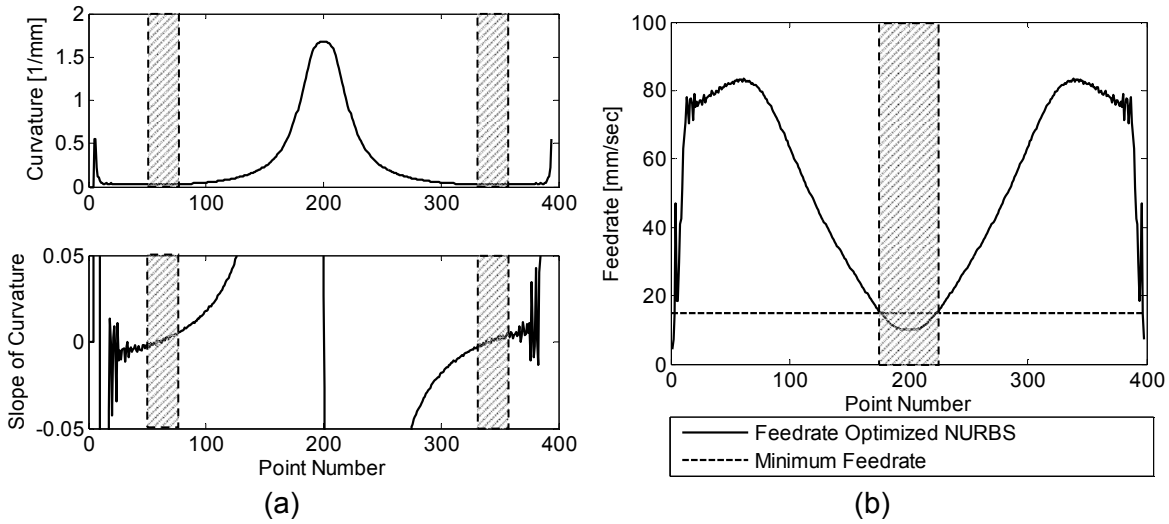

Figure 4.7: Segments identified by (a) curvature-based segmentation and (b) stability based segmentation for the airfoil die

These segments are circular-interpolated, and the modified maximum feedrate calculated, as shown in Figure 4.8(a) for the CB method and in Figure 4.8(b) for the SB method. The resulting maximum feedrate after application of SB-segmentation does not fall below the minimum feedrate, as shown in Figure 4.8(b).

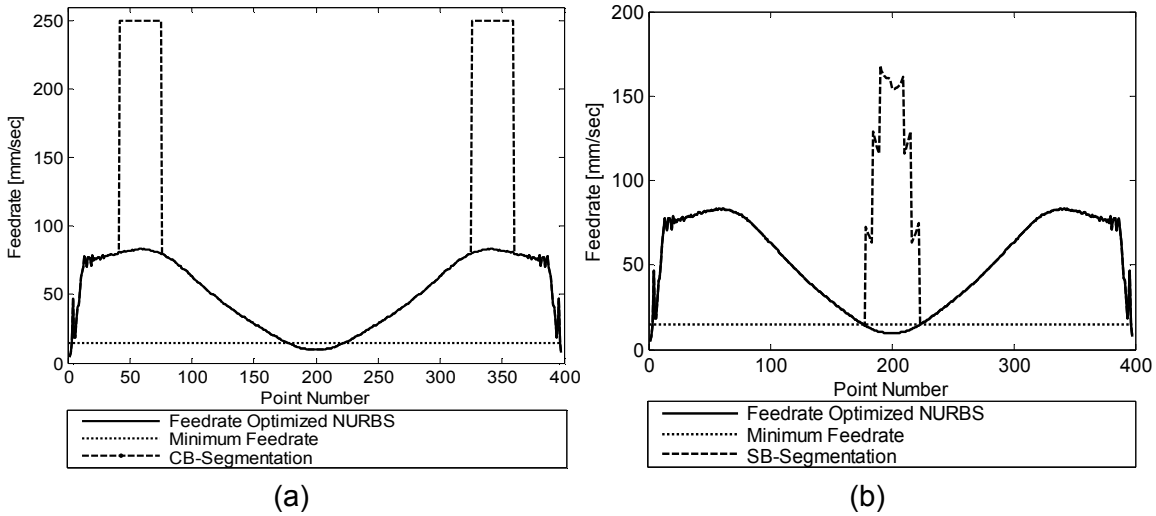

Figure 4.8: Maximum and minimum feedrate limits for the airfoil die shape, after (a) curvature-based segmentation and (b) Stability-based segmentation

The results from the machining time study for the airfoil die are presented in Table 4.2. For all three tool sizes, the machining time for the airfoil was reduced by approximately 6% by CB segmentation. The SB technique identified an additional 6-8 segments, depending on tool size, each approximately 0.15 *mm* long. As a result of the application of SB segmentation, the process was stabilized and the machining time decreased by an additional 15-31% for an overall time benefit for the VFIS method of 21-36%.

Table 4.2: Results of Application of CB, SB, and VFIS Segment Methods Compared to VF NURBS for the airfoil die shape

Tool Size [mm]	Interp. Method	Segment Length [mm]	Chord Error [µm]	Interp. Error [µm]	Max. Total Error [µm]	Sampling Time [ms]	Total Path Time [s]	% Time Benefit
0.02	CB	[2.0092 2.0334 17.2930]	[0.0664 0.0540 0.1]	[0.0336 0.0460 0.0]	0.1	[0.1 0.1 2.0]	0.4701	6.37%
	SB	[0.1451 0.1780 0.1608 0.1634 0.1504 0.1449 20.3930]	[0.0597 0.0098 0.0098 0.0092 0.0365 0.0932 0.100]	[0.0403 0.0902 0.0902 0.0902 0.0635 0.0068 0.0000]	0.1	[0.1 0.1 0.1 0.1 0.1 0.1 2.0]	0.4192	16.51%
	VFIS	[0.1451 0.1780 0.1608 0.1634 0.1504 0.1449 2.0092 2.0334 16.3504]	[0.0597 0.0098 0.0098 0.0092 0.0365 0.0932 0.0664 0.0540 0.100]	[0.0403 0.0902 0.0902 0.0902 0.0635 0.0068 0.0336 0.0460 0.0000]	0.1	[0.1 0.1 0.1 0.1 0.1 0.1 0.1 0.1 2.0]	0.3872	22.88%
	VF NURBS	[21.3356]	[0.1]	[0.0]	0.1	[2.0]	0.5021	
0.2	CB	[2.0092 2.0334 17.2930]	[0.0664 0.0540 0.1]	[0.0336 0.0460 0.0]	0.1	[0.1 0.1 2.0]	0.4804	6.25%
	SB	[0.2325 0.1521 0.1661 0.1690 0.1540 0.2037 16.2156]	[0.0600 0.0300 0.0068 0.0068 0.0300 0.0647 0.100]	[0.0400 0.0700 0.0932 0.0932 0.0700 0.0353 0.0000]	0.1	[0.1 0.1 0.1 0.1 0.1 0.1 2.0]	0.3942	23.07%
	VFIS	[0.2325 0.1521 0.1661 0.1690 0.1540 0.2037 2.0092 2.0334 16.2156]	[0.0600 0.0300 0.0068 0.0068 0.0300 0.0647 0.0664 0.0540 0.100]	[0.0400 0.0700 0.0932 0.0932 0.0700 0.0353 0.0336 0.0460 0.0000]	0.1	[0.1 0.1 0.1 0.1 0.1 0.1 0.1 0.1 2.0]	0.3622	29.32%
	VF NURBS	[21.3356]	[0.1]	[0.0]	0.1	[2.0]	0.5124	
1.0	CB	[2.0092 2.0334 17.2930]	[0.0664 0.0540 0.1]	[0.0336 0.0460 0.0]	0.1	[0.1 0.1 2.0]	0.5707	5.36%
	SB	[0.2325 0.1521 0.1318 0.1817 0.1851 0.1661 0.1224 0.2037 15.9176]	[0.0600 0.0300 0.0415 0.0078 0.0078 0.0095 0.0584 0.0651 0.100]	[0.0400 0.0700 0.0585 0.0922 0.0922 0.0905 0.0416 0.0349 0.0000]	0.1	[0.1 0.1 0.1 0.1 0.1 0.1 0.1 0.1 2.0]	0.4200	30.35%
	VFIS	[0.2325 0.1521 0.1318 0.1817 0.1851 0.1661 0.1224 0.2037 2.0092 2.0334 15.9176]	[0.0600 0.0300 0.0415 0.0078 0.0078 0.0095 0.0584 0.0651 0.0664 0.0540 0.100]	[0.0400 0.0700 0.0585 0.0922 0.0922 0.0905 0.0416 0.0349 0.0336 0.0460 0.0000]	0.1	[0.1 0.1 0.1 0.1 0.1 0.1 0.1 0.1 0.1 2.0]	0.3877	35.71%
	VF NURBS	[21.3356]	[0.1]	[0.0]	0.1	[2.0]	0.6030	

The VFIS method combines the two methods of CB and SB segmentation to compound the benefits, resulting in a maximum feedrate limit that is significantly faster than the

NURBS maximum feedrate at each circular segment, as shown in Figure 4.9(a) for the fan feature and in Figure 4.9(b) for the airfoil die.

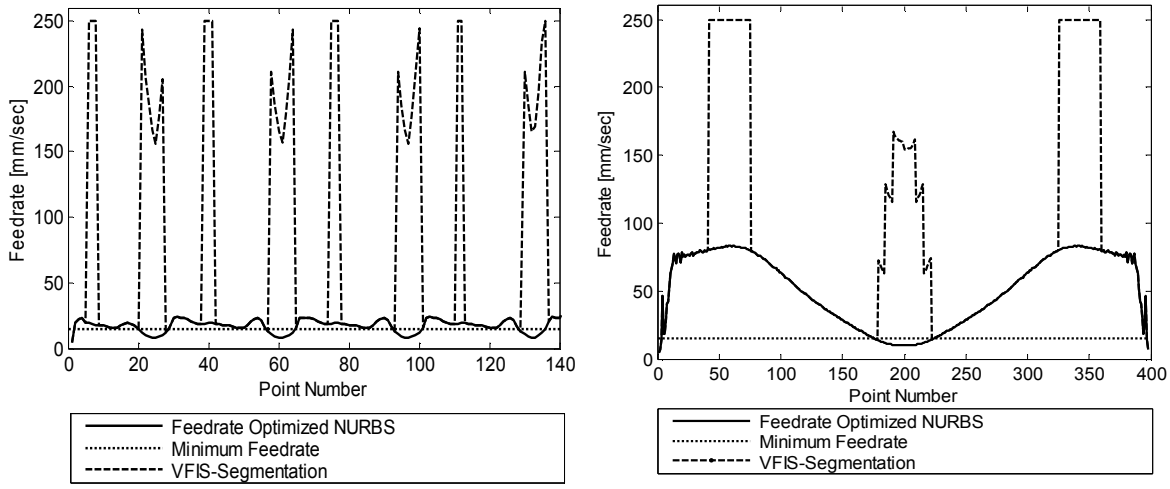

Figure 4.9: Final results of the intelligent segmentation feedrate optimization method on the (a) fan shape and the (b) airfoil die cavity.

The limit on maximum feedrate calculated in this study does not consider other factors that may further limit feedrate, such as limitations on motor speed and acceleration limitations from system inertia. A 250 *mm/s* limit on feedrate was imposed as an approximate maximum limit on velocity capabilities of a high-speed micro/meso-scale machining center. The number of segments identified and the length of the identified segments varied between the two geometries and the three tool sizes. Figure 4.10 presents the number of segments identified by the interpolation methods considered: circular interpolation, VFIS segmentation, SB segmentation, CB segmentation, and NURBS interpolation for both the fan and the airfoil. Figure 4.11 records the corresponding minimum segment length for each of the interpolation methods for both shapes.

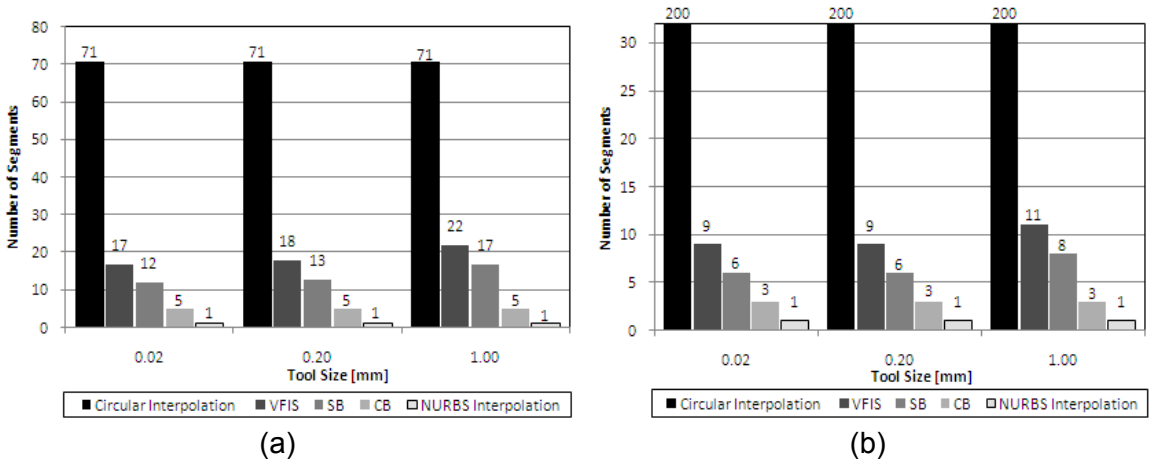

Figure 4.10: Number of segments identified by each interpolation approach for (a) the fan feature shape and (b) the airfoil die shape

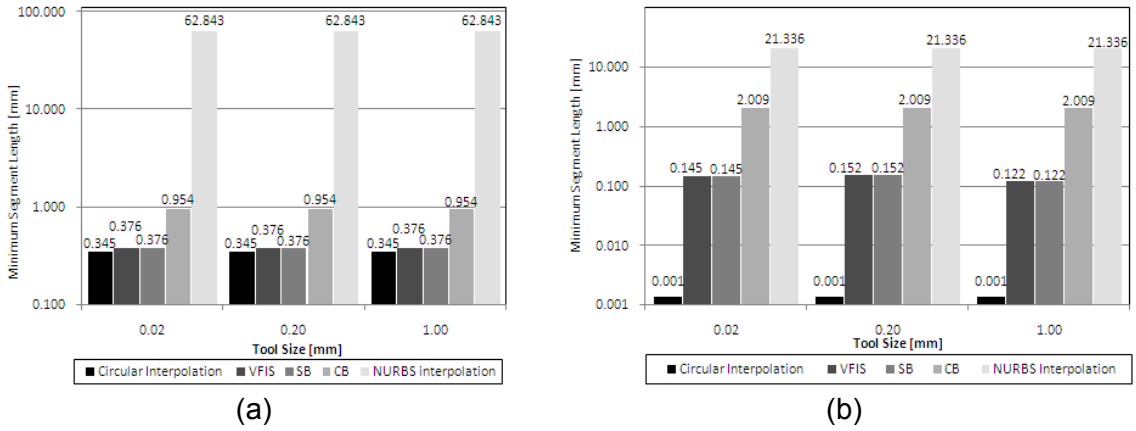

Figure 4.11: Minimum length of segments identified by each interpolation approach for (a) the fan feature shape and (b) the airfoil die shape

For both geometries, interpolation by NURBS results in a single segment the length of the entire tool-path while circular interpolation results in a large number of short segments. For example, in the airfoil case, the single NURBS segment is 21.336 *mm* long, while circular interpolation requires 200 segments as small as 1 *μm*. Neither of these solutions is optimal. The necessarily complex equation for NURBS and the large number of segments required for circular interpolation, results in longer computational times or increased code length, respectively, and the associated negative effects

discussed previously. The VFIS method achieves an optimal compromise between segment length and number of segments by applying circular interpolation in areas of the geometry that can benefit most from an increase in sampling frequency, and applying NURBS interpolation in areas of the geometry that can benefit most from a reduction in the number of segments. As a result, the VFIS method achieves a solution with a moderate number of segments (9-11 for the airfoil) with moderate minimum segment length (0.122-0.152 *mm* for the airfoil), and thus meets the objective of providing an enhanced parametric description of the tool-path.

Either CB or SB segmentation can be applied alone. However, the cutting process may become unstable if stability-based segmentation is not applied, and productivity benefits may be missed if curvature-based segmentation is not applied. To ensure stability and gain maximum productivity benefits, both components should be applied as part of a complete implementation of the VFIS method.

CB segmentation allows for a longer circular segment length within set error tolerances than is achievable with circular interpolation alone. The number of segments which can be identified by curvature-based segmentation and the resulting amount of benefit depends entirely on the curvature of the geometry and is independent of the size of the target geometry, size of the tool, and other process parameters. If the geometry has many sections that are nearly circular the benefit of this method is large. Conversely, if the geometry has few nearly circular segments, there is little benefit to be gained with this method. It may happen that a special case may exist in which the geometry will be shown to have no nearly-circular segments, and therefore result in no gain achieved by the CB technique.

In the SB technique, the identified segments may not have nearly zero slope of curvature (resembling circles). The segment length must be reduced in order to remain within set error tolerances, thus requiring a larger number of segments than with the CB segmentation, as indicated in Figure 4.10 and Figure 4.11. SB segmentation achieves significant improvement over variable-feedrate NURBS and over CB segmentation at the microscale by increasing feedrate in the slowest segments of the curve.

The benefits that can be achieved with the VFIS method increase as tool-size/feature-size ratio increases. Figure 4.12 presents the percent time benefit achieved for each simulation test case plotted against the mean tool-size to feature-size ratio along the path for the given tool size. As the mean ratio of tool-size to feature-size increases, the number and length of segments which can benefit from SB segmentation increase. This is due to the decrease of maximum feedrate as the difference between feature size and tool size decreases, without a corresponding decrease of minimum feedrate (ref. Eq. (5)).

The benefits of the CB segmentation method do not increase with tool-size to feature-size ratio, but decrease slightly. The lack of increase is due to the exclusive dependence of the CB segment identification on the curvature of the target geometry, which does not change with tool-size to feature-size ratio. The decrease in time benefit is the result of variation in the machining time required with the VF NURBS method. As tool-size to feature-size ratio increases, the VF NURBS method requires a longer time, while the actual time decrease afforded by the CB method remains constant. Thus, the percent time benefit of this method decreases slightly as tool-size to feature-size ratio increases.

The VFIS method is primarily beneficial at the microscale, where tool-size to feature-size ratio becomes large. However, the method is also useful at the macroscale in specialized cases of a large tool size, high curvature, high precision requirements, or a combination of the three. CB segmentation alone, however, is equally beneficial at both the microscale and macroscale, whenever there are segments of near-zero slope of curvature.

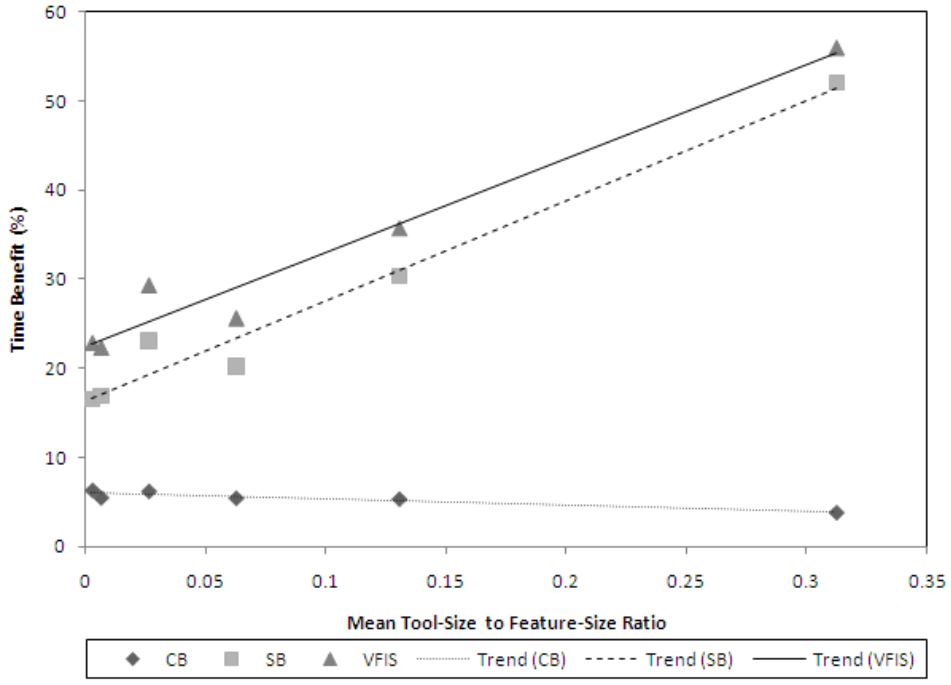

Figure 4.12: Percent time benefit over VF NURBS method achieved by each interpolation approach by mean tool-size to feature-size ratio

Summary

The Variable-Feedrate Intelligent Segmentation method was introduced as a means of compensating for the increased Λ ratio by selecting the interpolation method to be applied in different regions of a curve. Two components of this method, Curvature-Based Segmentation and Stability-Based Segmentation, were presented. The CB segmentation method consists of circular interpolating a curve in regions of constant

curvature, while the SB segmentation method consists of circular interpolating a curve in regions of high curvature. Both methods were shown to provide significant time savings over traditional VF-NURBS due to the increased sampling rates allowed by these methods.

Chapter 5: Experimental Evaluation of Trajectory Generation Methods

In this chapter, the methods of Enhanced Variable-Feedrate NURBS and Variable-Feedrate Intelligent Segmentation will be experimentally evaluated on a testbed machine. First, the apparatus for the tests will be identified. Then, the approach to the testing procedure is laid out, including the means of evaluation of the methods. A detailed explanation is then given for the choice of process parameters for the test in order to fairly evaluate the numerical simulations from previous chapters. This is followed by the introduction of the β parameter as a factor in VFIS implementation. Finally, results are presented from cutting tests. The first set of test results presented is from a complete set of evaluation tests performed on sine wave geometries. The second set is an evaluation of the fan and airfoil shapes simulated previously in Chapter 4.

5.1 Apparatus

The following is a list of the apparatus which was utilized in the experimental evaluation presented in this chapter.

1. The cutting tests presented here were performed on the low cost/precision ratio micro/meso-scale machining center described in the Appendix. The three key capabilities of this machine are summarized in Table 5.1.
2. Inspection of the parts and evaluation of error were performed on a Leica microscope model DMRM.

3. Further inspection of the cutting path was performed with a Zygo white light interferometer model New View 200 with quoted nanometer precision.

Table 5.1: Summary of Key features of the custom micromilling machine described in the appendix, which was used for evaluation of the proposed trajectory generation methods

Feature	Value
Positioning Precision [μm]	±1
Maximum Feedrate [mm/s]	100
Work Volume [mm]	228x127x159

5.2 Experimental Approach

In order to evaluate the trajectory generation methods, a set of test geometries was specified. Geometries with varying curvature were chosen for testing in order to maintain generality in the results. A test geometry was chosen in which the minimum radius of curvature can be easily set in order to evaluate the relationship between the Λ ratio and time benefit of VFIS. A sinusoidal geometry was chosen for the primary evaluation tests because this geometry has a continuously-varying and well-defined radius of curvature. An explanation of characteristics of sinusoidal geometries which fit the requirements was given in Chapter 3.

It is necessary to test a variety of Λ ratios in order to evaluate the trends of the benefits of VFIS as predicted from the numerical studies presented in Chapter 4. This has been accomplished by both varying the tool size and varying the geometry for several values of minimum ρ. Three different sine waves have been considered in order to vary the Λ ratio for each test. Sinusoidal geometries with minimum radii of curvature of 150 *μm*, 250 *μm*, and 350 *μm* have been chosen in order to represent typical sizes of microscale geometries. Three common microendmill tool sizes have been chosen in order to

provide a wide range of Λ values for the selected feature sizes. Tool diameters of 100 *μm*, 150 *μm*, and 200 *μm* were tested. For all tests, the workpiece material is Al 6061. Axial depth of cut is 10 *μm*, and radial depth of cut is equal to the tool diameter. The maximum feedrate that can be sustained by the tool before breakage must also be considered as a feedrate limit. Here, this limit is assumed to be equal to the feedrate which creates a chip thickness equal to 2% of the tool diameter. The precise appropriate value for this feedrate limit depends on many factors, including workpiece material, tool material, tool cutting edge radius, and cutting speed. However, the 2% manufacturer-recommended value has been applied here as an assumption. The result is the feedrate limit expressed in Eq. (1).

$$\hat{f_T} = (0.02)(2r)(N)(n) \tag{1}$$

The complete test parameter set is presented in Table 5.2, along with the resulting Λ ratios and maximum allowable feedrates for limited chipload.

Table 5.2: Sine test parameters for evaluation of the trajectory generation methods. All tests were performed in Al 6061 with an axial depth of cut of 10 *μm*, with three repetitions for each test point

Test #	Tool Size [μm]	Minimum Feature Size [μm]	Ratio	f_T [mm/s]	Radial Depth of Cut [μm]
1		150	0.333		
2	100	250	0.200	5.333	100
3		350	0.143		
4		150	0.500		
5	150	250	0.300	8.000	150
6		350	0.214		
7		150	0.667		
8	200	250	0.400	10.667	200
9		350	0.286		

An example sinusoidal geometry with minimum radius of curvature equal to 150 *μm* is shown in Figure 5.1.

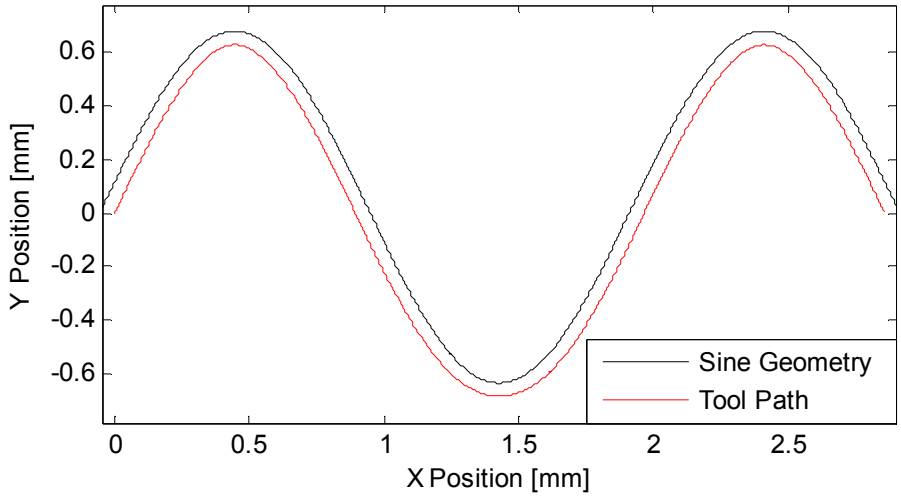

Figure 5.1: Example sine wave geometry with the generated tool path for a 100 *μm* tool

The sine wave was cut from the bottom, as shown by the example spindle path shown by the red curve in Figure 5.1 as a 50 *μm* perpendicular offset to the curve.

Each sine test specified in Table 5.2 was performed three times using the EVF-NURBS method from Chapter 3 and three times using the VFIS method from Chapter 4. For each trial, the command signal positions calculated by the algorithm was output and compared against the target toolpath. Algorithm error along the path was calculated as the perpendicular distance between target spindle points and the linear interpolation between algorithm points, as illustrated in Figure 5.2.

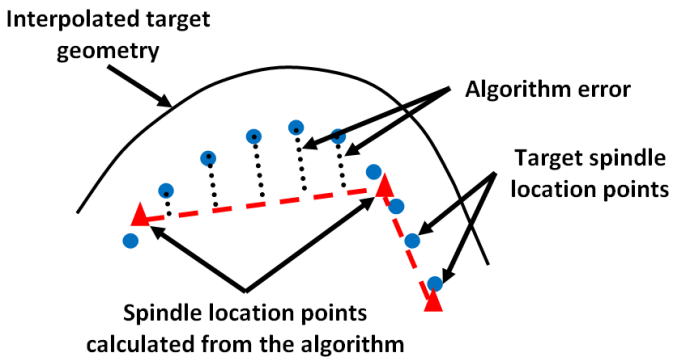

Figure 5.2: Algorithm error definition as applied to sine geometry cutting tests

After completion of all three trials for each test for both methods, the cut was imaged using the Leica microscope, with reported nanometer resolution. The image was then processed to extract the shape of the cutting edge. Although the sinusoidal geometries were chosen to fit within the Y-axis of the microscope, they do not fit within the X-axis of the field of view. Thus, a complete image was created by applying a stitching algorithm. A flow chart of the stitching algorithm applied is shown in Figure 5.3. After all pixel coordinates were output, the pixel coordinates were converted to X-Y coordinates using the microscope calibration. Error was then calculated by finding the distance between the curves at each point along the target geometry. This error is considered to be the total error, and includes both algorithm error and process errors such as tracking error, volumetric error, and tool deflection.

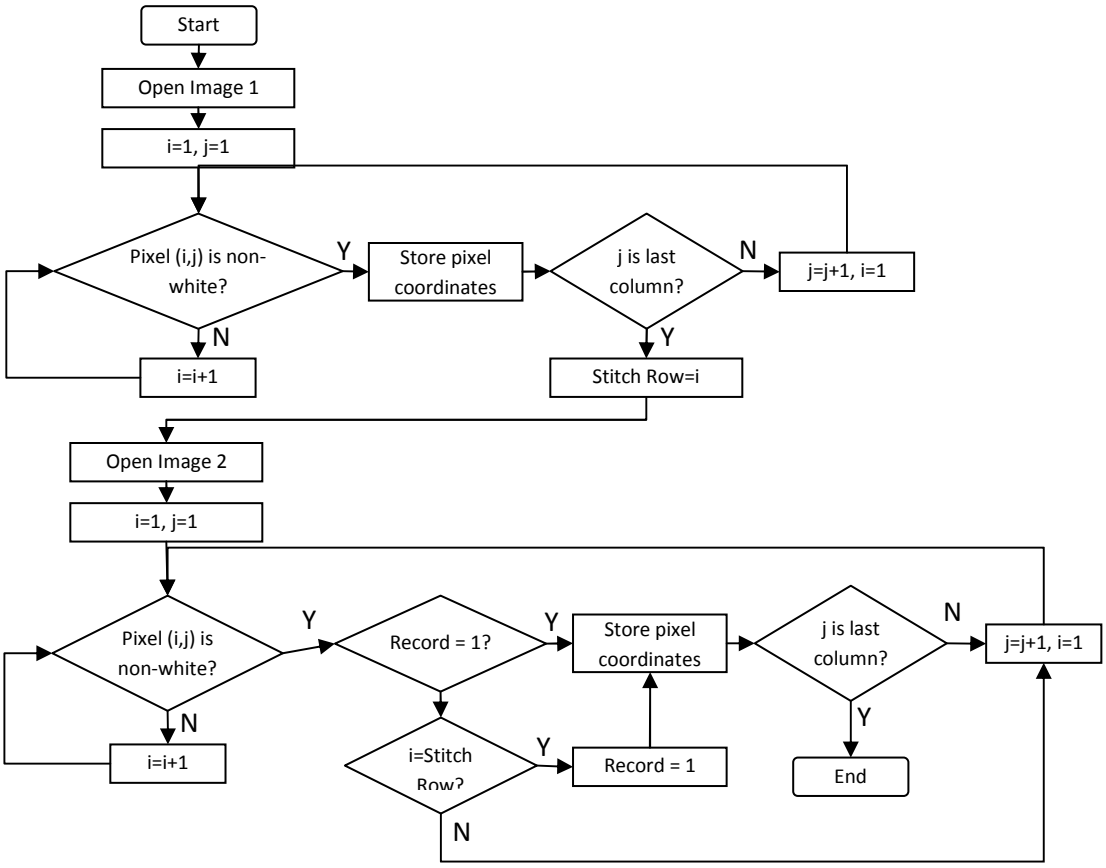

Figure 5.3: Flow chart of the metrology approach applied to the sinusoidal VFIS and modified VF-NURBS evaluation tests

The sinusoidal geometry tests were used for three purposes: a) to verify that the two algorithms are successfully able to constrain algorithm error to within the specified limit b) to determine the cutting time reduction benefits available with VFIS and c) to evaluate the amount of process error.

The fan and airfoil shapes presented in Chapter 4 were also cut. Because these shapes are too large to be imaged with the Leica microscope and too complex to be effectively reconstructed with the stitching algorithm, process error was not be able to be measured for these trials. Instead, these trials were evaluated in terms of cutting time and in terms of the error between the target toolpath and the encoder feedback. For these trials, a 200 *μm* stub-length tool was chosen, in order to limit errors due to tool deflection while still allowing for a tool which will fit in all features. A 30 *μm* axial depth of cut was chosen as 10% of the total flute length. As in the sine tests, the radial depth of cut is equal to the tool diameter, and the material is Al 6061.

5.3 Determination of Equivalent Test Parameters

The VFIS algorithm has been developed in mind of hardware capabilities considered cutting-edge or currently in development. The process parameters will be chosen so as to be able to experimentally evaluate the numerical simulations presented in Chapter 4 in light of the cutting-edge hardware assumption. A summary of the parameters which are representative of this cutting-edge technology are presented in Table 5.3.

Table 5.3: Parameter values for the numerical evaluation of VFIS

Parameter	Unit	Value	Description
ρ	mm	<1	Feature size
r	μm	10-1000	Tool size
Fast Ts	ms	0.01-0.1	Sampling rate for circular and linear segments
Slow Ts	ms	1.0	Sampling rate for NURBS segments
n	flutes	2	Number of flutes
N	krpm	500-1,000	Spindle speed
e	μm	0.1	Allowable algorithm error

The sampling rates and spindle speed from the numerical evaluation parameter set are not practically achievable on existing hardware. Instead, a simulation of these conditions is derived which faithfully represents the VFIS benefits available under the target conditions, yet is implementable within the capabilities of the available hardware. All of the parameters chosen for the experimental evaluation are summarized in Table 5.4.

Table 5.4: Parameter values for the experimental evaluation of VFIS

Parameter	Unit	Value(s)	Description
ρ	mm	<1	Feature size
r	μm	100, 150, 200	Tool size
Fast Ts	ms	10	Sampling rate for circular and linear segments
Slow Ts	ms	100	Sampling rate for NURBS segments
n	flutes	2	Number of flutes
N	krpm	80	Spindle speed
e	μm	10	Allowable algorithm error

A derivation of the choice of test parameters in Table 5.4 will now be presented.

Hardware limitations apply to the choice of a value for sampling rate *Fast Ts* and spindle speed *N*. The spindle speed value used in the numerical evaluation cannot be implemented because these ultra high-speed spindles are commercially available and are actively researched. The value for *Fast Ts* is limited by numerical computation, timer resolution, and communication latency limitations of the PC-based control hardware. PC-based control hardware was utilized in order to avoid the high costs associated with

dedicated hardware. The low-cost objective for this machine is further described in the Appendix.

The efficacy of the curvature-based portion of the VFIS algorithm depends solely upon the curvature characteristics of the target geometry, and not upon the process parameters chosen. However, the benefit available from the stability-based portion is highly dependent upon the portion of the feedrate profile $\hat{f}_E$ which falls below f_{min}. The benefit also depends upon the relative amount of feedrate increase which is possible between $\hat{f}_E$, which increases with T_s, and $\hat{f}_T$, which does not increase with T_s. Therefore, in order to fairly evaluate the benefits possible with VFIS as determined in the numerical evaluations, it is necessary to choose experimental evaluation parameters which preserve these feedrate relationships between the experimental and numerical cases.

Expressions for maximum allowable feedrate from a chord error limit were previously derived as in Eq. (2) for included features, and as in Eq. (3) for excluded features.

$$\hat{f}_E = \frac{2}{T_s}\sqrt{(\rho - r)^2 - (\rho - r - \delta)^2} \tag{2}$$

$$\hat{f}_E = \frac{2}{T_s}\sqrt{(\rho + r)^2 - (\rho + r - \delta)^2} \tag{3}$$

For all features, the minimum feedrate according to the minimum chip thickness is as in Eq. (4).

$$f_{min} = t_{c_{min}} nN \tag{4}$$

In the following mathematical representations, the subscript ‘1’ will refer to the numerical evaluation, while the subscript ‘2’ will refer to the experimental evaluation to be performed on existing hardware. It is necessary for the testing parameters to be chosen

so as to maintain the three ratios in Eqs. (5), (6), and (7), in order to simulate the conditions represented in the numerical evaluation.

$$\frac{\hat{f}_{T_1}}{f_{min_1}} = \frac{\hat{f}_{T_2}}{f_{min_2}} \tag{5}$$

$$\frac{\hat{f}_{E_1}}{f_{min_1}} = \frac{\hat{f}_{E_2}}{f_{min_2}} \tag{6}$$

$$\frac{\hat{f}_{T_1}}{\hat{f}_{E_1}} = \frac{\hat{f}_{T_2}}{\hat{f}_{E_2}} \tag{7}$$

Hardware limitations apply to the choice of *Fast Ts* and spindle speed *N*. Geometry radius of curvature and tool size are not restricted by hardware, and are unchanged. Remaining parameters are then chosen appropriately in order to maintain the key ratios in Eqs. (5-7).

The ratios are evaluated, starting with Eq. (5) evaluated in Eq. (8).

$$\frac{\hat{f}_T}{f_{min}} = \frac{(0.02)(2r)(N)(n)}{t_{c_{min}} nN} = \frac{0.04r}{t_{c_{min}}} \tag{8}$$

It is assumed that all tools to be used in this study have the same cutting edge radius, equal to 3 *μm*. The minimum chip thickness is also taken to be constant as 0.3 times the cutting edge radius. Then, the ratio in Eq. (8) is independent of all varying parameters.

Next, consider the ratios in Eqs. (6) and (7), evaluated in Eqs. (9) and (10), respectively.

$$\frac{\hat{f}_E}{f_{min}} = \frac{\frac{2}{T_s}\sqrt{(\rho - r)^2 - (\rho - r - \delta)^2}}{t_{c_{min}} nN} \tag{9}$$

$$\frac{\hat{f}_T}{\hat{f}_E} = \frac{0.04rNn}{\frac{2}{T_s}\sqrt{(\rho - r)^2 - (\rho - r - \delta)^2}} \tag{10}$$

In Eqs. (9) and (10), included features are assumed in order to account for worst-case scenario possibilities. In both of these ratios, spindle speed *N* and sampling rate *Fast Ts* have been restricted by hardware limitations. The only variable remaining to be determined is the maximum allowable chord error *δ*. Since Eqs. (6) and (7) must hold true for both *slow Ts* and *fast Ts*, in order for a solution for *δ* to exist for both values of *Ts*, it is now necessary to impose in addition that the ratio of *slow Ts* to *fast Ts* must remain constant between the target case and the test case, as shown in Eq. (11).

$$\frac{Slow\ Ts_1}{Fast\ Ts_1} = \frac{Slow\ Ts_2}{Fast\ Ts_2} \tag{11}$$

Thus, the value for *slow Ts* is determined. A value for *δ* will now be determined. This is done by considering both the target case and the test case. Eqs. (12) and (13) describe the relationships which are imposed by the low-cost hardware used in this implementation, whose development is described in the Appendix.

$$N_1 = 10N_2 \tag{12}$$

$$T_{s_1} = 0.01T_{s_2} \tag{13}$$

Eqs. (12) and (13) are substituted into Eqs. (3) and (4) to arrive at the relationships in Eqs. (14) and (15).

$$\hat{f}_{T_1} = 10\hat{f}_{T_2} \tag{14}$$

$$f_{min_1} = 10f_{min_2} \tag{15}$$

Thus, in order for the ratios in Eqs. (9) and (10) to hold true, Eq. (16) must also hold true.

$$\hat{f}_{E_1} = 10\hat{f}_{E_2} \tag{16}$$

The relationships in Eqs. (17) and (18) are derived from Eq. (1) in order to determine the value of *δ* so that Eq. (16) holds true.

$$\frac{T_{s_1}^2\hat{f}_{E_1}^2 + 4\delta_1^2}{8\delta_1} = \rho - r \tag{17}$$

$$\frac{T_{s_2}^2 \hat{f}_{E_2}^2 + 4\delta_2^2}{8\delta_2} = \rho - r \tag{18}$$

Eqs. (18), (16), and (13) are substituted into Eq. (17) to obtain a quadratic equation in δ_2 in terms of the known values for the target case. This is shown in Eq. (19).

$$-32\delta_1{\delta_2}^2 + \left(8{T_{s_1}}^2{\hat{f}_{E_1}}^2 + 32{\delta_1}^2\right)\delta_2 - 800{T_{s_1}}^2{\hat{f}_{E_1}}^2\delta_1 = 0 \tag{19}$$

Eq. (19) is then solved for δ_2. Because the value of ${\hat{f}_{E_1}}^2$ is not constant, a single value solution for δ_2 cannot be found. Instead, a value for δ_2 is chosen by applying a method of gradient descent to minimize the peak difference in the three key ratios in Eqs. (5-7) over the target curve. For the test curve and the chosen parameters, the ratio differences are minimized for a δ_2 value of 10 *μm*.

Given the numerical evaluation parameters in Table 5.3 and choosing for example a 100 *μm* diameter tool cutting below the sine wave, the three key feedrate profiles for the numerical evaluation parameter set are shown in Figure 5.4(a). The key feedrate ratios for the numerical evaluation parameter set are shown in Figure 5.4(b).

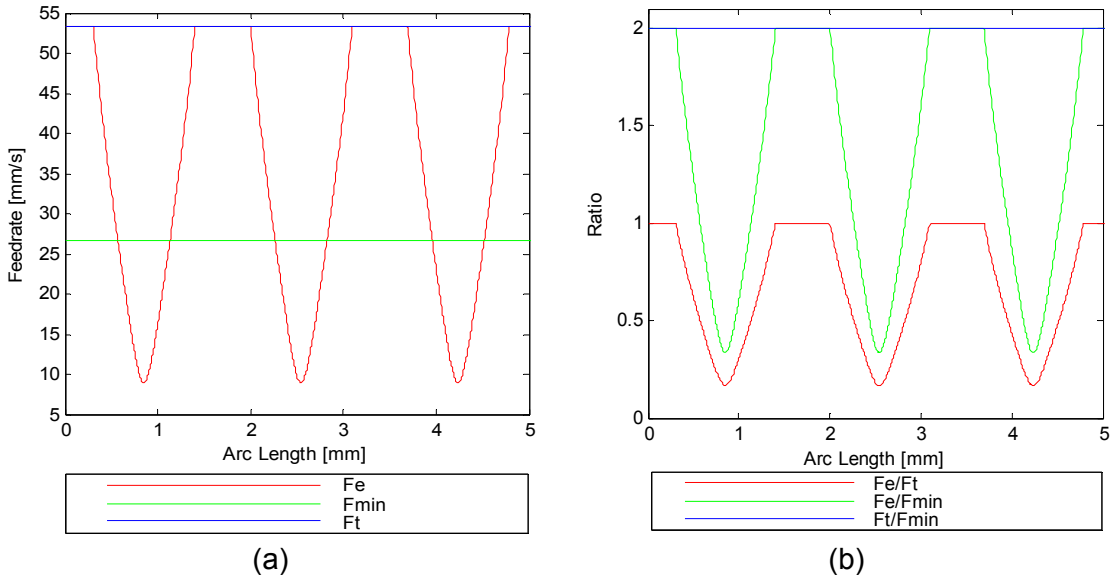

Figure 5.4: (a) Feedrate profiles and (b) feedrate limit ratios for the numerical evaluation parameters applied to the example sine wave

The three feedrate profiles for the experimental evaluation parameter set adapted for available hardware are shown in Figure 5.5(a), and the resulting ratios are shown in Figure 5.5(b).

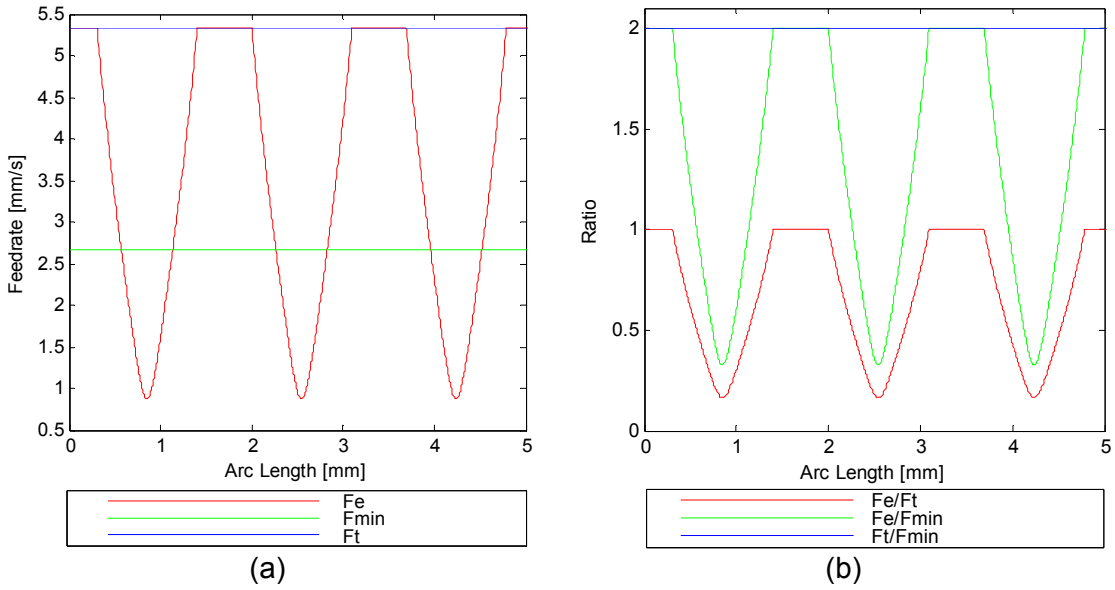

Figure 5.5: (a) feedrate profiles and (b) feedrate limit ratios for the experimental evaluation parameters applied to the example sine wave

The difference in the feedrate ratios for the numerical and experimental cases in Figure 5.4(b) and Figure 5.5(b) is calculated and plotted in Figure 5.6.

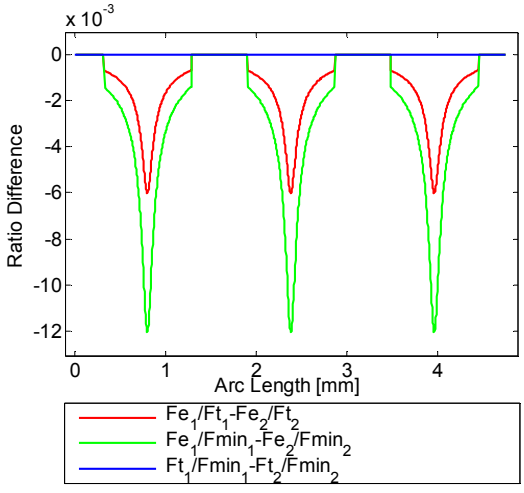

Figure 5.6: Difference in feedrate limit ratios between the numerical and experimental cases

The ratio difference is negligible, thus the experimental parameters can be considered a good simulation of parameters used in the numerical evaluation.

5.4 The β Parameter

An additional parameter must be chosen for the implementation of VFIS, which will be referred to here as the β parameter. This parameter specifies the portion of total error which can be allotted to interpolation error during the segmentation and interpolation stage. The remaining portion can then be allotted to chord error during the execution stage. This definition of the β parameter is expressed in Eqs. (20) and (21).

$$e = \delta + \varepsilon \tag{20}$$

$$\varepsilon \leq \frac{e}{\beta} \tag{21}$$

In the limit as ε becomes maximized, the relationship in Eq. (22) exists for δ.

$$\delta = e\left(1 - \frac{1}{\beta}\right) \tag{22}$$

The β parameter has the effect of trading off VFIS segment length with number of segments and determining feedrate limits for circular segments. A higher value of β will cause more, shorter segments with higher feedrates, while a lower value of β will result in fewer, longer segments with lower feedrates. The value of β is allowed to be any positive value greater than or equal to one. A β value that is too small may result in regions of the curve in which the maximum feedrate remains below the minimum feedrate even after the application of stability-based segmentation, leading to increased likelihood of large dynamic errors due to unstable chip-formation mechanics that will excite dynamic responses of the tool. A β value that is too high will result in fewer or no segments found by VFIS, decreasing or eliminating the time benefits of the VFIS

method. The specific β trade-off is curve-dependent, but a minimum value for β can be calculated analytically.

For the minimum β case, the value for allowable chord error must be large enough so that the maximum feedrate exceeds the minimum in the regions of highest curvature. Eq. (17) is solved for δ. Then, the limit of allowable feedrates for $\hat{f}_E$ is found by setting it equal to the minimum feedrate. Sampling rate is set to the fast sampling rate and the radius of curvature is set equal to the minimum radius of curvature along the curve. The result is shown in Eq. (23).

$$\frac{T_s^2 f_{min}^2 + 4\delta^2}{8\delta} = \rho_{min} - r \tag{23}$$

Eq. (22) is then substituted into Eq. (23) and solved for β. The results are shown in Eq. (24).

$$\beta \geq \frac{-e}{(\rho_{min} - r) \pm 0.5\sqrt{4(\rho_{min} - r)^2 - Fast{T_s}^2 {f_{min}}^2} - e} \tag{24}$$

Eq. (24) defines the smallest value allowable for β in order to maintain chip formation stability over the entire curve after the VFIS method is applied. For all sine tests performed, the β parameter is set to the minimum allowable value according to Eq. (24). The values are reported in Table 5.5.

Table 5.5: β parameter values applied for the sine wave experimental evaluation of VFIS

Test #	Tool Size [µm]	Minimum Feature Size [µm]	Ratio	β_{min}
1		150	0.333	1.0980
2	100	250	0.200	1.0466
3		350	0.143	1.0306
4		150	0.500	1.1357
5	150	250	0.300	1.0536
6		350	0.214	1.0334
7		150	0.667	1.2211
8	200	250	0.400	1.0631
9		350	0.286	1.0369

5.5 Sine Wave Cutting Test Results

After the cutting tests have been performed, the sine waves are imaged with the Leica microscope and the individual image components are stitched to create a complete image. Figure 5.7 shows a characteristic result from the EVF-NURBS method, and Figure 5.8 shows a characteristic result from the VFIS method.

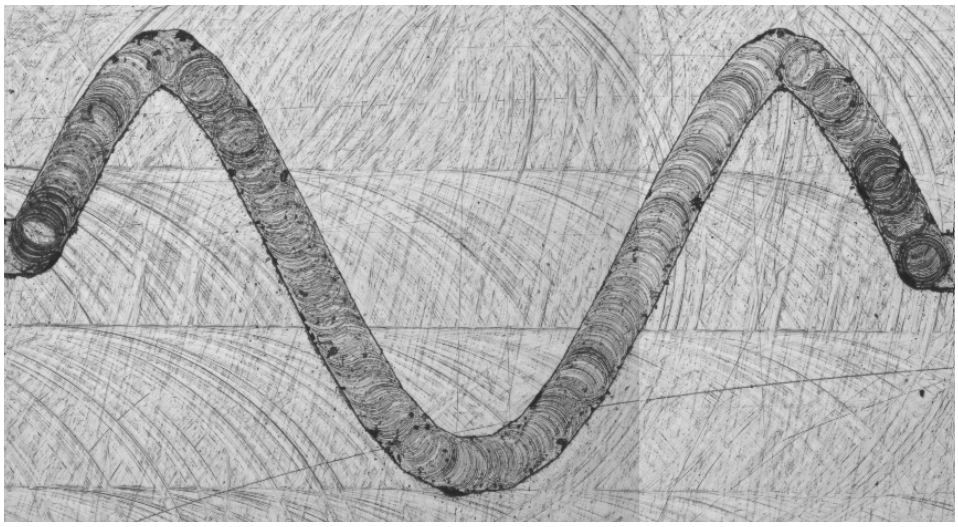

Figure 5.7: Stitched image of a sinusoidal geometry cut using the EVF-NURBS method

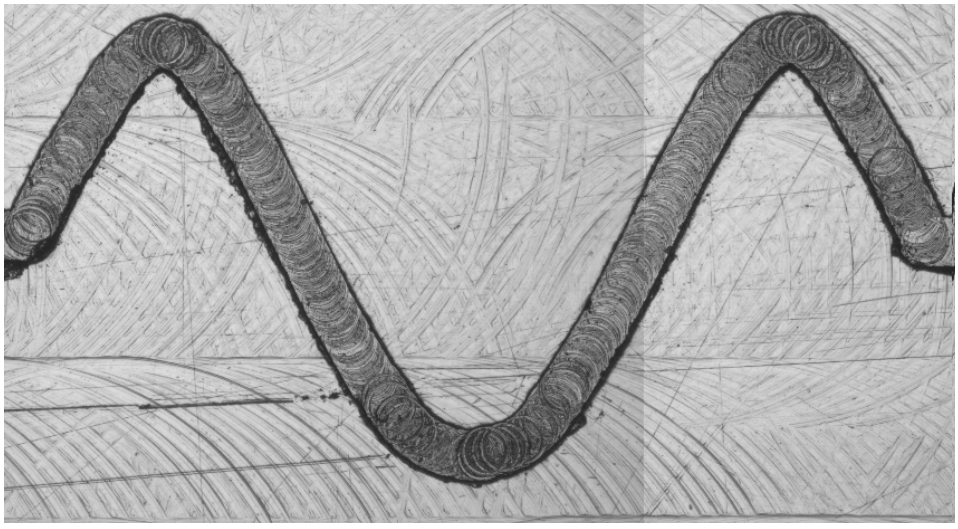

Figure 5.8: Stitched image of a sinusoidal geometry cut using the VFIS method

Data collected during all tests are then examined to quantify the performance of the algorithms. Error in the sinusoidal results is evaluated, then the cutting times are compared. Total error in the final part can be attributed to two sources: (1) algorithm error and (2) process error. The algorithm error is examined first, then total error is calculated. The difference in the errors is attributed to process error.

To evaluate algorithm error, the algorithm output is compared against the target toolpath. The algorithm output for a characteristic sinusoidal trial is compared with the target toolpath in Figure 5.9(a) for the EVF-NURBS method, and in Figure 5.9(b) for the VFIS method.

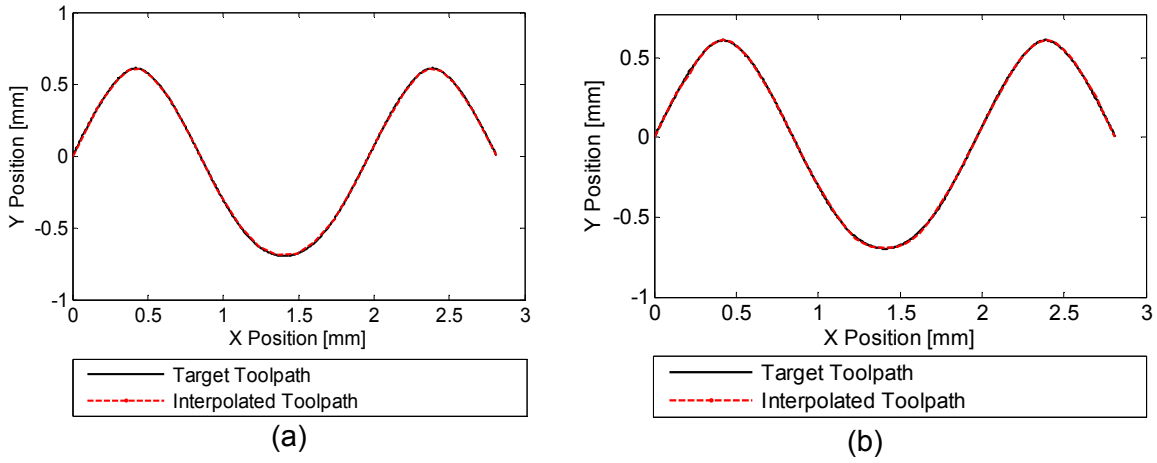

Figure 5.9: Comparison of algorithm-generated toolpath and target toolpath for a characteristic trial using (a) the EVF-NURBS method and (b) the VFIS method

A magnified view of a portion of the toolpath is shown in Figure 5.10.

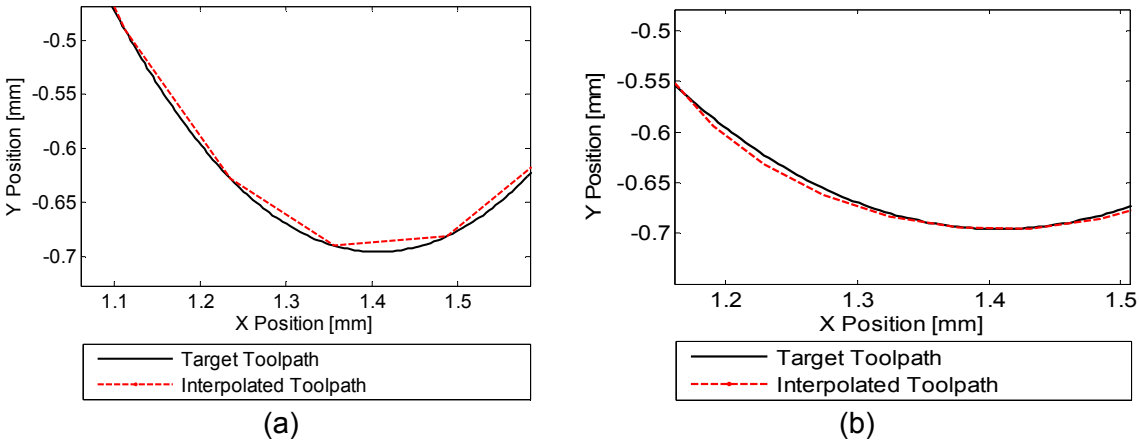

Figure 5.10: Magnified view of a portion of the sinusoidal toolpath trajectories as generated by (a) EVF-NURBS and (b) VFIS segmentation method

Algorithm error is equal to the sum of chord error and interpolation error. Figure 5.10 reveals the trade-off between chord and interpolation error achieved by the VFIS method. The EVF-NURBS method in Figure 5.10(a) generates a toolpath with zero interpolation error and significant chord error. The VFIS result in Figure 5.10(b) shows greater interpolation error, but little chord error. The total algorithm error is calculated for all trials for both methods. The results for the characteristic trial are shown in Figure 5.11.

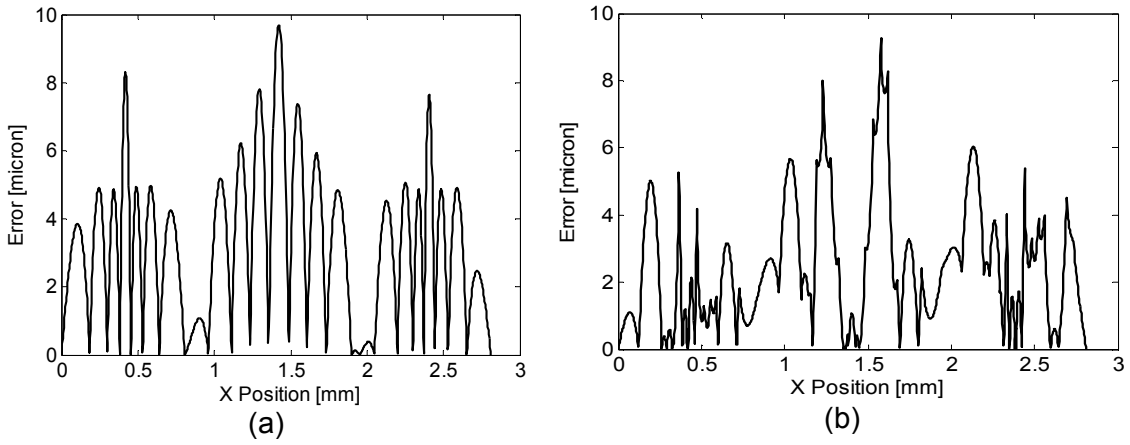

Figure 5.11: Algorithm error for (a) the EVF-NURBS method and (b) the VFIS method for a characteristic trial of the sine geometry test

The lobe pattern in the algorithm error plots in Figure 5.11 is due to the chord error. The EVF-NURBS result in Figure 5.11(a) consists exclusively of chord error, while the VFIS result in Figure 5.11(b) consists of a combination of chord error and interpolation error.

Total error is evaluated by processing the image of the sinusoidal cut. The first step of the image processing is to remove the background. Figure 5.12 is the image of the cut path after image processing to remove the background and application of the stitching algorithm. The image for an EVF-NURBS trial is shown in Figure 5.12(a) and the image for a VFIS trial is shown in Figure 5.12(b).

(a) (b)

Figure 5.12: Images of cut sine wave pattern after background image removal for Test 4, Trial 1 for (a) EVF-NURBS and (b) VFIS

The top edge of the image is then extracted and converted to X-Y coordinates. Figure 5.13 shows the X-Y coordinates of the extracted image overlaid on the X-Y coordinates of the ideal geometry.

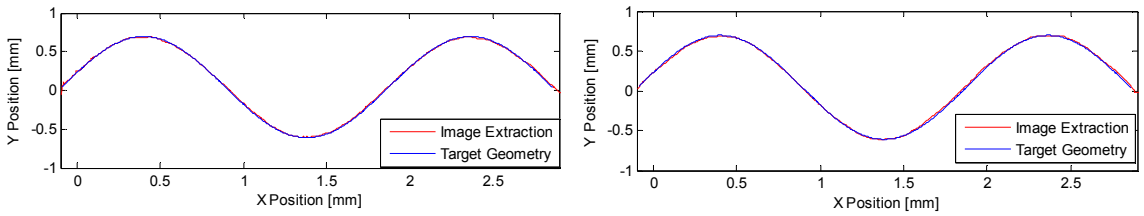

(a) (b)

Figure 5.13: Comparison of the extracted image with the target geometry for the characteristic trial for (a) EVF-NURBS and (b) VFIS

Total error can then be calculated. Plots of the total error for EVF-NURBS and VFIS trials are shown in Figure 5.14.

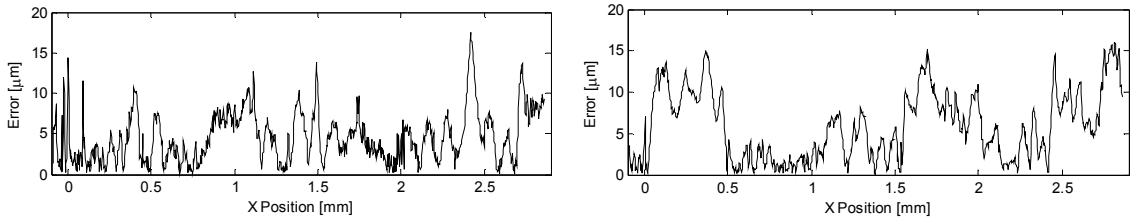

Figure 5.14: Total error in the final cut sine geometry for (a) the EVF-NURBS case and (b) the VFIS case

The maximum total error for each trial of each test was measured, and the mean and standard deviation calculated. The data are reported in Table 5.6.

Table 5.6: Maximum, mean, and standard deviation of error calculations for each trial of each test performed with EVF-NURBS and VFIS

Test		Trial 1		Trial 2		Trial 3	
		Max	Distribution	Max	Distribution	Max	Distribution
1	N	18.65	4.29±3.14	15.30	4.35±3.07	17.05	5.96±4.16
	V	20.13	6.22±4.54	20.71	4.95±4.39	17.05	5.44±4.19
2	N	17.71	4.36±3.17	15.53	4.39±3.15	16.86	4.08±3.22
	V	29.32	5.91±5.87	24.63	5.52±5.42	29.88	8.16±6.84
3	N	20.12	4.09±3.26	15.65	4.10±3.29	21.23	5.21±3.99
	V	17.77	5.39±3.95	15.62	4.65±3.17	15.38	5.33±3.31
4	N	17.51	4.55±3.09	23.80	5.40±4.53	16.47	4.54±3.10
	V	16.06	5.91±4.11	15.70	4.54±3.44	14.21	4.67±3.32
5	N	13.18	3.59±2.58	15.85	3.71±2.66	12.61	3.66±2.52
	V	17.57	4.91±3.78	16.83	4.26±3.45	16.06	4.61±3.61
6	N	17.91	5.57±3.77	22.45	5.78±5.24	21.95	5.53±4.84
	V	23.63	7.49±5.22	19.13	6.52±4.43	18.30	5.21±4.24
7	N	17.58	4.62±3.29	26.11	5.15±4.44	15.23	4.55±2.93
	V	18.42	5.74±4.67	21.79	6.99±5.77	23.24	6.10±5.07
8	N	13.37	4.19±2.91	14.18	3.97±2.70	16.33	4.22±3.13
	V	24.89	8.95±5.87	20.26	7.21±4.72	21.52	7.45±5.26
9	N	18.22	4.12±3.50	19.74	4.30±3.61	19.79	4.36±3.33
	V	21.57	8.61±5.23	25.52	11.12±6.63	34.74	11.13±7.52

The data from each trial are then processed to find the maximum error, mean, and standard deviation of total error for each test case. Max and mean algorithm error values are also calculated from the trajectory generation algorithm output. Algorithm

error is subtracted from total error to determine the process error. Since the algorithm output is deterministic, all of the variance in total error is attributed to variance in process error. The results of this error compilation are shown in Table 5.7.

Table 5.7: Compiled test data showing the maximum, mean, and standard deviation of total error, then broken down into algorithm error and process error

Test		Total Error [µm]				Algorithm Error [µm]		Process Error [µm]			
		Max	σ	Mean	σ	Max	Mean	Max	σ	Mean	σ
1	N	17.00	1.67	4.87	0.95	9.63	3.39	7.37	1.67	1.48	0.95
	V	19.32	1.93	5.54	0.59	9.28	2.33	10.04	1.93	3.21	0.59
2	N	15.57	0.94	4.28	0.31	9.59	3.71	7.24	0.94	0.57	0.31
	V	27.56	3.54	6.47	1.49	9.16	2.58	18.4	3.54	3.89	1.49
3	N	18.78	3.32	4.44	0.66	9.60	3.90	9.18	3.32	0.54	0.66
	V	16.54	1.19	5.18	0.32	9.17	2.98	7.37	1.19	2.2	0.32
4	N	18.90	4.37	4.80	0.52	9.68	3.26	9.22	4.37	1.54	0.52
	V	15.93	1.66	5.16	0.66	9.28	2.34	6.65	1.66	2.82	0.66
5	N	14.26	2.38	3.61	0.04	9.73	3.69	4.53	2.38	-0.08	0.04
	V	17.06	0.86	4.58	0.35	8.96	2.43	8.1	0.86	2.15	0.35
6	N	20.90	2.63	5.73	0.32	9.68	3.86	11.22	2.63	1.87	0.32
	V	20.21	2.97	6.27	1.15	9.08	2.76	11.13	2.97	3.51	1.15
7	N	20.67	7.47	4.88	0.52	9.66	3.13	11.01	7.47	1.75	0.52
	V	21.15	2.47	6.28	0.64	8.66	2.44	12.49	2.47	3.84	0.64
8	N	15.08	1.53	4.10	0.18	9.81	3.73	5.27	1.53	0.37	0.18
	V	22.22	2.39	7.87	0.94	9.31	2.30	12.91	2.39	5.57	0.94
9	N	19.44	1.09	4.28	0.14	9.78	3.87	9.66	1.09	0.41	0.14
	V	27.28	6.76	10.28	1.45	9.14	2.59	18.14	6.76	7.69	1.45

All values for algorithm error fall below 10 *µm*, thus it is verified that the maximum algorithm error for each test is below the imposed error limit. Maximum process error for the tests ranges from 4.5 *µm* to 18 *µm*.

The time benefits from VFIS are calculated from a time stamp command at the beginning and end of each trial. The variance in time is negligible, so only one time value is reported here for each test. The cutting times for EVF-NURBS and VFIS and the resulting percent time benefit are shown in Table 5.8.

Table 5.8: Cutting times reported for the NURBS and VFIS cutting tests and the calculated time benefit of VFIS for each test

Test	Λ	Time EVF-NURBS [s]	Time VFIS [s]	Percent Time Benefit of VFIS
1	0.33	2.500	1.969	21.26
2	0.20	2.700	2.076	23.10
3	0.14	2.736	2.113	22.79
4	0.50	2.612	1.803	30.96
5	0.30	2.600	1.982	23.77
6	0.21	2.712	1.928	28.90
7	0.67	2.600	1.664	35.99
8	0.40	2.500	1.941	22.38
9	0.28	2.600	1.956	24.76

In the derivation of the VFIS method presented in Chapter 4, it was predicted that the time benefits for VFIS should increase as the Λ ratio increases. To evaluate this prediction, the VFIS percent time benefit is plotted against the Λ value for each test. This plot is shown in Figure 5.15.

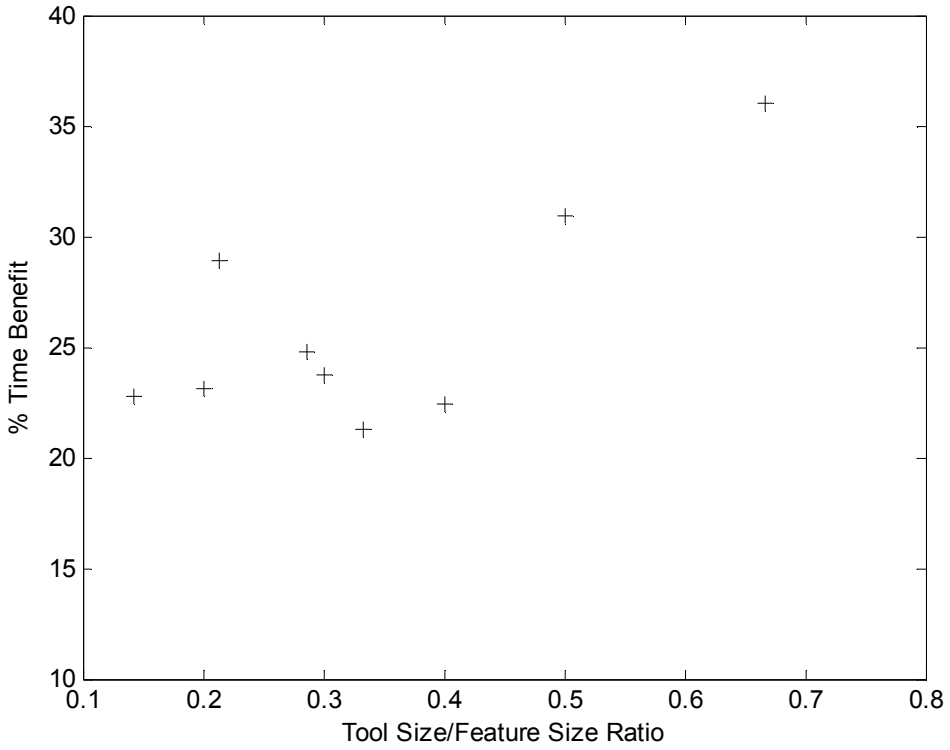

Figure 5.15: VFIS % time benefit vs Λ ratio for all sine tests performed

Figure 5.15 shows a trend similar to the numerical simulation results presented in Chapter 4. The general trend is increasing time benefit with increasing ratio, though several test points show deviation from this trend.

The algorithm output for the fan shape and airfoil shape toolpaths are shown in Figure 5.16 superimposed on the target toolpaths.

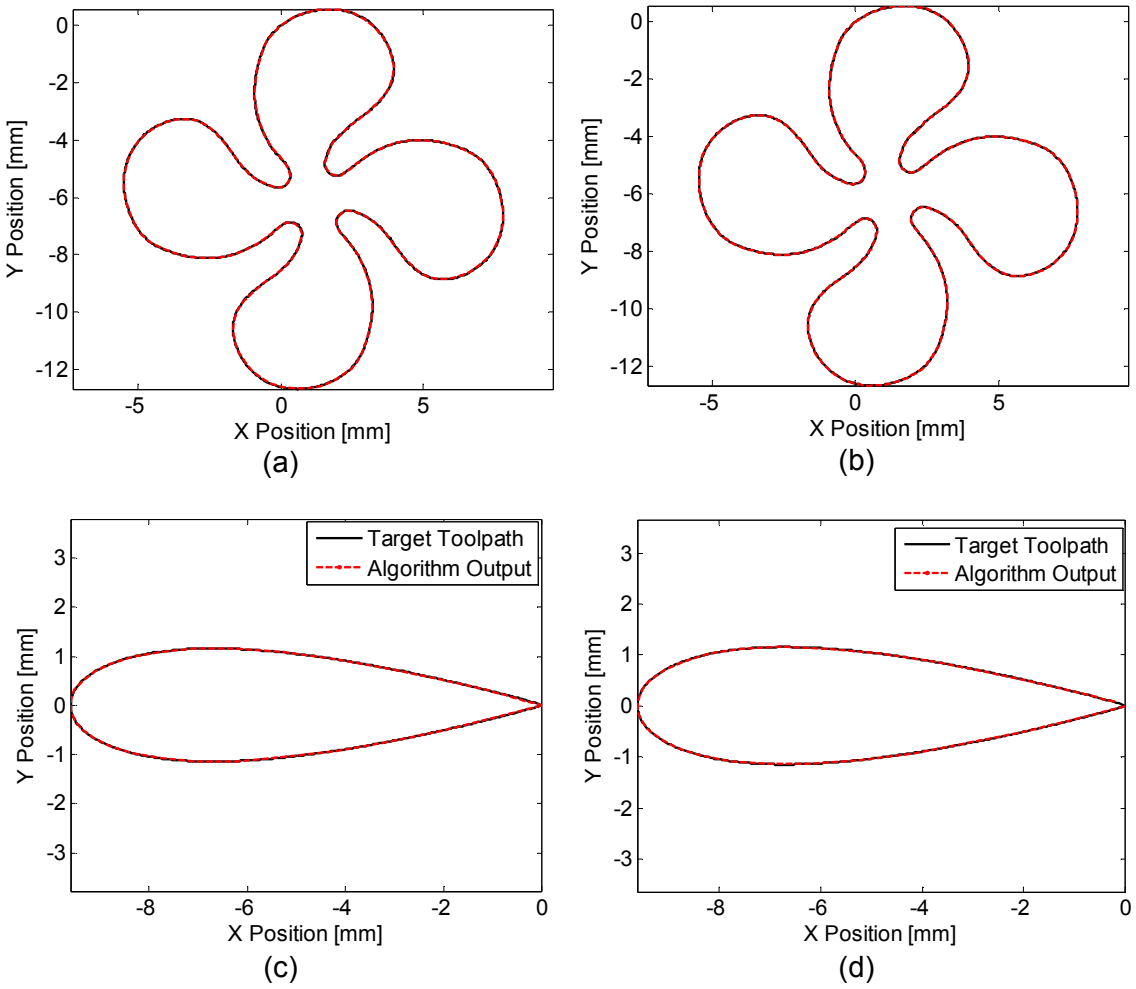

Figure 5.16: Fan shape trajectory generation algorithm output from (a) EVF-NURBS and (b) VFIS superimposed on the target tool path and airfoil shape trajectory generation algorithm output from (c) EVF-NURBS and (d) VFIS superimposed on the target tool path

The algorithm error for both interpolation methods is shown in Figure 5.17.

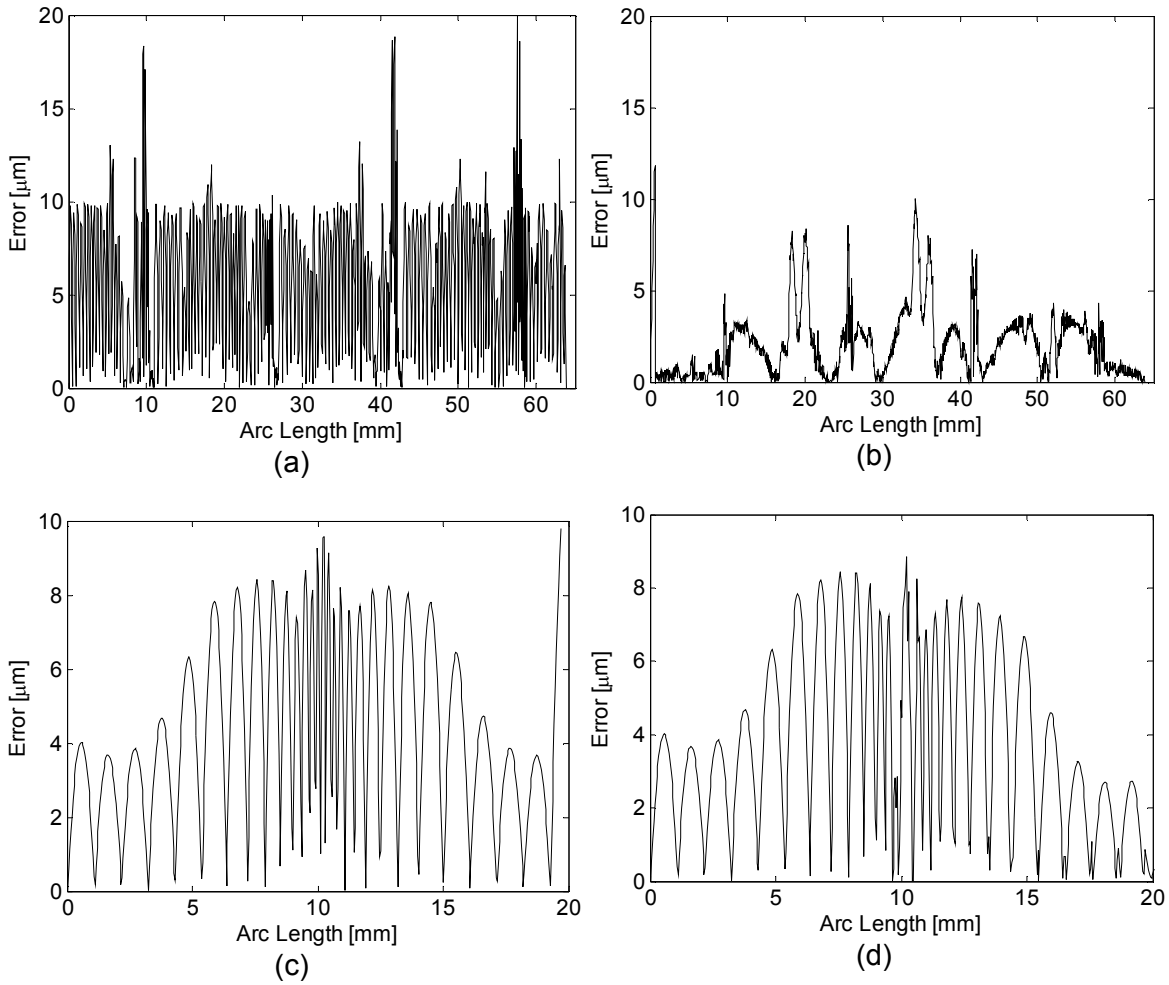

Figure 5.17: Algorithm error in the fan shape for (a) EVF-NURBS interpolation and (b) VFIS interpolation and in the airfoil shape for (c) EVF-NURBS interpolation and (d) VFIS interpolation

For the fan shape, the algorithm error for the EVF-NURBS method remains below the specified 10 *μm* over most of the arc length, except for certain locations in which the error spikes above the limit. Recall from Chapter 3 that the EVF-NURBS method can fail at inflection points. The fan geometry contains a number of inflection points which correspond to the locations of these error spikes. Algorithm error for the fan shape using the VFIS method appears to be much reduced compared to EVF-NURBS, while error for the airfoil appears similar in both methods. To evaluate this, the max and mean errors

are calculated for both shapes and for both methods. The results are shown in Table 5.9.

Table 5.9: Max and mean algorithm error for EVF-NURBS and VFIS trials of the airfoil and fan shapes

Test		Algorithm Error [μm] Max	Mean
Fan	N	20.75	5.94
	V	11.80	2.13
Airfoil	N	9.81	4.27
	V	8.85	3.66

The max and mean error values show a reduction in error with the VFIS method.

Cutting times are also evaluated for both shapes. The feedrate profiles for the EVF-NURBS and VFIS methods are shown in Figure 5.18.

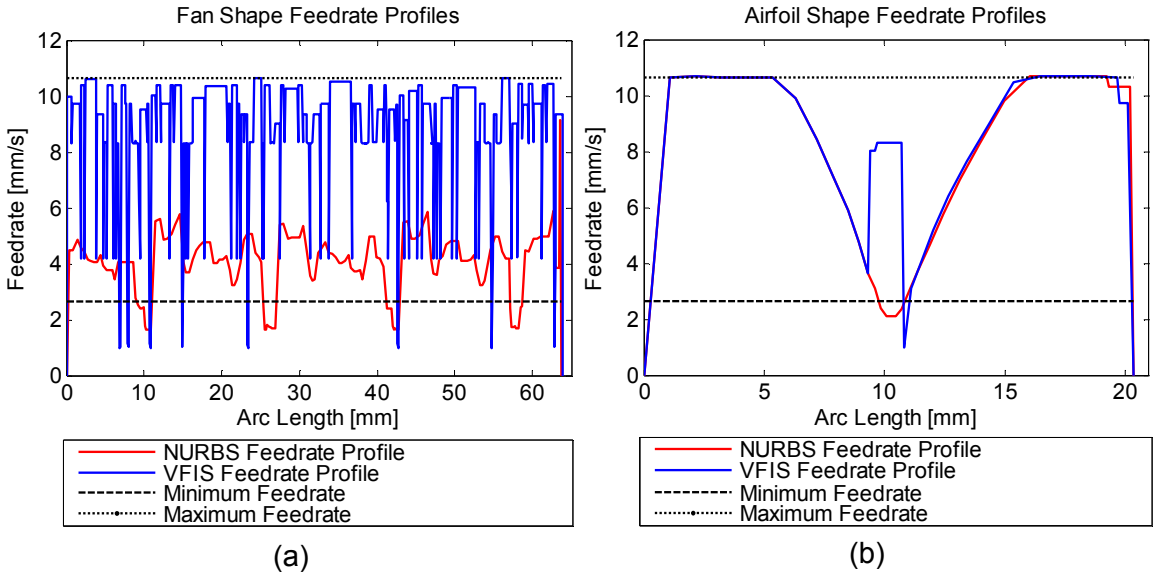

Figure 5.18: Feedrate profiles for (a) the fan shape and (b) the airfoil shape

The feedrate profiles indicate that VFIS identifies many more segments in the fan shape than in the airfoil shape, indicated by the widely varying VFIS feedrate in the fan shape

relative to the airfoil shape. For both shapes, the EVF-NURBS feedrate profile drops below the minimum feedrate over a significant portion of the curve. The VFIS profile, however, drops below the minimum only in transitions from circular segments to EVF-NURBS segments where the sampling rate is changed. The higher feedrates available for VFIS indicate a time benefit. This benefit is calculated and recorded in Table 5.10.

Table 5.10: Cutting time for EVF-NURBS and VFIS for the fan and airfoil shapes

Test	Λ	Time EVF-NURBS [s]	Time VFIS [s]	Percent Time Benefit
Fan	0.29	18.830	8.686	53.87
Airfoil	0.22	3.384	2.828	16.43

After the shapes have been cut, a small portion of the fan shape tool path in a location of minimum radius of curvature is scanned with the Zygo white light interferometer to compare the surface roughness in the bottom of the channel. Figure 5.19 and Figure 5.20 show the resulting images.

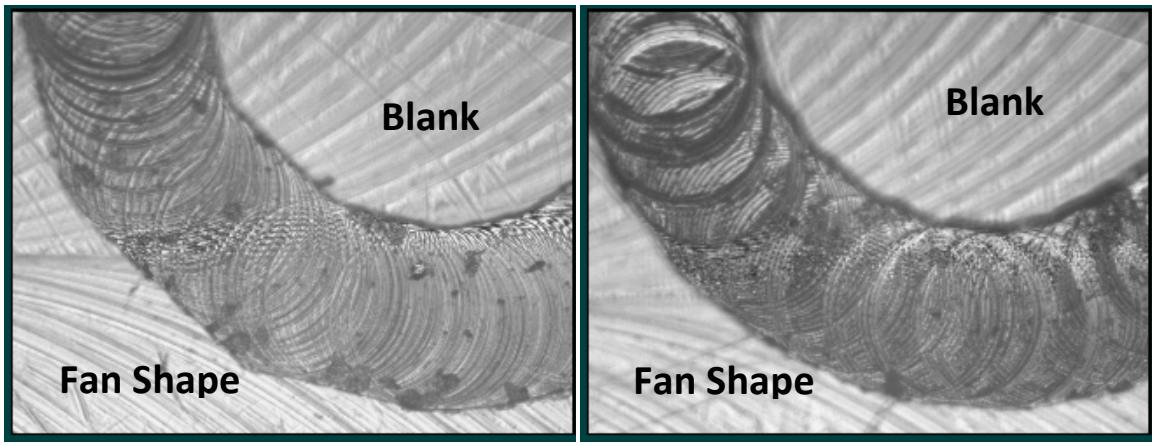

(a) (b)

Figure 5.19: Image of the point of minimum radius of curvature for (a) EVF-NURBS interpolation and (b) VFIS interpolation

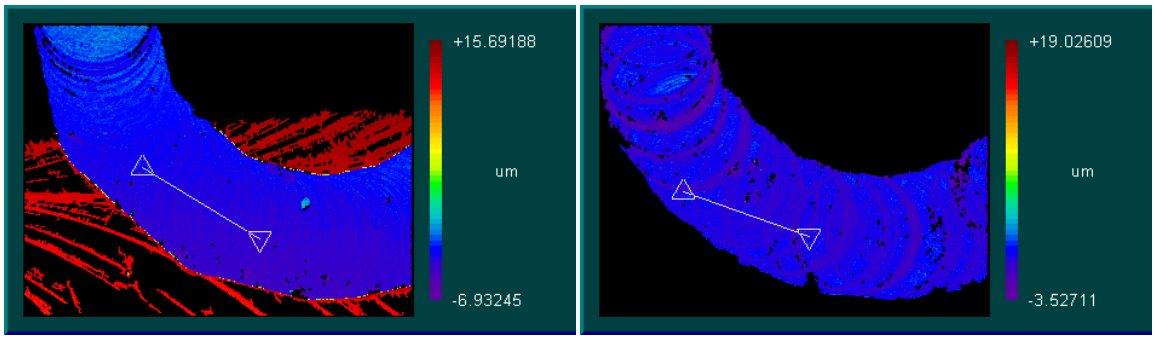

(a) (b)

Figure 5.20: Interferometer scan of the point of highest curvature for the fan shape made using (a) EVF-NURBS and (b) VFIS

Figure 5.19 and Figure 5.20 show the difference in chord error between the EVF-NURBS and VFIS methods. In the EVF-NURBS image, chord error is clearly visible, particularly on the cutting edge toward the fan shape. In the VFIS image, chord error is not visible, despite the higher feedrate.

The feedrate, chipload, and surface roughness for this point of the cutting path for both EVF-NURBS and VFIS are reported in Table 5.11.

Table 5.11: Feedrate, chipload, and surface roughness for EVF-NURBS and VFIS at the point of highest curvature in the airfoil shape

Characteristic	EVF-NURBS	VFIS
Feedrate [mm/s]	2.2	9.5
Chipload [µm]	0.8	3.6
Surface Roughness Ra [nm]	262	355

The VFIS method is found to have a higher surface roughness, due to the higher feedrates and, thus, larger chipload.

5.6 Sensitivity to the Minimum Chip Thickness Parameter

The actual minimum chip thickness is dependent upon many parameters, including material properties, tool edge condition, and surface speed. The VFIS algorithm has adopted an approximation of this effect that assumes the minimum chip thickness is 30% of the edge radius of the tool (r_e), following reported studies [8, 12]. However, other studies have reported minimum chip thickness values in the range of 10% of the re up to as high as 50% of the re. A sensitivity study was conducted using the fan shape and airfoil geometries in order to assess the impact of the minimum chip thickness assumption on the performance of the VFIS algorithm. The minimum chip thickness parameter was varied between 10% and 50% of the edge radius. The result of the sensitivity study on the fan shape and the airfoil shape are presented in Table 5.12 and Table 5.13, respectively.

Table 5.12: Time benefit of VFIS with varying minimum chip thickness for the fan shape

Minimum Chip Thickness	EVF-NURBS Time [s]	VFIS Time [s]	VFIS Time Benefit
$0.1r_e$	18.8301	8.6804	53.90
$0.2r_e$	18.8301	8.7277	53.65
$0.3r_e$	18.8301	8.6861	53.87
$0.4r_e$	18.8301	8.6808	53.90
$0.5r_e$	18.8301	8.7662	53.45

Table 5.12 indicates that the time benefits of VFIS for the fan shape are insensitive to variations in minimum chip thickness, with a variance in time benefits of only 0.0398. The insensitivity of VFIS time benefits for this shape is due to the significant portion of the curve which is segmented by Curvature-Based Segmentation. Changes to minimum chip thickness only affect the benefits available from Stability-Based Segmentation. When the minimum chip thickness is decreased, fewer segments are identified by Stability-Based Segmentation. However, in the fan shape, the segments identified by

Stability-Based Segmentation are also nearly circular. As fewer segments are identified by SB Segmentation, more segments are identified by CB Segmentation. As a result, variations in minimum chip thickness have little effect on total time benefits of VFIS.

In contrast, the airfoil shape shows VFIS benefits primarily due to stability-based segmentation due to the constantly-varying radius of curvature in this shape. The time benefits for the airfoil shape with varying minimum chip thickness are shown in Table 5.13.

Table 5.13: Time benefit of VFIS with varying minimum chip thickness for the airfoil shape

Minimum Chip Thickness	NURBS Time [s]	VFIS Time [s]	VFIS Time Benefit
$0.1r_e$	3.3840	3.3840	0.00
$0.2r_e$	3.3840	3.3840	0.00
$0.3r_e$	3.3840	2.8161	16.78
$0.4r_e$	3.3840	2.8525	15.71
$0.5r_e$	3.3840	2.6882	20.56

Table 5.13 indicates that the time benefits of VFIS for the airfoil shape are highly sensitive to variations in minimum chip thickness, with a variance of 97.0564. This sensitivity is due to the large portion of the curve identified by SB Segmentation relative to CB Segmentation. When the minimum chip thickness is small, as in the $0.1r_e$ and $0.2r_e$ entries in Table 5.13, there is no VFIS time benefit for the airfoil, because there are no regions of the curve in which the maximum feedrate falls below the minimum. As the minimum chip thickness becomes larger, a larger portion of the maximum feedrate profile falls below the minimum. This results in both a greater number of identified segments and a greater length of segments. Due to feedrate variations between segments and the greater interpolation error which occurs with greater segment length, the effect of the increased minimum chip thickness can cause either an increase in time

benefits (as in the change from $0.4r_e$ to $0.5r_e$) or a slight decrease (as in the change from $0.3r_e$ to $0.4r_e$), depending on the curvature properties of the curve.

Summary

The trajectory generation methods of EVF-NURBS and VFIS were experimentally evaluated using cutting trials performed on a low-cost mesoscale machining center detailed in the Appendix. The evaluations were performed on a set of sinusoidal geometries and on fan and airfoil shapes. The VFIS method was found to provide both reduced process error and decreased cutting time relative to the VF-NURBS method. The time benefits achieved ranged from 21%-36% for the sinusoidal geometries, with higher time benefits generally at higher values of Λ. The fan shape trial showed a VFIS time benefit of 54%, and the airfoil a benefit of 16%.

Chapter 6: Tool Size Optimization for Enhanced Productivity

In the previous chapters, segmentation and trajectory generation methods were created to improve productivity by capitalizing on the increased importance of sampling rate in micromilling processes. In this chapter, it is recognized that productivity in micromilling is not exclusively dependent upon achievable sampling rate, but also highly dependent upon tool size. In the current optimization literature, tool size is typically assumed to be a single known value chosen prior to the optimization process. Tool size is typically chosen as the largest tool that fits in all features, or according to expert knowledge. However, due to scale effects, the largest tool which fits in all features may not be optimal in terms of productivity. Also, expert knowledge which is applicable at the macroscale is not applicable to the microscale due to scale effects. In response to this challenge, in this chapter a preliminary investigation will be made into possible methods of choosing an optimal tool size in light of the scale effects that have been identified.

Two independent optimization schemes will be introduced here: (1) maximal material removal rate with minimal error and (2) minimal machining time under constraints to reduce dynamic effects. In the first optimization method, tool size will be allowed to be any value, and the optimal tool size will be found which minimizes cutting time while constraining both chord error and tool size error. In the second method, scale effects are integrated into an optimization process to choose tool sizes, feedrate profiles, and spindle speed profiles for minimal machining time under constraints for precision and achievability given spindle power constraints and the requirement of constant chipload.

Each method will be presented and evaluated, followed by a discussion of microscale tool size optimization as it relates to micromilling productivity.

6.1 Optimization Scheme for Maximal MRR with Minimal Error

In this first optimization scheme, an objective function *J* is derived to minimize total error along the toolpath $e(u_s)$, maximize material removal rate $MRR(u_s)$, and minimize number of tool changes c_t, with respect to tool size and feedrate according to user-defined weights w_1, w_2, and w_3. The objective function is shown in Eq. (1).

$$J = w_1 e(u_s) + w_2 \frac{1}{MRR(u_s)} + w_3 c_t \tag{1}$$

In order to maintain stability, the objective function is subject to the minimum chip thickness constraint as in Eq. (2).

$$f(u_s) > 0.3 r_e(u_s) n(u_s) N(u_s) \tag{2}$$

Two sources of error are considered in this optimization: chord error $e_c(u_s)$ and tool size error $e_t(u_s)$. Total error along the desired tool cutter path is the sum of these two errors. However, tool size error is present only in locations where the tool radius is larger than the radius of curvature. Conversely, chord error is present only where the tool radius is smaller than the radius of curvature. In order to express this in the objective function, a Boolean function is defined as in Eq. (3).

$$x(u_s) = \begin{cases} 1 & \text{for } \rho(u_s) > r(u_s) \\ 0 & \text{otherwise} \end{cases} \tag{3}$$

The equation for chord error as previously derived is a means of calculating maximum chord error along the curve. For implementation in this objective function, an expression is needed for chord error at any point along the curve. Methods currently used for

calculating chord error consider only maximum chord error. To approximate chord error at any point along the curve, this study introduces a multiplier, $g(u_s)$, which utilizes a sinusoidal modulation of the chord error between sampling instants. The sinusoidal modulation is utilized as its characteristics of zero-value at the endpoints, maximum at the midpoint and continuous, smooth increasing and decreasing magnitude provide an intuitive approximation of the chord-error along the path. The form of the multiplier is given in Eq. (4).

$$g(u_s) = \sin^2\left(\frac{\sqrt{\dot{x}(u_s)^2 + \dot{y}(u_s)^2}}{f(u_s)}\frac{u_s}{T_s}\pi\right) \tag{4}$$

By combining Eqs. (1-4) and previously calculated expressions for chord error, tool size error, and material removal rate, a process optimization model modified for the microscale is determined as in Eq. (5).

$$\begin{aligned} J &= w_1\left(x(u_s)e_c(u_s)\sin^2\left(\frac{\sqrt{\dot{x}(u_s)^2 + \dot{y}(u_s)^2}}{f(u_s)}\frac{u_s}{T_s}\pi\right) + \left(-x(u_s)+1\right)e_t(u_s)\right) \\ &+ w_2\frac{1}{\left(avg\left(r(u_s)*f(u_s)\right)\right)} + w_3 c_t \\ e_c(u_s) &= -\sqrt{\frac{-\left(f(u_s)*f(u_s)\right)\left(T_s^2\right)}{4} + \left(\rho(u_s) - r(u_s)\right)^2} + \rho(u_s) - r(u_s) \\ e_t(u_s) &= \rho(u_s) + r(u_s)\cos\phi\tan\phi - \frac{\rho(u_s)}{\cos\phi} + r(u_s)\cos\phi - r(u_s) \end{aligned} \tag{5}$$

The optimization was implemented on two geometries shown in Figure 6.1 as a preliminary verification of the optimization approach. The first target geometry is defined as one period of a sine wave of amplitude 30 *mm* and a period of 2π *mm*. This shape has a minimum radius of curvature of 625 *μm*. The second geometry is a quartic function of similar dimensions, with a minimum radius of curvature of 668 *μm*. These shapes were chosen in order to illustrate the benefits of the optimization process in the

case of a large value of Λ. For each geometry, five tests were performed, each test employing a different set of values for weights w_1 and w_2. The tests were performed over a constrained domain of only one allowable tool size and feedrate for the entire tool path. For all cases, the sampling time for the control loop was set at 2.0 *ms*, and a two-flute endmill with a cutting edge radius of 3 *μm* was assumed with a spindle speed of 250,000 *rpm*.

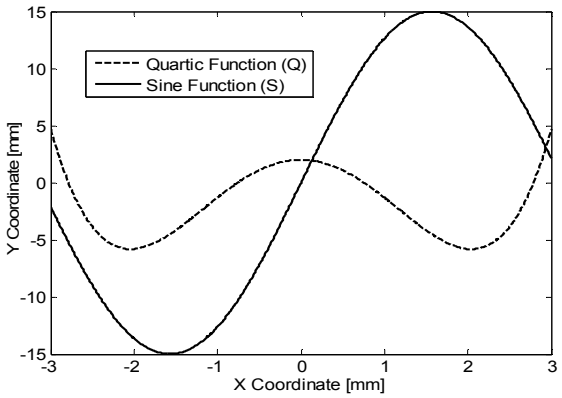

Figure 6.1: Two target geometries for preliminary verification of the tool size optimization scheme for minimal error

Available tool sizes for the test case were restricted to range in diameter from 10 *μm* to 100 *μm* increasing in 10 *μm* increments. Feedrates were allowed to range from 400 *mm/min* to 1000 *mm/min* in 10 *mm/min* increments.

Test cases and the results of all tests run are summarized in Table 6.1, where average MRR values have been normalized for a fixed axial depth of cut. These calculations assume that parameters not specified, such as axial depth of cut, are maintained at a value reasonable for the scale [19].

Table 6.1: Summary of optimization cases run for the tool size optimization scheme for minimal error

Test No.	w_1	w_2	Optimal Tool Size [*mm*]		Optimal Feedrate [*mm/min*]		Max. Chord Error [μm]		Avg. MRR [mm^2/min]	
			Tool Path							
			Q	*S*	*Q*	*S*	*Q*	*S*	*Q*	*S*
1	1	1	0.100	0.100	1000	890	12.60	9.100	49.50	44.50
2	10	1	0.091	0.090	720	750	3.700	4.000	32.76	33.75
3	100	1	0.090	0.061	450	750	1.300	2.200	20.25	22.87
4	1000	1	0.043	0.033	450	450	0.624	0.563	9.675	7.425
5	1	0	0.005	0.005	450	450	0.439	0.439	1.125	1.125

Test 1 in Table 6.1 indicates that when the weights of the objective function are equal, a large tool size and allowable feedrate are determined to be optimal, resulting in a relatively large chord error and high MRR. As weight on the error is increased in tests 2-4, optimal feedrate and tool size are both decreased, resulting in lower chord error and lower MRR.

A larger tool size is chosen as optimal for the quartic function as for the sine function in tests 2, 3, and 4 in Table 7.1. This is due to the larger minimum radius of curvature in the quartic function, thus providing a smaller ratio of tool size to feature size. The lowest error attainable can be found by setting w_1 to 1 and w_2 to 0, as in test 5. In this case, the smallest tool size available is chosen as optimal. The optimal feedrate is not the lowest feedrate available, however, because the lowest feedrate results in unstable operation due to the minimum chip thickness effect. The lowest stable feedrate, 450 *mm/min*, is determined to be optimal, resulting in the lowest achievable chord error, but also the lowest material removal rate.

Figure 6.2 is a plot of the objective function value with tool size and feedrate for Test 4. The vertical wall at 450 *mm/min* represents the feedrate limit imposed by the minimum chip thickness requirement. Within the stable range of feedrates, a large tool size and high feedrate result in the maximum value for the objective function. This is due to the

compounding effects of high tool size to feature size ratio and high feedrate on chord error. The optimal tool size and feedrate are determined by the minimum of the pareto surface.

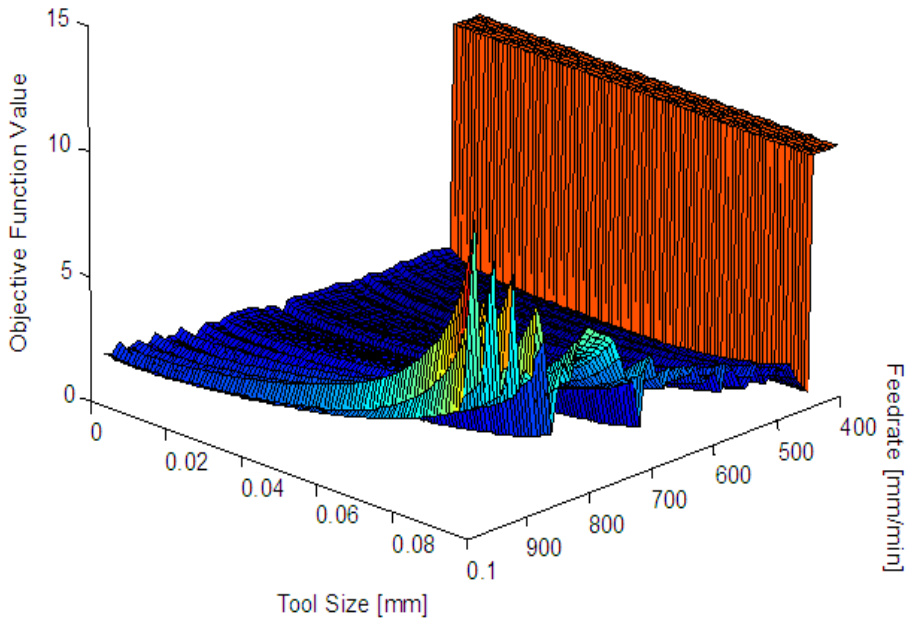

Figure 6.2: Objective function value plotted with tool size and feedrate for sine wave Test Case 4 applying the tool size optimization scheme for minimal error

6.2 Optimization Scheme for Minimal Machining Time with Constraints to Minimize Dynamic Effects

In this second optimization scheme, tool size will be found which minimizes cutting time while minimizing dynamic effects. In pursuit of the objective to minimize dynamic effects, feedrate and spindle speed will be related so as to maintain a constant chipload. A constant chipload is desirable in order to decrease cutting force variations, and also in order to maintain consistent surface roughness. As feedrate is reduced in regions of high curvature, spindle speed must also be decreased in order to maintain a constant

chipload. A reduction of spindle speed results in a reduction of available spindle power. At the same time, the specific cutting energy of the material increases as chip thickness becomes small, increasing the power required. As a result, a power limitation is encountered in high-precision micromilling. Thus, the spindle power characteristics impose a further restriction on available tool sizes.

In macroscale milling, tool size and material removal rate are related due to the dependence of optimal axial depth of cut and chipload on tool size [5]. At the microscale, there are additional relationships between material removal rate, precision, and tool size that need to be considered. In this optimization scheme, the existence of tool size error will not be considered; instead, a restriction is placed on choice of tool size such that the finishing tool must be able to fit in the smallest feature without gouging. If the arc length of the smallest feature is only a small portion of the total geometry arc length, then use of this small tool to create the entire geometry would result in a reduction of material removal rates achievable.

Regardless of the strategy employed in the micromilling process, the tool path can be divided into two tool-path segments: a path segment in which the tool does not touch the geometry, and a path segment in which the tool does touch the geometry. Here, the path segment in which the tool touches the geometry will be referred to as ‘the final tool-pass’. See Figure 6.3.

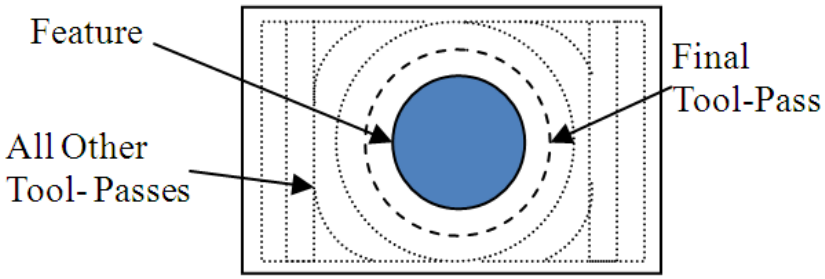

Figure 6.3: Illustration of the final tool-pass and all other tool-passes

All tool-passes besides the final tool-pass are not subject to the restrictions on chord error previously mentioned, but can be performed at a constant feedrate equal to the maximum feedrate allowable by physical limitations, with the largest tool available. The final pass, however, is subject to all of the constraints previously mentioned: tool size error and chord error constraints, and power constraints. If the tool used to perform the final tool-pass is large relative to the geometry feature size, the tool will leave some tool-size error or will have to feed very slowly in order to satisfy chord error constraints. To maintain constant chip thickness, the spindle speed will have to decrease, violating the power limitation. If a small tool is used for the final pass, the cutting time will be long because a small tool requires a small axial depth of cut.

In the algorithm developed here, a combination of two tools is allowed for the final tool-pass. The optimal combination of a larger tool and smaller tool, each performing the final tool-pass on a portion of the total geometry arc length, is determined which minimizes cutting time within precision bounds.

Cutting time can be expressed as in Eq. (6), where M is the amount of material to be removed.

$$t = \frac{M}{MRR_{avg}} \tag{6}$$

The amount of material to be removed can be approximated as in Eq. (7), where *h* is the height of the material, s_{max} is the arc length of the geometry, and *Y* is the width of material to be removed. By multiplying distance in three dimensions, we obtain the volume of material to be removed *M*.

$$M = hs_{\max}Y \tag{7}$$

When milling along a straight line with a constant feedrate, material removal rate is defined as the product of feedrate, axial depth of cut, and radial depth of cut. In order to account for variable feedrate along the path, the average material removal rate can be found by integrating material removal rate along the path, and dividing by the total path length. To account for curvature along the path, velocity of the tool cutting edge must be used instead of feedrate. In light of these modifications, the equation for average material removal rate is shown in Eq. (8).

$$MRR_{avg} = \frac{1}{s_{\max}} \int_0^{s_{\max}} d_a d_r V_c(s) ds \tag{8}$$

In Eq. (8), V_c is the velocity of the tool cutting edge.

Here it is assumed that the axial depth of cut, the radial depth of cut, and the feed per tooth are each a constant proportionality of tool radius, as suggested by the Machinery's Handbook [5] and by Sreeram, et al. [49], who found that an axial depth of cut equal to the tool's diameter results in maximal tool life. The chip thickness constant may be chosen for acceptable surface roughness, as suggested by Dimov, et al. [3]. These constant proportional relationships are shown in Eq. (9).

$$d_a = Ar$$
$$d_r = Br \tag{9}$$
$$f_t = Cr$$

Values of *A*, *B*, and *C* are chosen according to surface finish, tool life, and cutting force constraints. It is assumed in this study that the user has chosen appropriate constant values according to the quality requirements specified for the application.

In order to maintain a constant chipload as feedrate is varied, spindle speed is varied with feedrate. In order to account for this in the objective function, cutter edge speed is expressed as shown in Eq. (10).

$$V_c(s) = nN(s)\frac{\rho - r}{\rho} \tag{10}$$

Eqs. (10), (9), (8), and (7) are substituted into Eq. (6) to obtain an expression for cutting time as expressed in Eq. (11).

$$t_n = \frac{hs_n Y}{\frac{1}{s_n}\int_0^{s_n} Ar_n Br_n Cr_n nN(s)\frac{\rho - r}{\rho}\,ds} \tag{11}$$

Total time is the sum of the times required for the final pass of each tool, as shown in Eq. (12).

$$t = t_1 + t_2 = \frac{hs_1 Y}{MRR_{avg_1}} + \frac{hs_2 Y}{MRR_{avg_2}} \tag{12}$$

In Eq. (12), s_1 and s_2 are each a portion of the total geometry arc length, so that the sum of s_1 and s_2 is equal to the total geometry arc length s_{max}. Then, time can be minimized by maximizing the combined average material removal rate over the two regions s_1 and s_2.

Average material removal rate can be maximized by adjusting *r* and *N(s)* within the allowable range. Allowable range is defined by two constraints: an error constraint and a spindle power constraint.

1. Chord error constraint: the chord error constraint is enforced as a restriction on spindle speed. The constraint is shown in Eq. (13) if radius of curvature is tool-side, and in Eq. (14) otherwise.

$$N(s) \le \frac{2}{T_s nCr}\sqrt{\left(\rho(s)-r\right)^2+\left(\rho(s)-r-\delta\right)^2} \tag{13}$$

$$N(s) \le \frac{2}{T_s nCr}\sqrt{\left(\rho(s)+r\right)^2+\left(\rho(s)+r-\delta\right)^2} \tag{14}$$

2. Spindle power constraint: required power is expressed as in Eq. (15), where *u* is specific cutting energy.

$$P(s) = MRR(s)u \tag{15}$$

The value of specific cutting energy depends exponentially on the workpiece material and chip thickness [50]. Required power must be less than or equal to available power at a given spindle speed. Letting available power at a given spindle speed be represented by *P(N)*, the constraint can be expressed as in Eq. (16).

$$MRR \times u \le P(N) \tag{16}$$

In order to minimize time, the constants are factored out of Eqs. (11) and (12) and the resulting equation is inverted, leaving the objective function for maximization. The objective function to be maximized is shown in Eq. (17).

$$J = \left[\frac{s_1^2}{\int_0^{s_1} {r_1}^3 N(s)ds} + \frac{s_2^2}{\int_0^{s_2} {r_2}^3 N(s)ds}\right]^{-1} \tag{17}$$

To determine the optimal tool sizes r_1 and r_2, Eq. (17) should be maximized. This maximization requires the determination of values for s_1 and s_2. In this study, these values are determined by maximizing material removal rate at each point in the curve s_i. If tool 1 would provide superior material removal rate at point s_i, then point s_i is said to belong to the segment s_1. If tool 2 has a higher value of material removal rate at s_i, then s_i belongs to segment s_2. Additionally, if a point results in gouging with the larger tool, the point is assigned to the smaller tool. In the next section, an algorithm is proposed to achieve the optimization.

The optimization is carried out as follows. For every available tool size, for every point along the geometry path, calculate the fastest spindle speed which satisfies the chord error and power constraints. If no spindle speed exists which satisfies both constraints, or if the spindle location point is a distance of less than one tool radius away from any point in the geometry (gouge), then the fastest spindle speed is taken to be 0. For each tool size, calculate the *MRR(s)* profile given the spindle speed profile determined previously. For each combination of two tool sizes, create a composite *MRR(s)* profile defined by taking the maximum *MRR(s)* value at each point. Points at which the two profiles cross indicate the arc length segments at which each tool should be used. If the composite *MRR(s)* profile has a zero point anywhere along the curve, eliminate the corresponding tool size combination. For each composite *MRR(s)* curve, calculate the area under the curve and divide it by the total arc length. The maximum result is taken. The corresponding tool size combination is optimal. The optimal feedrate and spindle speed profiles are those which corresponds to the identified optimal tool sizes. Corresponding arc segments for each tool are indicated from the points at which the *MRR(s)* profiles cross. A flow chart of the algorithm is shown in Figure 6.4.

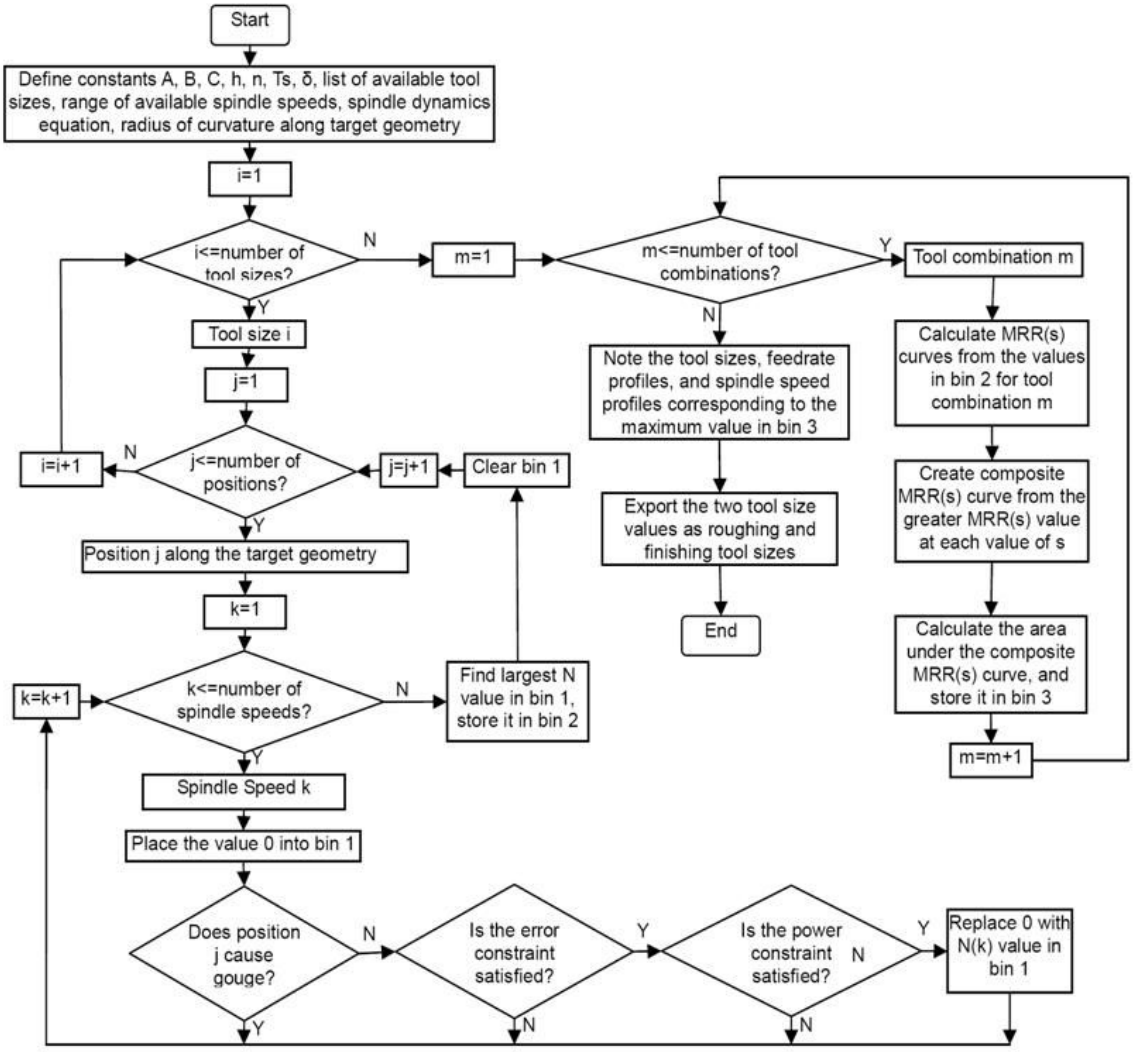

Figure 6.4: Flow chart for the tool size optimization algorithm for minimum machining time and minimal dynamic effects

A numerical example is presented here, illustrating the implementation of the method and results of the optimization algorithm. The algorithm is applied to an involute gear shape as shown in Figure 6.5. In this shape, the minimum radius of curvature is 0.15 *mm* and a height of 1 *mm*. For this example, the gear will be feature milled with a spindle capable of speeds up to 80,000 *rpm* controlled with a controller capable of a 1 *ms* loop sampling rate.

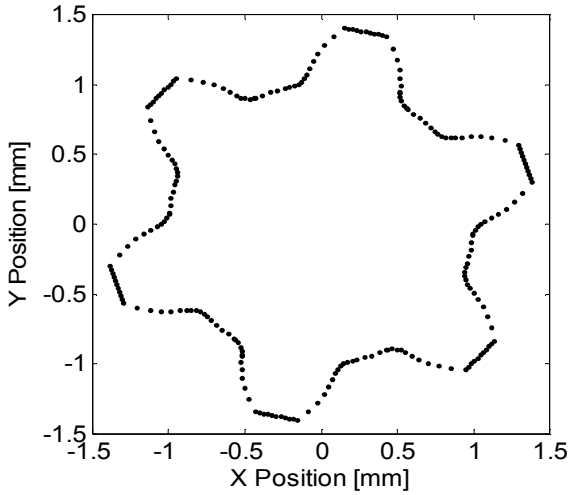

Figure 6.5: Gear shape for numerical implementation of the tool size optimization algorithm for minimal machining time and minimal dynamic effects

The torque and power characteristics of the spindle model ASTRO-E 800Z were obtained from the NSK America, and is shown in Figure 6.6 [51].

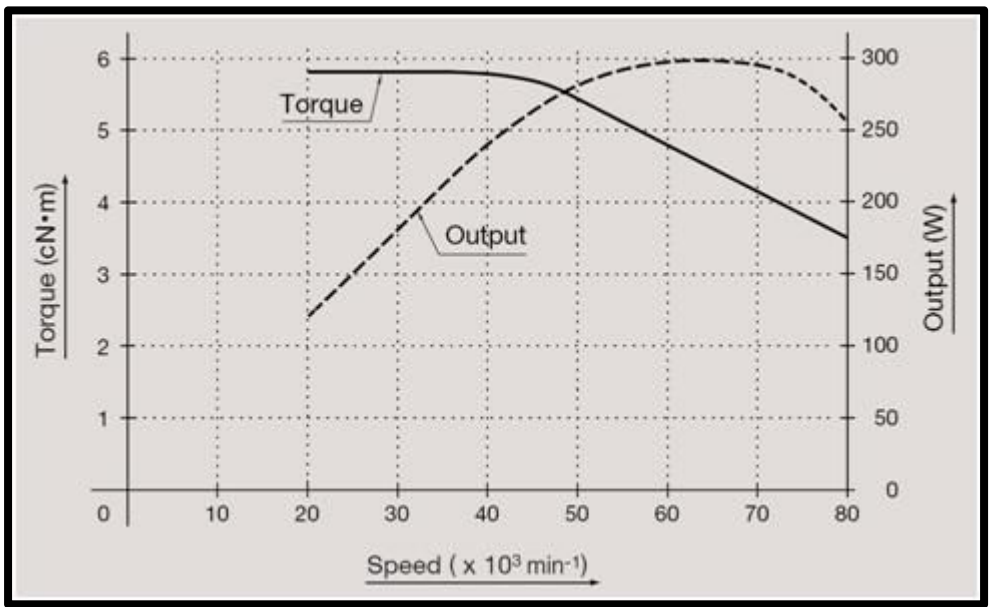

Figure 6.6: Spindle torque and power characteristics [51]

The spindle power curve shown in Figure 6.6 is fit with a second-order polynomial to obtain the *P(N)* equation necessary for the optimization. The equation determined from the fit is shown in Eq. (18).

$$P(N) = -0.0004N^2 + 0.7752N - 107.0714 \tag{18}$$

Aluminum is chosen as the workpiece material to obtain the specific cutting energy equation. The final form of the spindle power constraint for this example is shown in Eq. (19).

$$N(s_i, r_j) \leq \frac{P(N(s_i r_j))}{(Ar_j Br_j Cr_j n)10^{-0.38-0.4\log(Cr_j)}} \tag{19}$$

Available tool sizes considered for this operation range from 0.0254 *mm* to 2.3825 *mm*, tool sizes sold by Performance Microtool [4]. The optimization is performed for a range of constant values. For all cases, the material width *Y* is set at 100 *μm* and the axial depth proportionality *A* is set to 2, as suggested by Sreeram, et al. in [49]. Values considered for the optimization and the algorithm outputs are summarized in Table 6.2.

Table 6.2: Summary of test cases and results from preliminary evaluation of the tool size optimization scheme for minimal cutting time and minimal dynamic effects

Case	Material	C	δ [μm]	Tool Radius 1 [mm]	Tool Radius 2 [mm]	MRR [mm^3/s]
1	Al	0.005	0.01	1.1913	0.1016	0.7010
2	Al	0.020	0.01	1.1913	0.1016	1.1808
3	Al	0.060	0.01	1.1430	0.1016	1.0456
4	Al	0.100	0.01	0.7937	0.0762	0.7405
5	Al	0.020	0.10	1.1913	0.1016	2.6660
6	Al	0.060	0.10	1.1913	0.1016	3.7297
7	Alloy Steel	0.005	0.01	1.1913	0.1016	0.7010
8	Alloy Steel	0.10	0.01	0.6985	0.0762	0.6430

Referencing Table 6.2, the optimal finishing tool is not always the largest tool to fit in the smallest feature, due to power constraints. The choice of the optimal finishing tool exhibits greater variation amongst the cases than the optimal choice of roughing tool.

The optimal roughing tool choice becomes small when chipload becomes large and allowable chord error becomes small, as can be seen by comparing cases 2, 3, and 4.

Comparison of cases 1 and 2 indicates that an increased chip thickness causes an increased optimal material removal rate, while comparison of cases 2 and 3 indicate that increased chip thickness causes a decreased optimal material removal rate. This apparently indicates that there exists an optimal chip thickness for maximal material removal rate. However, there are additional complexities that need to be considered in choosing optimal chip thickness, such as the forces, to prevent excessive tool deflection and tool breakage. The material choice has a more significant effect on the optimal tool choice when the chip thickness proportionality is large and the chord error limitation is small, as can be seen from comparing cases 7 and 8 to cases 1 and 4, because these parameters cause power limitation to become significant. It is expected that material choice would be a more significant factor in optimal tool choice for a spindle of higher speed and lower power capability. Greatest increase in achievable material removal rate can be achieved by increasing the maximum allowable chord error, as illustrated by comparing cases 2 and 3 with cases 5 and 6. Throughout all cases, there is significantly more variation in the determination of optimal finishing tool than in choice of roughing tool.

The Pareto surface for maximization obtained for case 3 is shown in Figure 6.7, and is a characteristic result. The optimal tool size combination is determined from the maximum point on the Pareto surface.

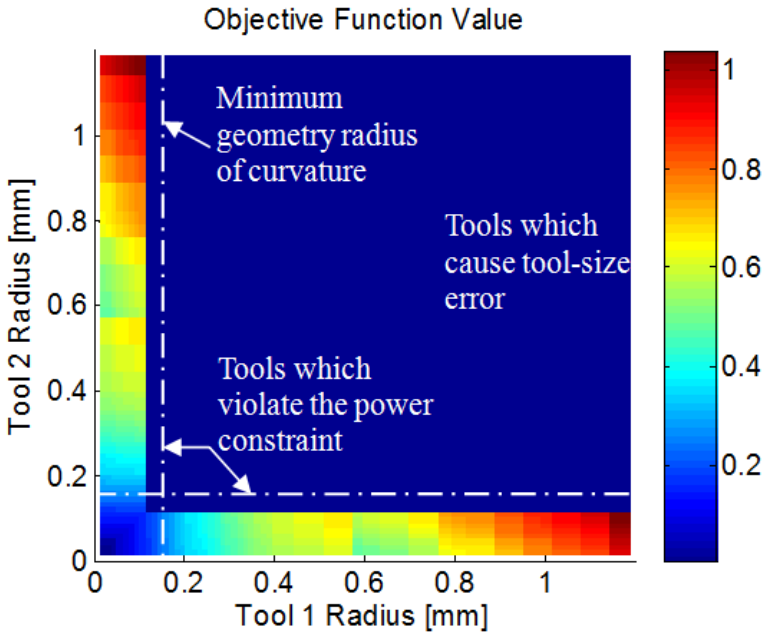

Figure 6.7: Pareto surface for case 3 in the evaluation of the tool size optimization scheme for minimal machining time and minimal dynamic effects

The Pareto surface as shown in Figure 6.7 not only indicates the optimal tool size combination as the maximum point, but also reveals the tool size combinations which cannot satisfy constraints. Dark blue regions of the Pareto surface, which represent an objective function value of zero indicate tool combinations that violate constraints. The dark blue regions corresponding to tools that are larger than the minimum feature size, found in the upper right-hand regions of the Pareto surface plot, represent tool combinations that have failed the zero tool-size error constraint. Other blue regions indicate tool size combinations for which the power constraint is violated.

The corresponding feedrate and spindle speed profiles for the optimal tools are shown in Figure 6.8. Curve segments in which the roughing tool should be used are shown shaded in gray. These regions were determined by identifying the points at which the

roughing and finishing tool feedrate curves cross. All other segments should be cut with the finishing tool.

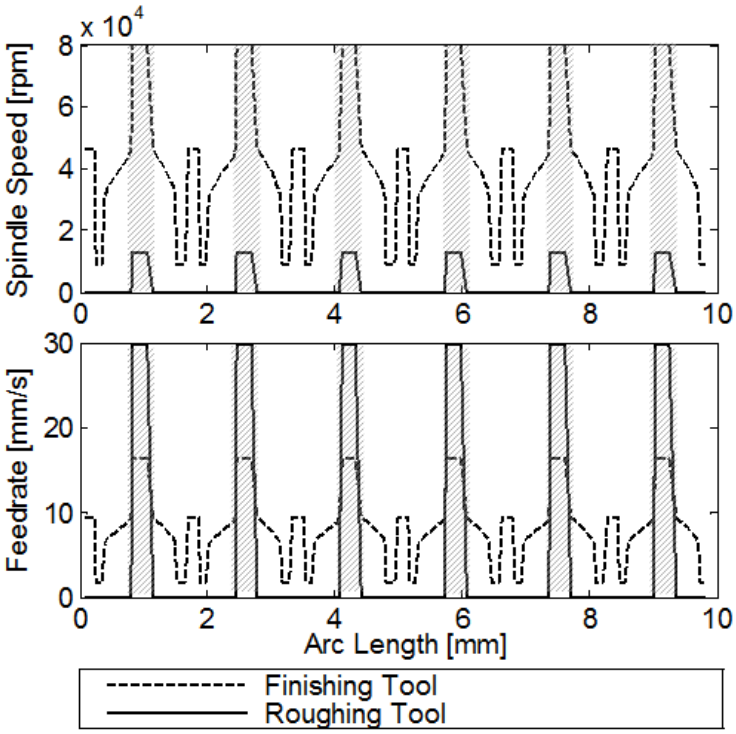

Figure 6.8: Spindle speed and feedrate profiles for the roughing and finishing tools for case 3 in the evaluation of the tool size optimization scheme for minimal machining time and minimal dynamic effects

Summary

In this chapter, two independent tool size optimization schemes were derived. The first optimization strategy considers the case in which nonzero tool size error is permissible, and so allows a greater range of tools to be considered in the optimization. However, it does not take into account spindle power limitations, or other dynamic effects. The second optimization strategy considers the case in which tool size error is constrained to be zero. This strategy accounts for dynamic effects, particularly spindle power limitations encountered when machining with a constant chipload. One of the benefits of

the second optimization scheme is that it has a modular nature, and thereby facilitates adaptation to include the specific constraints of unique applications.

Microscale segmentation and trajectory generation methods for maximum feedrate assume that a tool size has been chosen and end with determination of sampling rate. The tool size optimization methods presented here assume that segmentation has already been completed so that sampling rate is known, and ends with determination of tool size. Both aspects of the optimization are necessary to achieve an optimal operation in terms of maximal productivity.

Chapter 7: Conclusions and Future Work

The body of research presented in this thesis has addressed the enhancement of productivity in micromilling operations while maintaining the high level of precision required at the microscale. Specifically, this work has studied the impact of scale effects on the trajectory generation and feedrate optimization techniques applied at the microscale. At the start of this work, four specific objectives were established as the guide to the intended aim of the work. In this chapter, specific conclusions will be specified from the completed work, organized according to the specific objective which was addressed. The conclusions will be followed by an examination of possible avenues of future work, organized by key research topic.

7.1 Conclusions

Objective 1: To attain new knowledge which promotes increased understanding of key considerations for process optimization in high-speed, high-precision micromilling

- The traditional definition of the term 'feature size' was found to be an insufficient descriptor for application to the microscale. A modified definition as the tool-side radius of curvature was shown to adequately account for tool size effects present at the microscale.
- Three specific scale effects have been identified: the increase of the tool size to feature size ratio, the increased importance of sampling rate, and the increase of the derivative of radius of curvature with arc length.

- The increase of the ratio of tool size to feature size at the microscale has been found to cause the maximum feedrate for limited chord error to converge with the minimum feedrate according to the minimum chip thickness, resulting in cases in which the traditional method of feedrate optimization demands operation in a region of cutting instability.
- Sampling rate was found to have increased significance at the microscale, where maximum feedrate for constrained chord error becomes small. The sampling rate was shown to depend primarily on the restrictions imposed by the trajectory generation time determined by interpolation method.
- Reduction in scale of the part size was shown to cause the derivative of radius of curvature with arc length to become large at the microscale, causing the traditional feedrate optimization method of variable-feedrate NURBS to fail to constrain chord error.
- The scale effects were determined to affect microscale process optimization by causing inaccuracy in chord error calculation when the traditional method of Variable-Feedrate NURBS feedrate optimization is applied to the microscale.

Objective 2: To utilize new knowledge to develop new methods which can be applied to improve process optimization in high-speed, high-precision micromilling

- Two methods of tool size optimization were introduced to minimize cutting time with constrained geometric error through simultaneous optimization of tool size and feedrate. The new optimization methods more accurately apply to the microscale by considering the size effect of specific cutting energy of the material and limitations on spindle power. It was found that the optimal tool size is not always the largest tool which fits in a feature, as is commonly assumed.

Objective 3: To apply knowledge of scale effects in micromilling to develop a trajectory generation scheme which enhances productivity

- The EVF-NURBS feedrate optimization method was created to compensate for the inaccuracy in the traditional VF-NURBS method which occurs due to the increased $\partial p/\partial s$ scale effect. The EVF-NURBS method is shown to provide as much as 53% error reduction relative to the traditional method. The improvement is particularly significant with current PC-based control technology.
- Intelligent segmentation was shown to be an effective means of compensating for the increased Λ by capitalizing on the importance of sampling rate.
- The method of curvature-based segmentation was introduced to minimize total error by striking a balance between interpolation error and chord error. This is achieved by circular-interpolating toolpath segments with near-zero derivative of curvature and NURBS-interpolating the rest. The resulting increase in sampling time shows a reduction in cutting time of up to 15% in numerical simulations.
- The method of stability-based segmentation was introduced to improve cutting stability by circular-interpolating regions of the toolpath with high curvature. In numerical simulations, this method has shown as much as 38% reduction in cutting time.
- Application of the two intelligent segmentation methods together have been shown to provide more than 55% reduction in cutting time in numerical simulations.

Objective 4: To implement optimal parameters in a manner which is mechanically stable and robust, cost-effective, and industry-feasible

- The EVF-NURBS method was verified, showing its ability to effectively constrain error to within the specified algorithm error limit for the sinusoidal geometries
- The intelligent segmentation methods introduced in this study were experimentally validated by application to a set of sinusoidal geometries. The segmentation methods together were shown to provide as much as 36% time reduction while effectively constraining chord error to within the specified limit.
- The experimental validation showed that an increased Λ leads generally to increased benefit from the intelligent segmentation method.
- The intelligent segmentation method was experimentally validated by application to a fan shape and an airfoil shape, showing 54% time improvement for the fan and 16% time improvement for the airfoil.

7.2 Key Contributions

The work presented in this thesis has resulted in the following three key contributions:

- The identification of scale effects which impact microscale process planning

In order to improve the micromilling process, it is necessary to thoroughly expose the fundamental science which governs the process and defines limitations. This study has uncovered a series of previously unrecognized scale effects which were shown to reveal the source of limitations on achievable precision and speed in micromilling. This enhanced understanding of the micromilling process can be applied in the development of techniques for process improvement.

- The formulation of the EVF-NURBS method for improved precision

The scale effects identified in this study have revealed a source of significant inaccuracy when the customary productivity enhancement method of VF-NURBS is applied to microscale processes. In light of this finding, the method of Enhanced VF-NURBS was formulated to compensate for the scale effects. In the numerical evaluation performed in this study, the new EVF-NURBS method was shown to be capable of as much as 53% reduction in error relative to the standard method of VF-NURBS.

- Formulation of the VFIS trajectory generation method to achieve simultaneous high-speed and high-precision

The Variable-Feedrate Intelligent Segmentation method was created to overcome the limitations in productivity due to the precision and feedrate limitations imposed by the scale effects in micromachining processes. This method simultaneously achieves high-speed and high-precision by intelligently segmenting the target curve according to local curve characteristics. In experimental evaluations performed in this study, the new VFIS method has shown cutting time reductions of as much as 50%, with no increase of error relative to the standard VF-NURBS method.

These contributions have been disseminated to the community as the following publications.

Published:

Mayor, J.R. and Sodemann, A.A., (2007) “An Investigation of Scale Effects on Process Planning for High-Speed High-Precision Micromilling Operations.” *Proceedings of the International Conference on Micro Manufacturing, ICOMM 2007*

Mayor, J.R. and Sodemann, A.A. (2008) “Investigation of optimal parameter space for high-speed, high-precision micromilling.” Proceedings of the 16th International Conference on Manufacturing Science and Engineering: MSEC 2008, October 7-10, 2008, Evanston, Illinois, USA MSEC_ICMP 2008-72262

Mayor, J.R. and Sodemann, A.A., (2008). “Curvature-Based Tool-Path Segmentation for Feedrate Optimization in Micromilling.” *Transactions of the North American Manufacturing Research Institution of SME,* Vol. 36, pp. 285-292

Mayor, J.R. and Sodemann, A.A., (2008). “Intelligent Tool-Path Segmentation for Improved Stability and Reduced Machining Time in Micromilling.” *Journal of Manufacturing Science and Engineering,* Vol. 130, No. 3, pp. 031121-031134

Sodemann, A.A. and Mayor, J.R., (2009). “Parametric Investigation of Precision in Tool-Workpiece Conductivity Touch-Off Method in Micromilling.” *Transactions of the North American Manufacturing Research Institution of SME,* Vol. 37, pp. 565-572

Submitted:

Sodemann, A.A. and Mayor, J.R., “Enhanced Variable-Feedrate NURBS Trajectory Generation Method for Micromilling Processes.” Submitted to the *Journal of Manufacturing Science and Engineering* Submission no. MANU-09-1322

Sodemann, A.A. and Mayor, J.R., “Experimental Evaluation of the Variable-Feedrate Intelligent Segmentation Trajectory Generation Method.” Submitted to the *Journal of Manufacturing Science and Engineering* Submission no. MANU-09-1323

An industry contribution has also come out of this work in the application mechatronic principles to the enhancement of precision of a low-cost micromilling machine. A widely available micromilling machine which achieves a low cost/precision ratio is necessary for the further advancement of the science by increasing accessibility of micromilling technology. This work, presented in the Appendix, has resulted in the following conclusions:

- A custom micro-mesoscale machine tool was built to achieve a low cost/precision ratio.

- A method for on-part backlash measurement was introduced to allow backlash calibration with a widely-available optical microscope without requiring a dedicated laser interferometer.
- A method of velocity-based backlash compensation was introduced to improve the precision of the low-cost machine while allowing for custom contouring method which are necessary to compensate for scale effects. The backlash compensation was shown to be accurate to ± 1 *μm*.
- The conductive tool touch-off method was introduced as a low-cost and high-precision means of tool registration. This method was shown to be accurate to within 1 *μm* under the specific case of the spindle on.
- Precision tests of the machine show on-part positioning precision of ±1 *μm*.

The industry contributions from this work have been disseminated to the community as the following publications.

Published:

Mayor, J.R. and Sodemann, A.A., (2009) "Investigation of the Parameter Space for Enhanced Too Life in High Aspect-Ratio Full-Slotting Micromilling of Copper." *Proceedings of the International Conference on Micro Manufacturing, ICOMM 2009*, pp. 313-316

Submitted:

Mayor, J.R. and Sodemann, A.A., "Mechatronic Enhancements of a Low-Cost Micro-Mesoscale Machining Center." Submitted to the Journal of Materials Processing

7.3 Future Work

During the course of this study, a number of avenues of possible additional study have been identified. This section will present a selection of these future work topics for expansion of this study. Topics are organized by main research efforts.

7.3.1 Scale Effects and Process Optimization

- Tool Change Time and Wear Rate

In Chapter 2, it was determined that scale effects reveal the interdependency of tool size optimization and feedrate optimization. A scheme was devised in Chapter 6 in which feedrate and tool size optimizations are carried out simultaneously. However, the optimization work as presented in Chapter 6 considers only cutting time as the objective for minimization, and does not consider any other time costs such as tool change time. The optimization has been restricted to allow for only 2 tools in order to constrain the impact of not considering tool change time. If the optimization scheme was modified to account for tool change time, then it could also be expanded to allow for any number of tools. The optimization as presented also does not consider tool wear rates or differing cost of tools of different sizes. The second optimization scheme as developed in Chapter 6 is of a modular nature, with individual terms of the objective function devoted to individual optimization considerations. This work has the potential to be expanded to account for these or any number of additional considerations as necessary. Further study is necessary to explore this possibility.

- Optimization Equations Method of Solution

The current method used to solve the optimization equations presented in Chapter 6 is a numerical method which is computationally intensive. Such a method of solution is not detrimental currently, since the number of optimization variables is small and the optimization is carried out once, off-line. However, if additional constraints are added as per the suggestions above, and the computational intensity becomes significant, it would be beneficial to investigate other methods to solve the equations analytically, such as by the method of Lagrange multipliers. One drawback of an analytical solution is that at least one optimization variable, tool size, is a discrete variable. It is highly desirable to find the optimal tool size as one that is already commercially available, rather than a custom size. More study is required to overcome these obstacles.

7.3.2 EVF-NURBS Trajectory Generation Method

- Constant Curvature Estimation Method

In Chapter 3, an inaccuracy in conventional VF-NURBS in which the assumption of constant curvature between two subsequent sampling points breaks down at the microscale is revealed and investigated. Application to the microscale of this macroscale assumption leads to increased error due to poor estimation of radius of curvature. In Chapter 3, an estimation of curvature between two points is proposed by calculating the mean curvature. Numerical tests have shown this method to significantly improve error, but not to reduce the error to zero. To achieve the highest precision possible, other methods of estimating curvature should be investigated. One possible alternative is a midpoint method which takes the approximate radius of curvature as the circular interpolation between the first point, last point, and the data point which lies nearest the midpoint between the first and last points. Alternatively, more study is

needed to determine if there are other methods of chord error calculation which do not rely upon the constant-curvature assumption.

- Inflection Points

The method of constant curvature approximation by calculating the mean fails especially in the case of encountering an inflection point, in which the sign of curvature is reversed. Currently, this inaccuracy is compensated simply by identifying an inflection point and imposing a low feedrate in this section of the curve. Such a solution unnecessarily decreases feedrate in these sections, decreasing productivity. Additional study is needed to determine methods of compensating for this inaccuracy which do not unnecessarily reduce feedrate or cause additional error.

7.3.3 VFIS Method of Feedrate Optimization

- Point Density

The success of the CB algorithm and the SB algorithm both have been seen to depend upon the point density of the part. In the example geometries which were presented in Chapter 5, the fan trial shape had a low point density, and the airfoil shape had a high point density. In the experimental validation of cutting these shapes, it was found that the point density of the fan was insufficient to apply VFIS. The point density had first to be increased by NURBS-interpolating the shape and generating an increased point density from the interpolation. It was pragmatically determined that a point density in which points are spaced apart a few microns worked well. More study is required to determine the ideal point density.

- β Parameter Optimization

The β parameter was introduced in Chapter 5, and it was shown that a minimum value for this parameter along the entire curve can be derived analytically. More study is needed to determine if an optimal value for β can be found. Since β is a trade-off parameter between interpolation error and chord error for circular-interpolated segments, the optimal β value for one segment may not be the same as the optimal β for another segment.

7.3.4 Mechatronics-Enhanced Low-Cost High-Precision Micro-Mesoscale Machining Center

- Conductive Tool Registration

The second mechatronic enhancement for precision presented in the appendix is the conductive method of tool registration. In this study, it was determined that the case of spindle on was the most important for accurate touch-off. In the experiment that was performed, the only spindle conditions tested were spindle on and spindle off. A test should be done in which different spindle speeds are tested to determine the actual relationship between registration accuracy and spindle speed. It is predicted that this study would reveal interdependencies between approach feedrate and spindle speed that were not revealed in the tests from the appendix because of the limited spindle conditions tested. It may be that such a test would also reveal the source of the relatively high error percentage in the analysis of variance presented in this study.

- Volumetric Error Compensation

The software written for the low-cost machine only includes compensation for backlash error. Other sources of error, such as volumetric error, could also be compensated with the software. For this task, an error mapping should be made for straightness, roll, pitch, and yaw, and the error map provided to the software. The software could then compensate for this error by vector addition.

- Reduced Hardware Cost

In the low cost/precision ratio machine setup, a significant source of cost is the motors and the drives. One reason for the high cost of the drives is the capability of the drives to provide control of the motors. However, in this study, control is provided by an external source. Further study is needed to examine other actuation possibilities which may allow for an improved cost/precision ratio. The primary design constraints on choice of actuator are high torque capabilities and low inertia to allow for high accelerations, and rotational velocity to allow high feedrates. Given an external source of control, it may be possible to satisfy these constraints at a lower cost with DC motors.

- Low-Cost Real-Time Control Implementation

The low-cost high-precision machine could benefit greatly from implementation of a real-time control system. However, such a real-time platform is expensive and will negatively affect the cost/precision ratio of the machine. To compensate for this, it may be possible to control the machine with a simpler control mechanism with computing and timing capabilities, such as a PIC chip or Basic Stamp. Such an implementation would require the revision of the control software to implement some of the capabilities currently provided by the National Instruments hardware, such as PID motor control and

commutation. It would also be necessary to create a method of user interface with the chip.

Appendix: Mechatronic Enhancements of a Low-Cost Micro-Mesoscale Machining Center

Continued advancement of micromilling technology requires a wide base of access to the technology. This access can only be achieved with the availability of affordable machines capable of high-precision operations. Currently, the development of such a machine is impeded due to the prohibitive cost of high-precision hardware such as precision ball-screw motion stages, linear motor actuators, and precision sensors. Reduction in the cost of a micromilling machine requires use of low-cost, low-precision hardware. This part of the study will examine whether mechatronic enhancements of a low-cost structure can achieve a low-cost, high-precision machine.

This chapter will describe the application of fundamental mechatronic principles towards the demonstration of a low-cost, high-precision micro-mesoscale machining center that achieves an order of magnitude reduction in the cost to precision ratio relative to current commercially available machines. These mechatronic enhancements include both hardware and software components. This effort was undertaken with dual objectives: (1) as an indication of feasibility of a low cost/precision ratio machine by the use of mechatronics, and (2) to serve as a testbed for experimental validation of the methods developed in Chapters 3 and 4. This chapter will begin by describing the hardware components of the testbed. This will be followed by an overview of the control software created for the machine. Two specific precision enhancements: velocity-based backlash compensation and conductive tool registration are then described. The method of tool-workpiece conductivity monitoring is proposed as an inexpensive and accurate method for microscale tool touch-off, and the precision of the method is shown to be dependent

on parameter selection. A set of touch-off conditions is suggested for touch-off precision within 1 *μm*. The proposed mechatronic enhancements are then evaluated and results from a precision test of the machine are presented. Finally, the achieved cost/precision ratio will be evaluated and compared to other machines currently commercially available.

A.1 Hardware

The structure of the testbed machine was chosen with the objective of achieving a low cost/precision ratio and providing the capabilities necessary to implement a wide range of process parameters. The target cost of the machine is <$15k and the target precision is 1μm in order to achieve an order of magnitude decrease in the cost/precision ratio relative to current commercially-available machines.

The basis of the hardware is a set of leadscrew-driven stages purchased from Sherline, Inc. These stages were chosen for the low cost and capacity for easy customization. The chosen stages also allow for large workspace dimensions to allow for the production of a wide range of workpiece dimensions. A summary of the characteristics of the stages is shown in Table A.1.

Table A.1: Characteristics of the low-cost stages utilized in the low cost/precision ratio micro-mesoscale machining center

Characteristic	Value
Approximate Backlash (quoted)	80μm-120μm
Screw pitch (quoted)	28 tpi
Screw pitch (measured)	1.000 mm/rev
X Travel	228 mm
Y Travel	127 mm
Z Travel	159 mm

In order to improve precision, maximum velocity, and maximum acceleration, the standard stepper motor actuators are replaced by brushless DC motors model IB23002 from Motion Control Group, Inc. These motors have higher torque capabilities and higher positioning resolution relative to the standard stepper motors, yet remain inexpensive relative to the linear motors common on high-end machines. Each servo motor is fit with a 5 *V*, 5000-line quadrature optical encoder. The encoders provide position feedback to the external control system. A selection of specifications for the motors and encoders is shown in Table A.2.

Table A.2: Motion Control Group brushless servo motor specifications for model IB23002

Feature	Value
Continuous Stall Torque	0.78 Nm
Peak Stall Torque	2.34 Nm
Rated Speed	5700 rpm
Rated Power	298.28 W
Motor Inertia	0.3884940 kg cm^2
Frame Size	NEMA 23
Encoder Resolution	0.05 μm

The motors are powered by brushless servo drives model BMC12L from the same company, which provide 12.5 *A* continuous current and 25 *A* peak current, and also carry out the required commutation by interfacing with a hall sensor in each motor. The drives are capable of providing closed-loop control, but for this study are used in open-loop mode, with control provided by an external system.

In order to provide the higher rotational speeds necessary to increase cutting velocity at the microscale, two high-speed spindles are chosen for this work. The first is a high-speed air turbine spindle model HTS1501S from NSK America Corp. A second NSK America electric spindle, model E800Z is also obtained as an option. A selection of quoted specifications for these spindles is included in Table A.3.

Table A.3: Characteristics for the two spindles considered for use with the low cost/precision ratio machine

Feature	Value	
	Spindle 1	Spindle 2
Type	Electric	Air
Speed Range	0-80,000 rpm	150,000 rpm
Runout (quoted)	<1μm	<1μm

The micromilling machine is controlled by a National Instruments NI 7356 6-axis motion controller. This device receives input from the encoders and produces an analog output to the drives. A selection of the device characteristics is shown in Table A.4.

Table A.4: NI 7356 motion controller specifications

Feature	Value
Form Factor	PCI
Number of Axes	6
Control Loop Rate	2 axis at 62.5 *μs*
Maximum encoder input rate	20 *MHz*
Number of Digital IO Channels	64
Number of Analog Input Channels	8

PID feedback control is supplied by NI Motion software. This system has the capability to control motion in either position or velocity mode. The ability of the controller to operate in velocity mode is necessary to implement the custom contouring required to validate the new trajectory generation methods developed in this study. The motion control card receives input from a user-designed program written in the LabWindows language, which will be described in the next section.

A.2 Software

A program was written in the LabWindows programming language to provide high-level machine tool control. The program allows for simple control operations such as absolute

positioning and jog, as well as complex control operations such as NURBS interpolation of a user-specified toolpath. A user interface was created to allow easy access to the software machine tool control capabilities. Figure A.1 is a screenshot of the manual control component of the user interface which allows for absolute and relative positioning and jog. Software control of spindle speed has also been incorporated for use with a variable-speed electric spindle.

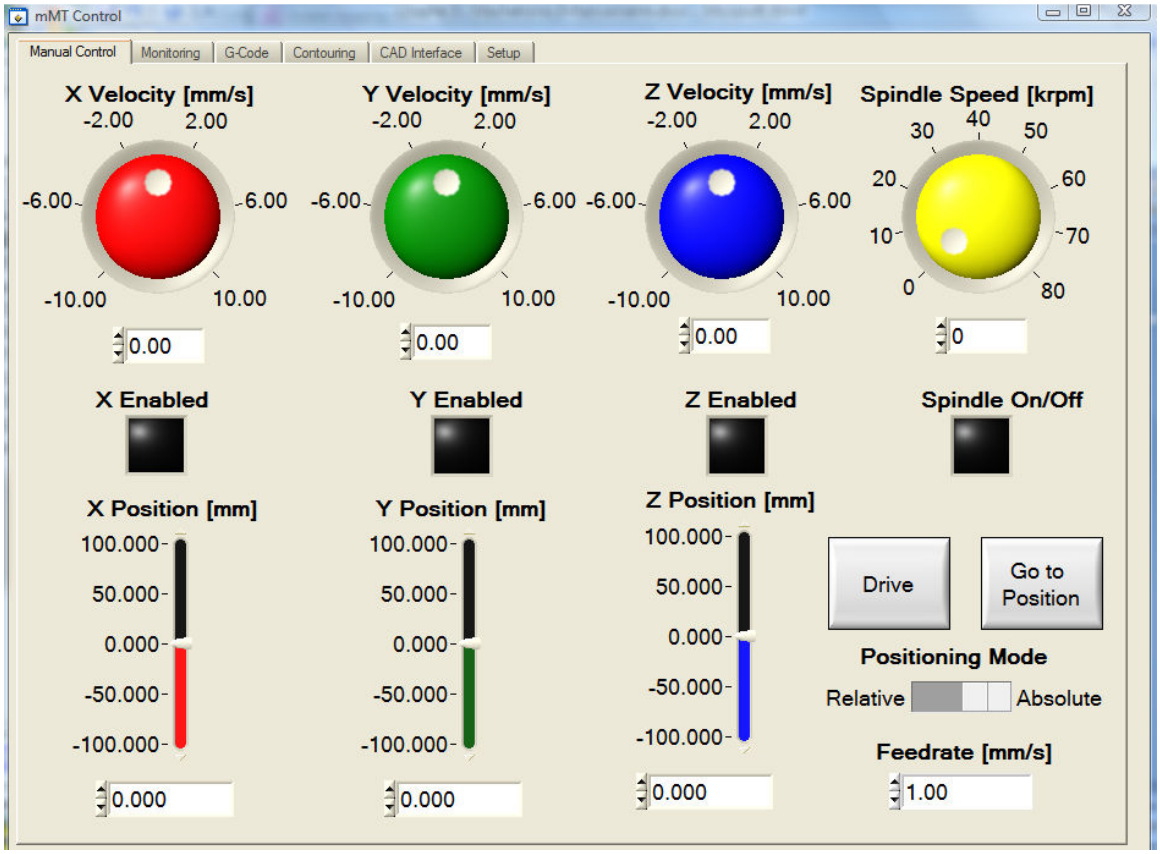

Figure A.1: Screenshot of the user interface for accessing the manual control capabilities of the control software written for the low cost/precision ratio micro-mesoscale machining center

More advanced software capabilities are accessed through the contouring component of the user interface, shown in Figure A.2.

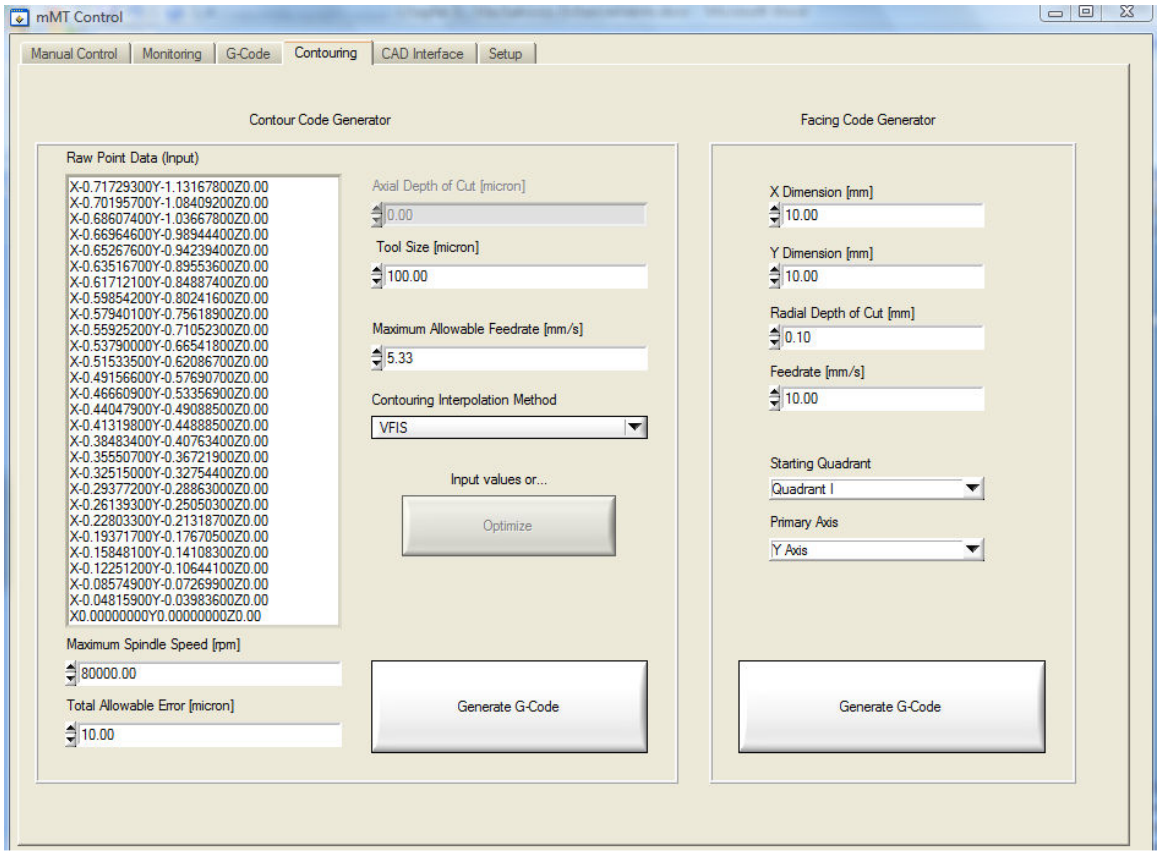

Figure A.2: User interface for accessing the custom contouring capabilities of the micro-mesoscale machining center

In the contouring component, the user is able to enter a vector of (X,Y,Z) position data points representing a target toolpath. The user also enters the maximum speed of the spindle for the target machine, the error tolerance for the finished part, and the tool size. The software then suggests a maximum allowable feedrate which provides a chipload equal to 2% of the tool diameter according to the tool size and spindle speed values entered. The user then chooses a contouring interpolation method from linear, EVF-NURBS, or VFIS options. When the 'Generate G-Code' button is clicked, the chosen interpolation method is applied to the specified data points and corresponding G-Code is exported to the G-Code component of the user interface, shown in Figure A.3.

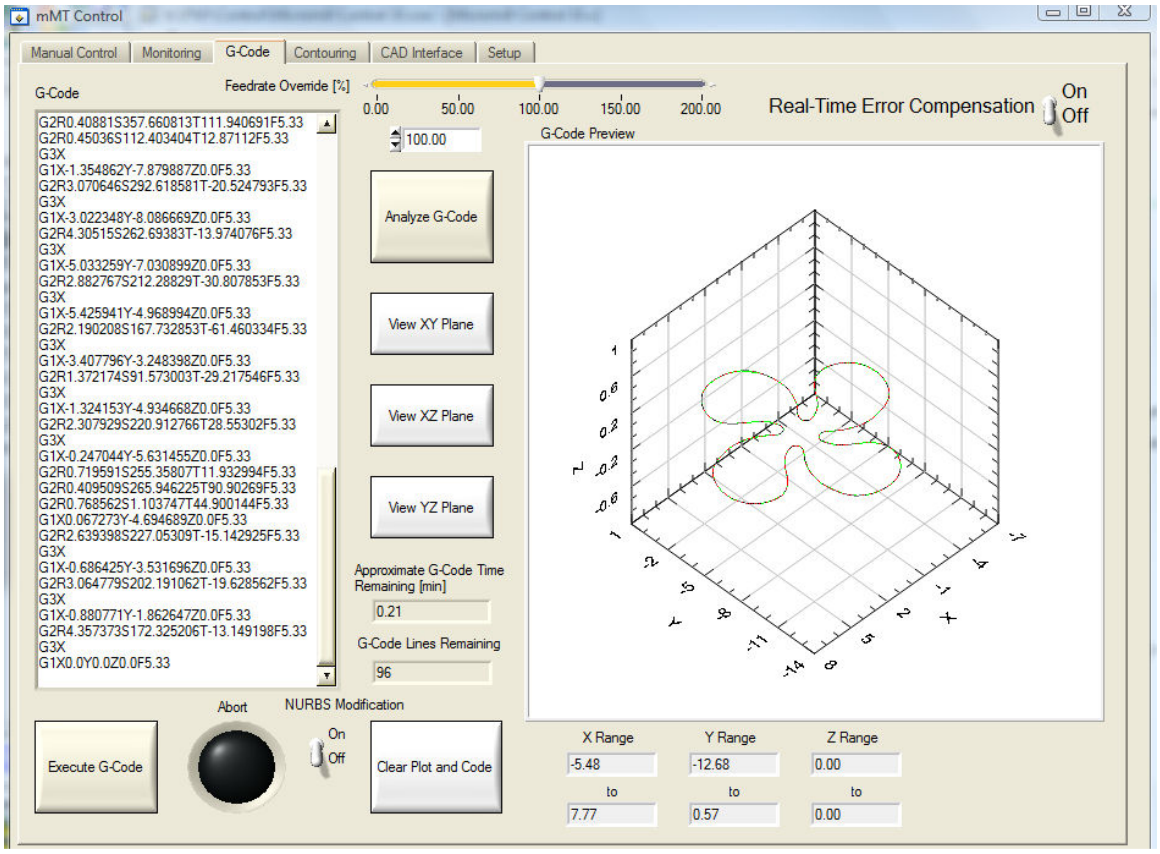

Figure A.3: User interface for accessing standard and custom G-Code emulation, analysis, and execution capabilities of the control software

G-Code is shown in the text box in the G-Code component of the user interface. The software has been given the capability to interpret standard linear and circular G-Code commands represented by G1 and G2, as well as a custom NURBS G-Code command represented by G3X. The identifying data corresponding to each G3X command is stored internally, and accessed at run-time. The G-Code appearing in this window can be previewed in the provided plot to verify the accuracy. When the 'Analyze G-Code' button is clicked, the interpolated path is plotted in green and the exact toolpath from the specified data points is plotted in red, so that the amount of interpolation and chord error can be visually evaluated prior to the cut. If the preview is correct, clicking the 'Execute G-Code' button initiates a timer which begins the contouring process on the machine.

In order to apply the methods developed in this study, standard contouring based only on linear and circular interpolation is not sufficient. A key capability written into the custom control software for this research, therefore, is the ability to generate trajectories for real-time contouring from custom interpolation and segmentation schemes. This capability also allows for the real-time compensation of backlash while contouring. A simplified flow-chart of the trajectory generation subroutine is provided here in Figure A.4 and will be referred to in the next section.

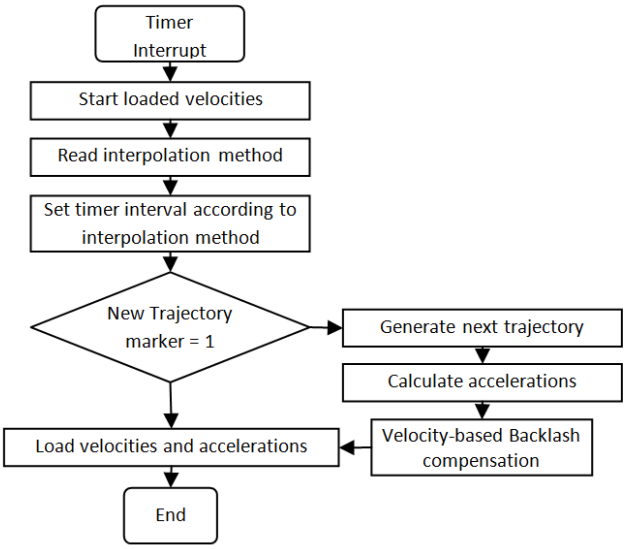

Figure A.4: Flow chart of the velocity-based trajectory generation subroutine for contouring with custom interpolation and segmentation schemes

In order to enhance the accuracy of the machine which is limited by the low-cost hardware, two key mechatronic enhancements are made: velocity-based backlash compensation and conductive tool registration.

A.3 Velocity-Based Backlash Compensation

The machine stages are quoted to have an expected backlash amount that is an order of magnitude larger than acceptable error for the machine. Therefore, a method of backlash compensation is necessary to maintain precision. The first step of backlash compensation is to measure the actual amount of backlash in the machine. A typical method of backlash measurement is the use of a laser interferometer. However, a laser interferometer is a costly piece of equipment that may not be available in many laboratories or machine shops. In keeping with the goal of increasing accessibility to micromilling technology, in this study a backlash measurement method is introduced which requires only a microscope, a piece of equipment which is likely to be available in any establishment having the intent to produce microscale components.

Backlash was measured by cutting an artifact into a piece of Al 6061, imaging the calibration shape with a Leica microscope, then measuring key features in the artifact. To plan an appropriate artifact which can be measured within the field of view of the microscope, a diagram is drawn in which the interferometer field of view is represented as a rectangle.

The artifact was cut with a 0.0040” (101.6 *μm*) diameter tool. The artifact is designed so that each of the measurement quantities can be measured sequentially, decoupling possible errors due to errors in tool size, runout, and cutting instability. A diagram of the artifact is shown in Figure A.5.

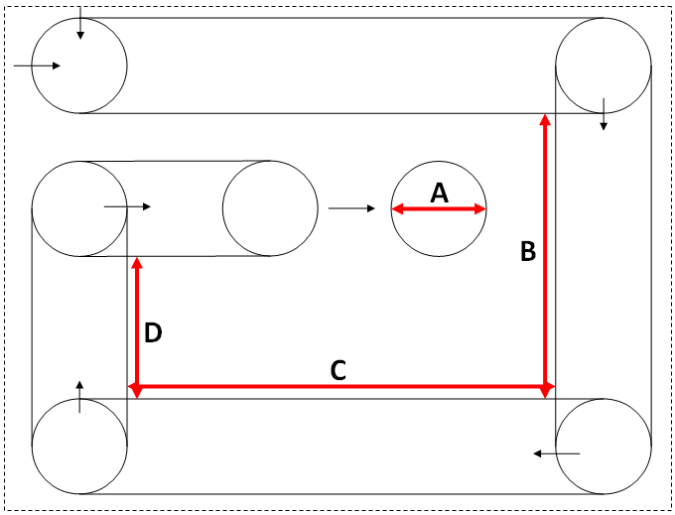

Figure A.5: Tool path of the calibration shape used to measure backlash amount decoupled from errors in tool size

The commands to create this artifact are defined by a number of encoder counts, which corresponds to a linear distance of tool travel. The target distances for the lengths identified in the artifact diagram in Figure A.5 are specified in Table A.5.

Table A.5: Target lengths of identified segments in the calibration shape

Segment	Number of Encoder Counts	Target Length [μm]
B	8000	300
C	11000	450
D	5000	150

The four distances A, B, C, and D can then be used to determine the values for X and Y backlash by application of Eqs. (1-4).

$$A = \text{Tool Diameter} + \text{errors due to runout and instability} \quad (1)$$

$$B = (\text{B Target Distance}) - A \quad (2)$$

$$C = (\text{C Target Distance}) - A - \text{X Backlash} \quad (3)$$

$$D = (\text{D Target Distance}) - A - \text{Y Backlash} \quad (4)$$

An initial set of tests are performed with no backlash compensation. The test is repeated across the X and Y axes, with 10 *mm* spacing between tests. A total of 100 *mm* of the workspace is tested in the X axis and 50 *mm* tested in Y. A characteristic image of an artifact cut with no backlash compensation is shown Figure A.6.

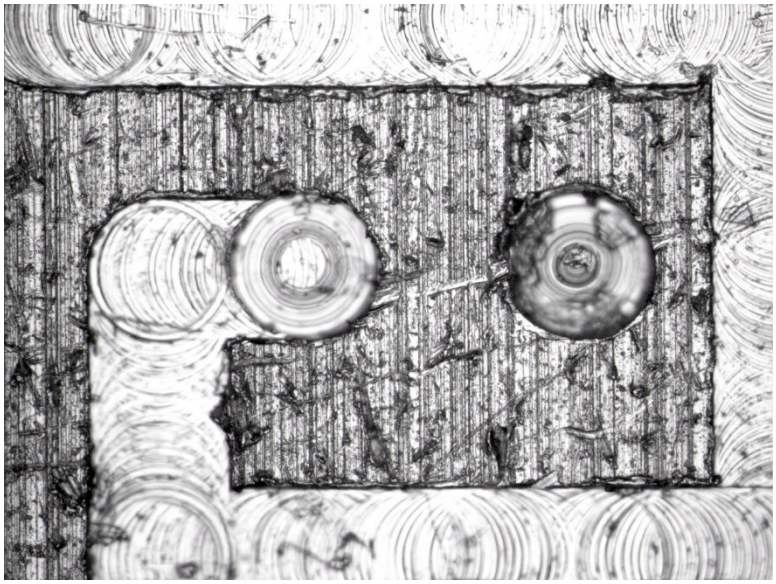

Figure A.6: Microscope image of the actual calibration shape from a characteristic backlash measurement test

Using the microscope parallel line tool, the distances across the A, B, C, and D segments in the artifact image are extracted individually. The measured values A, B, C, and D are input into Eqs. (1-4) to calculate the measured lengths for the each trial with no backlash compensation. The measured values are reported in Table A.6 and plotted in Figure A.7.

Table A.6: Backlash measurements across the X and Y stages and total backlash distribution with no backlash compensation

Axis	Position [mm]	Backlash Before Compensation [µm]	Total Backlash Distribution Before Compensation
X	0	89.41	87.61±3.76
	10	91.84	
	20	88.71	
	30	91.49	
	40	91.66	
	50	89.35	
	60	84.61	
	70	83.18	
	80	84.31	
	90	80.95	
	100	88.17	
Y	0	34.19	38.22±4.50
	10	36.14	
	20	35.03	
	30	36.05	
	40	44.02	
	50	43.90	

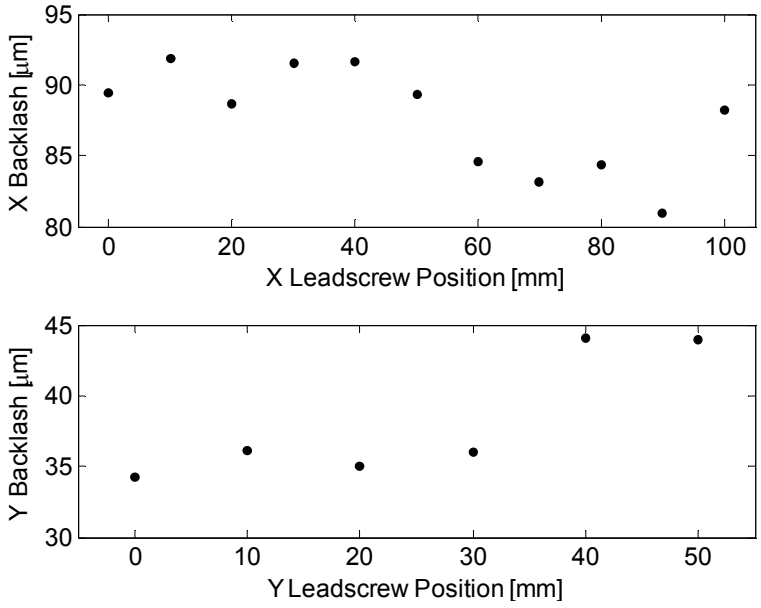

Figure A.7: Backlash measurements across the X and Y stages

Backlash compensation in position control mode is often applied in commercial motion control and CNC control applications, and this capability has also been incorporated into the custom software developed here. However, in order to compensate for backlash in velocity-based contouring for high-precision, a different method is required. In order to maintain precision and high productivity objectives, the backlash compensation method must be able to be executed in velocity control mode within a single iteration of the trajectory generation loop. The backlash compensation method must also be able to operate without causing distortion of the actual tool path. A flow chart of the backlash compensation method applied in this work is shown in Figure A.8, which represents the Velocity-Based Backlash Compensation block from Figure A.4.

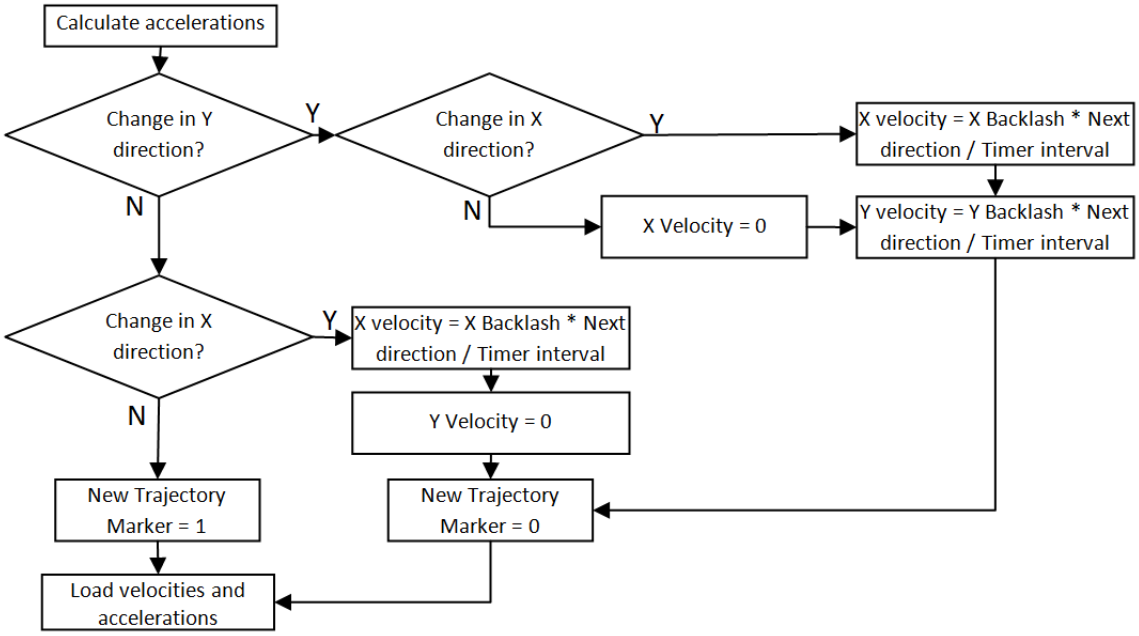

Figure A.8: Flow chart of velocity-based backlash compensation subroutine applied to the trajectory generation subroutine

A.4 Conductive Tool Registration

Tool registration is the process of locating the workpiece surface relative to the tip of the tool. Precision in tool registration at the microscale is critical because of the microendmill's extreme sensitivity to axial depth of cut [52, 53], the high relative precision required on microscale features, and difficulty in precise positioning of the workpiece. Traditional touch-off methods for the macroscale cannot be used at the microscale because of the extremely small tool size. Touch-off methods that have been proposed for use at the microscale include acoustic emissions [52, 54], optical methods such as an optical microscope with CCD camera [55], and force monitoring methods through use of a dynamometer mounted beneath the workpiece. These methods require extensive additional instrumentation and can be expensive. The conductive method of tool registration is both very inexpensive and simple to implement, requiring only a few simple electrical components. Gandarias, et al. proposed a method of tool-workpiece conductivity monitoring to detect tool breakage [56]. However, this method was not considered for registration purposes and the precision of the method not investigated. A 'conductive probe' is used by Atometric, Inc. [57], but details of the device are not provided on the website, and no patent for the device could be found.

This section will investigate the influence of various parameters on the precision of the conductivity-based touch-off method for micromilling to determine if this method is able to provide sufficiently high precision usable in microscale milling. A preliminary explanation of conductivity-based touch-off mechanics for micromilling is given as a prediction of the relationships between parameters choices and resulting high precision.

The conductivity-based touch-off circuit is designed as shown in Figure A.9. As indicated in Figure A.9, the leading resistor value is varied to test the effects of different voltages applied through the tool-workpiece interface.

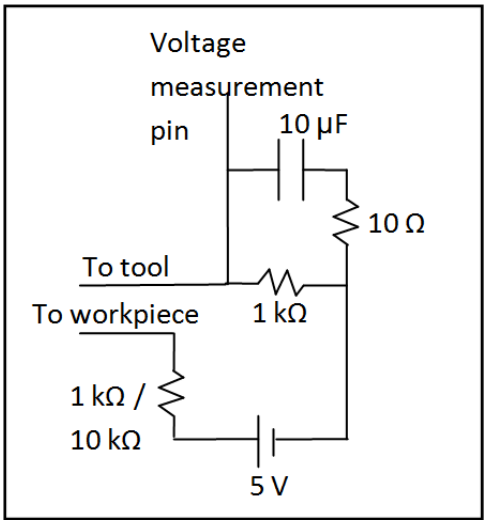

Figure A.9: Signal conditioning of the input tool/workpiece voltage included a hardware low-pass filter with 100Hz cutoff frequency

Touch-off is detected by measuring the voltage between ground and the voltage measurement pin. A voltage measurement of <0.1 V is interpreted as low voltage, and >0.1 V as high. An investigation into the mechanics of microscale conductive tool registration will now be presented.

Touch-off occurs on the bottom of the tool, which is shaped as shown in Figure A.10.

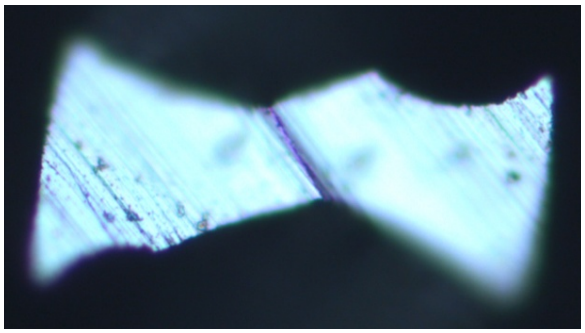

Figure A.10: Image of tool teeth from the bottom, where tool touch-off occurs

For the voltage signal to pass through the workpiece and through the tool, the tool must make electrical contact with the workpiece. Neither the bottom of the tool nor the top surface of the workpiece is perfectly flat. The geometry of the workpiece surface and endmill teeth are illustrated in Figure A.11(a), picturing the protruding edges of the tool and a rough, irregular surface on the workpiece. When the tool is not rotating, potential initial contact area between the tool and workpiece surface is small, as illustrated in Figure A.11(b).

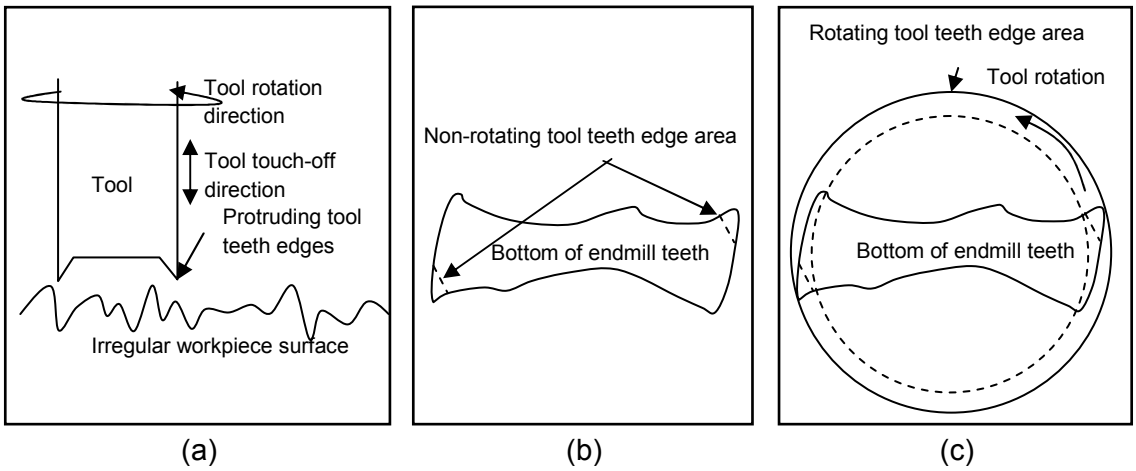

Figure A.11: (a) Tool and workpiece surface geometries (b) non-rotating tool potential initial contact area (c) rotating tool potential initial contact area

If the tool is not rotating, a voltage signal will not be seen until there is sufficient electrical contact area. As the contact area increases, resistance of the tool-workpiece interface decreases, increasing the voltage over time, as shown in Figure A.12(a). If the tool is rotating, the edges of the teeth can potentially contact the workpiece over a much larger area. The potential initial contact area for a rotating tool is shown in Figure A.11(c).

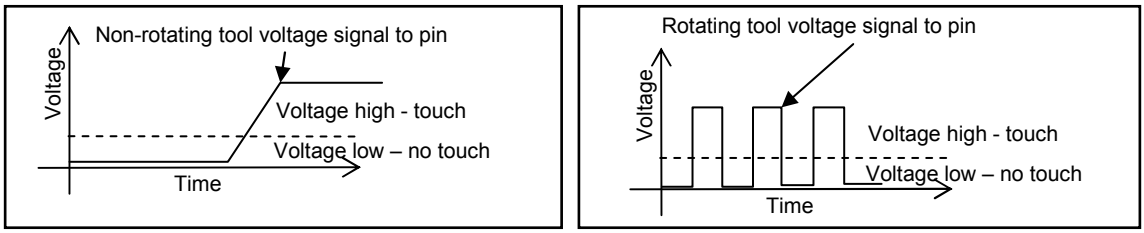

(a) (b)

Figure A.12: (a) Predicted non-rotating voltage signal during touch-off (b) predicted rotating voltage signal during touch-off

The rotating teeth will contact the surface periodically at the peaks of the workpiece surface. The voltage signal will be comprised of a series of pulses, as shown in Figure A.12(b). The high-frequency pulsed signal is perceived by the low-frequency voltage measurement device as a constant positive voltage signal. The magnitude of the perceived voltage signal increases with increased pulsing frequency. The frequency of the voltage pulses received is dependent on the rotational speed of the cutter and the number of workpiece surface peaks within the rotating tool teeth edge area. Given a constant surface roughness value, the number of workpiece surface peaks within the rotating tool teeth edge area depends on the tool size.

It is predicted that the precision of the touch-off will improve with an increase in the frequency of the pulsed signal. Such a frequency increase can be achieved by increasing spindle speed or increasing tool size. Additionally, it is predicted that touch-

off precision can be improved by increasing the magnitude of the voltage pulses by decreasing the resistance in the touch-off circuit.

In the process of the touch-off, the Z axis is indexed in the negative direction, so that the spindle is lowered towards the workpiece. If the spindle is on during the touch-off, the trajectory of the tool teeth is a helix. The helix pitch is determined by the speed of the touch-off, as shown in Figure A.13.

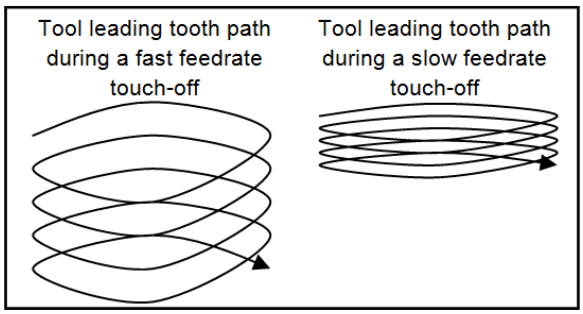

Figure A.13: Tool tooth trajectory during touch-off for fast and slow feedrates

A helix is defined as indicated in Eq. (5).

$$\begin{aligned} x(t) &= a\cos(t) \\ y(t) &= a\sin(t) \\ z(t) &= bt \end{aligned} \tag{5}$$

The pitch of the helix is defined as the distance traveled in the Z direction during one helix rotation. The pitch of the helix created by the tool tooth trajectory during touch-off is the ratio of feedrate to spindle speed, as shown in Eq. (6), where *N* is spindle speed in rpm, and *f* is the feedrate in the touch-off.

$$pitch = \frac{f}{N} \tag{6}$$

It is predicted that a slow feedrate will result in a more accurate touch-off than a high feedrate. However, at the microscale the spindle speed is relatively high compared to

the feedrate, so that the pitch remains small; in the tests performed in this study, helix pitches of 0.02 *μm* and 0.004 *μm* were studied.

A.5 Experimental Evaluation of the Machine Precision

In this section, the precision of the low cost/precision ratio machine will be evaluated. First, the two mechatronic enhancements of backlash compensation and conductive touch-off are evaluated. This will be followed by a precision evaluation of the machine.

A.5.1 Backlash Compensation Evaluation

A simple position-based backlash compensation algorithm is applied to the command of the artifact described in Figure A.5. Similar to the backlash measurement procedure, the artifact is cut 11 times over a 100 *mm* range in the X axis and 6 times over a 50 *mm* range in the Y axis. The amount of backlash compensation is set to the mean values reported in Table A.5 for the X and Y axes. A characteristic microscope image of a backlash-compensated trial is shown in Figure A.14.

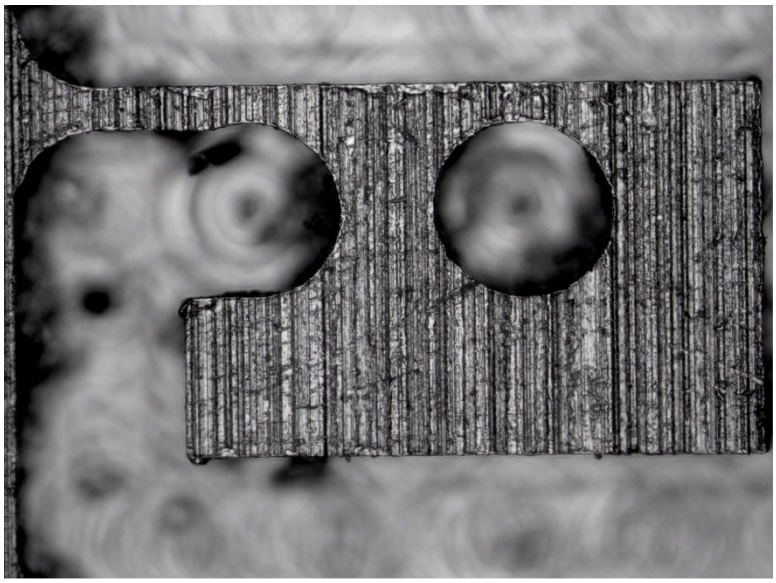

Figure A.14: Microscope image of the actual calibration shape from the backlash compensation test

Table A.7 lists the complete results from the backlash compensation tests.

Table A.7: Measured backlash values for the artifact tests cut with backlash compensation

Axis	Position [mm]	Backlash After Compensation [µm]	Total Backlash Distribution After Compensation
X	0	-2.45	-0.38±3.26
	10	1.99	
	20	2.89	
	30	3.72	
	40	4.51	
	50	0.04	
	60	-3.19	
	70	-2.95	
	80	-4.28	
	90	-0.25	
	100	-4.25	
Y	0	-7.39	1.16±6.63
	10	-4.74	
	20	2.00	
	30	0.64	
	40	10.57	
	50	5.86	

Table A.7 indicates that the mean backlash has been reduced to within ±1 *μm*, but the standard deviation remains approximately equal to the non-compensated tests. This could be improved by implementing a mapped backlash compensation scheme in which the amount of backlash compensation is targeted to the location on the leadscrew.

The velocity-based backlash compensation algorithm is tested on a sinusoidal geometry. The encoder positions are polled once in each loop of the trajectory generation subroutine. The reported positions are then compared with the target positions and reported as 'Error Plus Backlash' in Figure A.15.

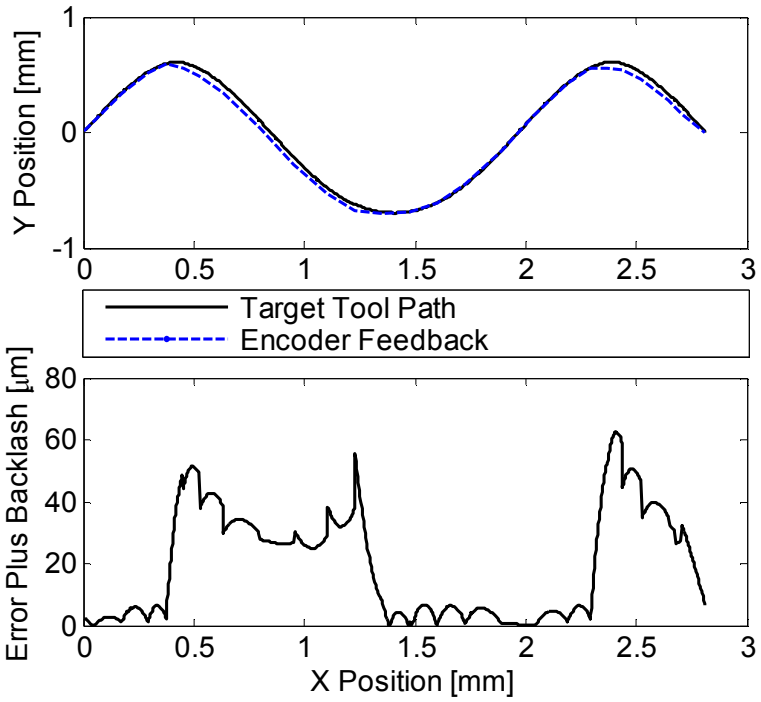

Figure A.15: Results of the velocity-based backlash compensation subroutine applied to a sinusoidal geometry

Figure A.15 shows a large increase in the difference between the target tool path and the encoder feedback at velocity reversals, indicating that the velocity-based backlash compensation algorithm is operating correctly.

A.5.2 Conductive Tool Registration Evaluation

In this study, various combinations of process variables were tested in an evaluation of the conductive touch-off method. The precision of the touch-off was measured for each variable value combination. An analysis of variance was performed to determine the magnitude of the effect of each variable.

In preparation for the touch-off tests, a copper workpiece was faced with a 2 *mm* diameter tool. The piece was faced with emphasis on providing a smooth surface finish, and later measurements showed the piece to have an average surface roughness of approximately 0.18 *μm*. The touch-off tool was then mounted and touch-off tests were performed. During each touch-off test, the Z axis was driven to position the tool tip at approximately 0.3 *mm* above the workpiece surface, so that no contact between tool and workpiece was detected. Parameters were set according to test specification, and a touch-off event was performed. Each combination of parameters was tested 5 times.

During a touch-off test, the Z axis is driven in the negative direction, thus lowering the spindle towards the prepared copper workpiece at a constant approach feedrate. The voltage at the pin is sampled at 0.1 *kHz*. When a high voltage is detected on the pin, a kill command is issued to the Z axis servo motor effecting the lowering of the spindle. For the spindle off condition tests, the spindle was turned off, the touch-off was performed, and then the spindle was turned on for a few seconds to create a

measurable indentation. For the spindle on condition tests, the spindle remained on during the entire test. The depth of the indentation produced by the tool is measured by a white-light interferometer and recorded as touch-off error.

Touch-off tests were performed with a set of variable values to determine the relative significance of the different variable values on the precision of the touch-off. The goal is to find the optimal values for an accurate and fast touch-off independent of the tool size used. A list of the parameters tested is shown in Table A.8.

Table A.8: Variables and values tested for evaluation of the conductive tool registration method

Variable	Values
Spindle speed	0, 150000 rpm
Approach feedrate	50, 10 μm/s
Voltage	0.5, 2.5 V
Tool size	0.1, 0.2, 0.6 mm

After all tests had been performed, the results were examined. Each touch-off location was scanned and the peak-to-valley measurement recorded diametrically across the touch-off location. Figure A.16 (a)-(d) illustrate the scan method for a relatively poor touch-off that was measured to be approximately 20 *μm* deep. This high-error touch-off was obtained using a 100 *μm* diameter tool with 0.5 *V* maximum signal, spindle off, at a 50 *μm/s* approach feedrate.

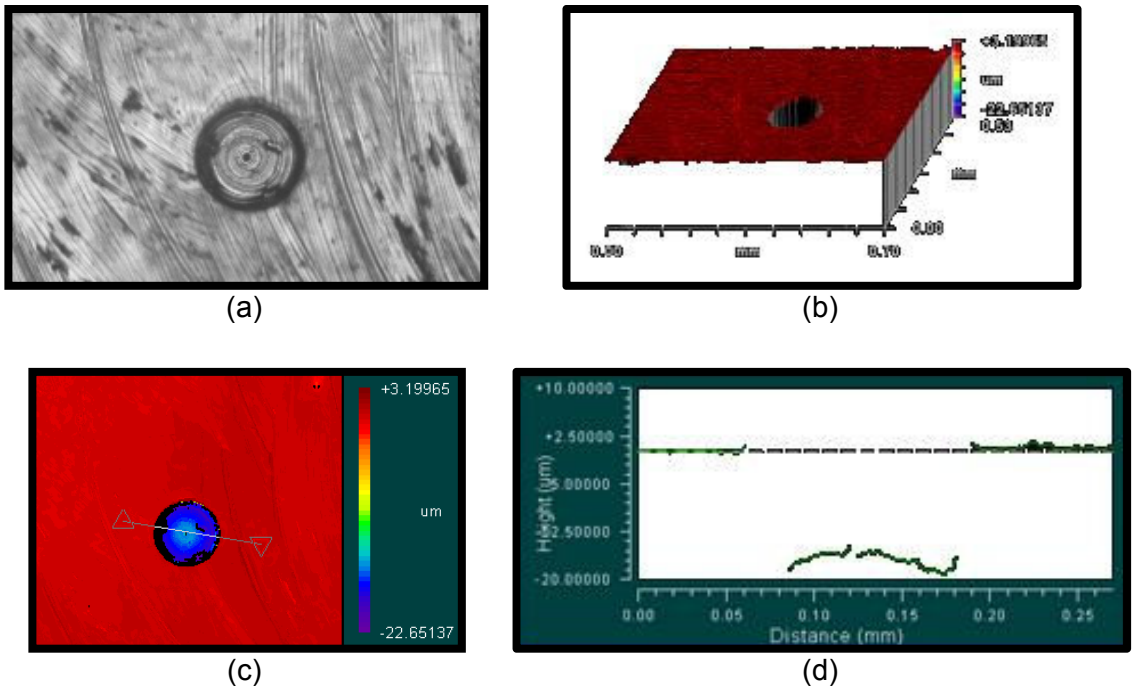

Figure A.16: Scan results for an unsuccessful conductive tool touch-off with a 100 *µm* tool, 0.5 *V*, spindle off, 50 *µm/s*

Figure A.17(a)-(d) are images the scan results for a relatively successful touch-off that was measured to be approximately 2 *µm* deep. This low-error touch-off was obtained using a 100 *µm* tool, 2.5 *V* high signal, spindle on, at a 50 *µm/s* approach feedrate.

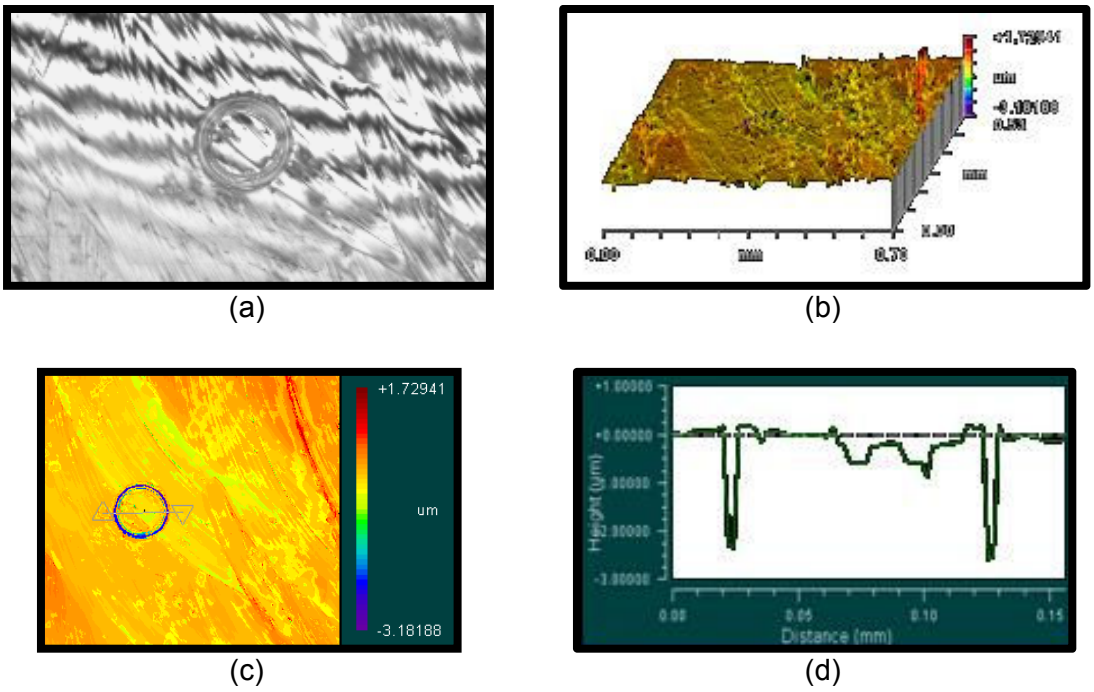

Figure A.17: Scan results for a successful conductive tool touch-off using a 100 *µm* tool, 2.5 *V*, spindle on, 50 *µm/s*

A complete list of the data collected is recorded in Table A.10. Touch-off tests that were more successful were more difficult to measure. Some of the tests performed resulted in touch-off indentations too small to be measured independent of the workpiece surface roughness. The results of these tests are recorded as in the data as 0.00 *µm* of measured error.

Table A.9: Complete touch-off error data measured for all tests of the conductive tool registration method

Parameters				Measured Error [µm]				
Tool Size [mm]	**Signal Voltage [V]**	**Spindle Condition**	**Approach Velocity [µm/s]**	**Trial 1**	**Trial 2**	**Trial 3**	**Trial 4**	**Trial 5**
0.1	**0.5**	**Off**	**50**	40.00	22.73	33.72	23.37	20.87
			10	25.27	31.40	30.29	27.93	20.13
		On	**50**	4.93	7.73	7.75	9.97	8.41
			10	3.72	4.63	3.59	2.76	0.79
	2.5	**Off**	**50**	5.44	9.96	13.75	15.75	5.31
			10	18.91	0.00	26.13	18.03	0.00
		On	**50**	0.00	6.64	0.00	4.90	0.00
			10	0.00	0.00	0.00	0.00	0.00
0.2	**0.5**	**Off**	**50**	21.10	32.87	36.59	22.31	29.89
			10	26.21	7.47	22.27	20.26	23.77
		On	**50**	11.51	8.96	8.20	10.11	12.01
			10	3.49	0.00	0.00	0.00	0.00
	2.5	**Off**	**50**	32.56	41.89	11.93	40.46	44.15
			10	45.71	38.95	19.22	44.69	0.00
		On	**50**	3.95	6.10	8.06	10.42	9.72
			10	3.94	4.03	0.00	0.00	0.00
0.6	**0.5**	**Off**	**50**	26.21	19.68	11.89	20.46	13.75
			10	9.14	20.16	9.47	24.19	22.47
		On	**50**	2.05	4.16	3.08	2.87	4.14
			10	0.00	0.78	1.02	1.71	1.71
	2.5	**Off**	**50**	24.29	22.61	10.03	11.07	13.97
			10	7.48	2.33	4.10	14.26	10.50
		On	**50**	1.43	2.56	1.83	2.14	1.35
			10	1.57	1.68	1.34	1.24	0.00

The mean and variance for each test was calculated and plotted. Figure A.18(a) and (b) show the measured touch-off error with tool size for all cases tested along with the standard deviation shown by the error bars, Figure A.19(a) and (b) illustrate the variance in touch-off error for all cases.

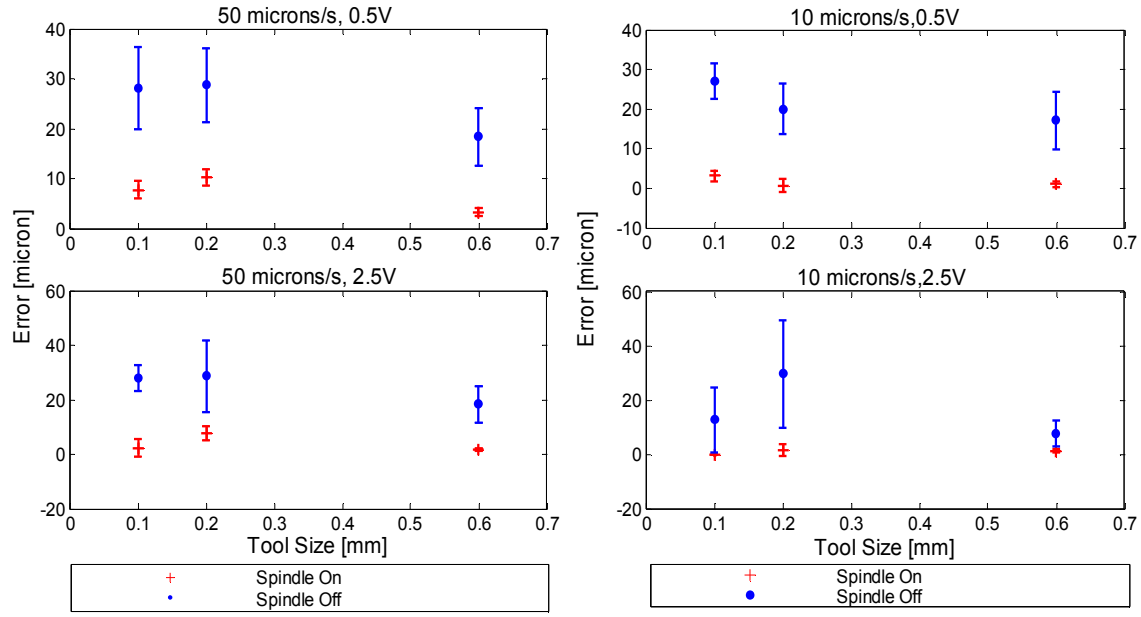

Figure A.18: Mean and standard deviation of touch-off error measured for all (a) 50 *µm/s* cases tested and (b) all 10 *µm/s* cases tested in the conductive tool registration tests

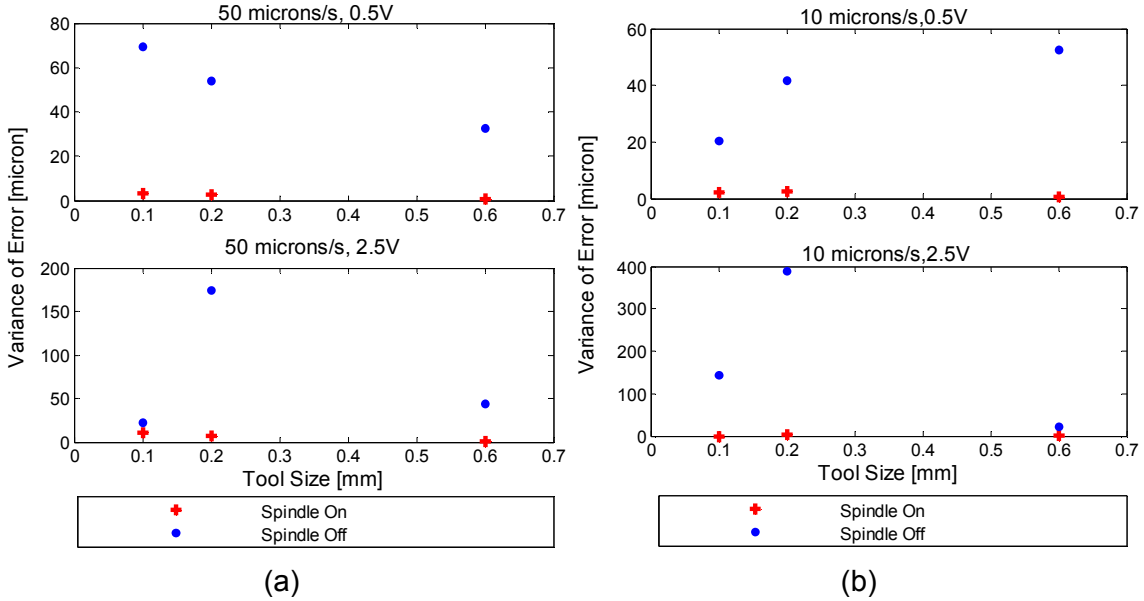

Figure A.19: Variance of touch-off error for (a) all 50 *µm/s* cases tested and (b) all 10 *µm/s* cases tested in the conductive tool registration tests

Figure A.18(a) and (b) suggest that the most significant factor for touch-off error reduction may be spindle condition. To verify this, an analysis of variance was carried out on the data. The results are shown in Table A.10.

Table A.10: Analysis of variance for various touch-off parameters

Variable	Symbol	SS	Percent
Approach Feedrate	A	463.1	2.55%
Spindle Condition	B	9139.9	50.29%
Voltage	C	334.8	1.84%
Tool Size	D	1385.9	7.63%
Feedrate & Spindle	AxB	2.8	0.02%
Feedrate & Voltage	AxC	13.0	0.07%
Feedrate & Tool Size	AxD	175.8	0.97%
Spindle & Voltage	BxC	61.8	0.34%
Spindle & Tool Size	BxD	531.8	2.93%
Voltage & Tool Size	CxD	932.3	5.13%
Spindle & Voltage & Tool size	BxCxD	536.3	2.95%
Feedrate & Spindle & Tool size	AxBxD	75.8	0.42%
Feedrate & Voltage & Tool size	AxCxD	67.8	0.37%
Feedrate & Spindle & Voltage	AxBxC	9.2	0.05%
Feedrate & Spindle & Voltage & Tool Size	AxBxCxD	41.5	0.23%
Error	E	4402.1	24.22%

The most significant variance percentages in Table A.10 are charted in Figure A.20.

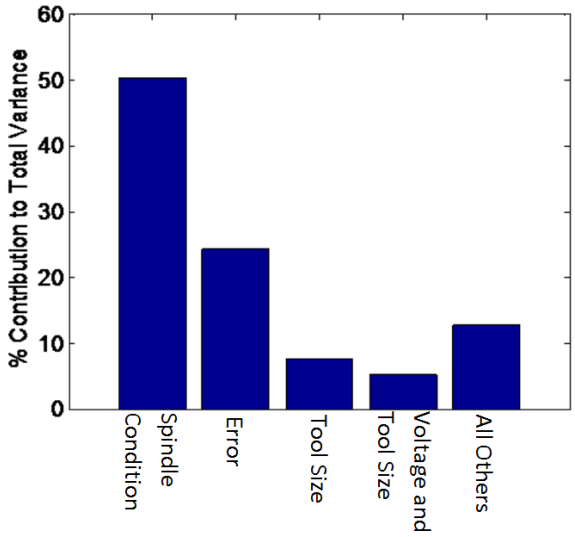

Figure A.20: Percent contribution of all tested variables to total output variance of the conductive tool registration tests

Figure A.19(a) and (b) also indicate that there is less variability in the magnitude of touch-off error for the spindle on condition. In order to investigate this, the calculated error mean and 95% confidence interval magnitudes were calculated for all cases and are listed in Table A.11.

Table A.11: Mean and 95% confidence interval magnitude for all cases tested in the conductive tool registration tests

Parameter				Calculated Values	
Tool Size [mm]	**Voltage [V]**	**Spindle Condition**	**Approach Feedrate [µm/s]**	**Error Mean [µm]**	**95% Confidence Interval Magnitude [µm]**
0.1	0.5	Off	50	28.14	7.29
			10	27.00	3.95
		On	50	7.75	1.60
			10	3.10	1.27
	2.5	Off	50	10.04	4.15
			10	12.61	10.46
		On	50	2.31	2.82
			10	0.00	0.00
0.2	0.5	Off	50	28.73	5.66
			10	20.00	6.43
		On	50	10.16	1.42
			10	0.70	1.37
	2.5	Off	50	34.20	11.56
			10	29.72	17.30
		On	50	7.65	2.33
			10	1.59	1.91
0.6	0.5	Off	50	18.40	5.01
			10	17.09	6.35
		On	50	3.26	0.79
			10	1.04	0.63
	2.5	Off	50	16.39	5.81
			10	7.73	4.22
		On	50	1.86	0.44
			10	1.17	0.59

The 95% confidence interval calculations confirm that the spindle on condition tests consistently have a smaller confidence interval. The confidence intervals for the spindle on tests are plotted in Figure A.21.

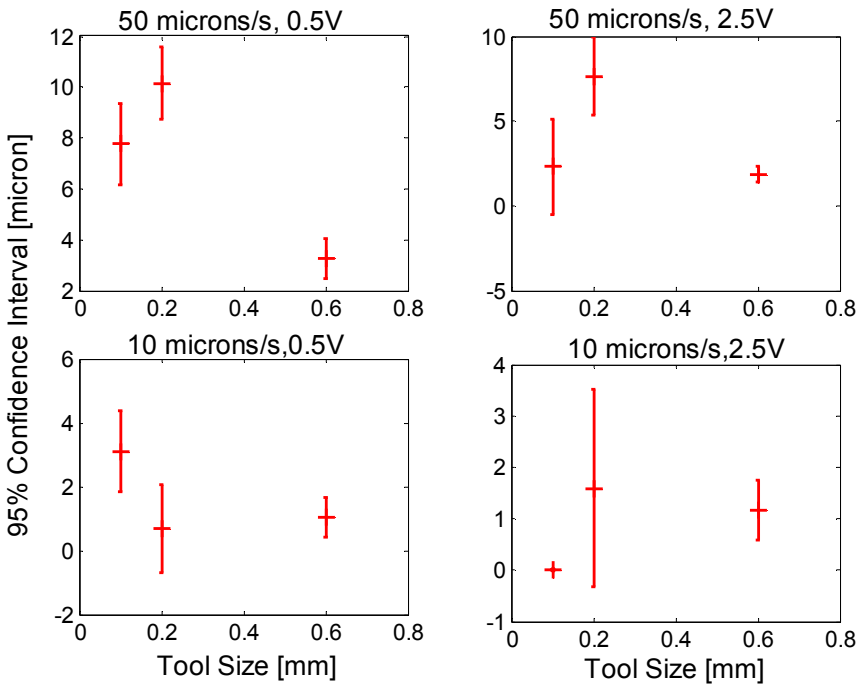

Figure A.21: 95% confidence interval of touch-off error for the spindle on cases of the conductive tool registration tests

From the results of the analysis of variance it is determined that all variables tested have an effect on resulting touch-off error, with differing magnitudes. The difference in error with voltage and approach feedrate is relatively insignificant, returning percentage of variance values a unit of magnitude smaller than the more significant variable of spindle condition, which contributes 50.29% of the total variance. Figure A.18(a) and (b) indicate that a higher voltage consistently results in less error only in the 50 *μm/s*, spindle on case. From these figures, approach feedrate is seen to have a small effect on touch-off error. In one case: spindle off, 2.5 *V*, for the 0.1 *mm* tool, the slower approach speed resulted in an increase in error compared with the faster approach feedrate. However, this difference is only a few microns.

In one case: 0.1*mm* tool, 2.5*V*, spindle on, 10 *μm/s* approach feedrate, the mean error and the 95% confidence value are both zero. In this case, the touch-off resulted in only a mark on the workpiece surface, the depth of which could not be measured independent of the workpiece surface roughness.

The analysis of variance reveals spindle speed and tool size to be the most significant variables, with spindle speed an order of magnitude more significant than the tool size. The spindle on condition results in significantly less error for all cases tested. In addition to a reduction of error, the spindle on condition results in a much smaller variance among test cases, as illustrated in Figure A.19 (a) and (b), and reduced 95% confidence interval, as shown in Table A.11.

The analysis of variance indicates that 24.22% of the variance is due to experimental error. This may be due to a number of undiscovered dependencies on untested variables such as runout, temperature variation, variability in workpiece material composition, etc. However, it is expected that this error component will diminish if a larger number of tests are performed at each parameter set. With a small number of tests performed at each parameter set, small testing anomalies cause a large amount of testing error variation. Additionally, the variance calculations presented in Figure A.19 (a) and (b) reveal that a large amount of the unexplained variation occurrs when the spindle is off. This may be due to surface roughness variations which more dramatically impact the spindle off cases. Six cases tested provided less than 1 *μm* of error within the 95% confidence interval. All of the cases are spindle on conditions. These cases are grayed in Table A.11.

A.5.3 Precision Test

After the mechatronic enhancements have been implemented and tested on the machine, a test is performed to validate the precision capabilities of the low cost/precision machine. In this test, a 200 *μm* stub-length endmill is used to cut a cross shape into a piece of Al 6061. Two shapes are cut: one with a target wall thickness of 100 *μm* and a second with a target wall thickness of 25 *μm*. Both shapes are cut to a depth of 30 *μm*.

From previous cuts made with the 200 *μm* tools, errors due to inaccurate tool size, spindle runout, and possible tool vibrations are estimated to result in a channel of around 220 *μm* from the 200 *μm* tool. Compensation for this error is programmed into the toolpath for the precision test. After the shapes are cut, they are imaged with a Leica microscope model DMRM. The actual size of the channel is measured at the start of each of the two tests. Figure A.22 shows the images of the two cut test shapes.

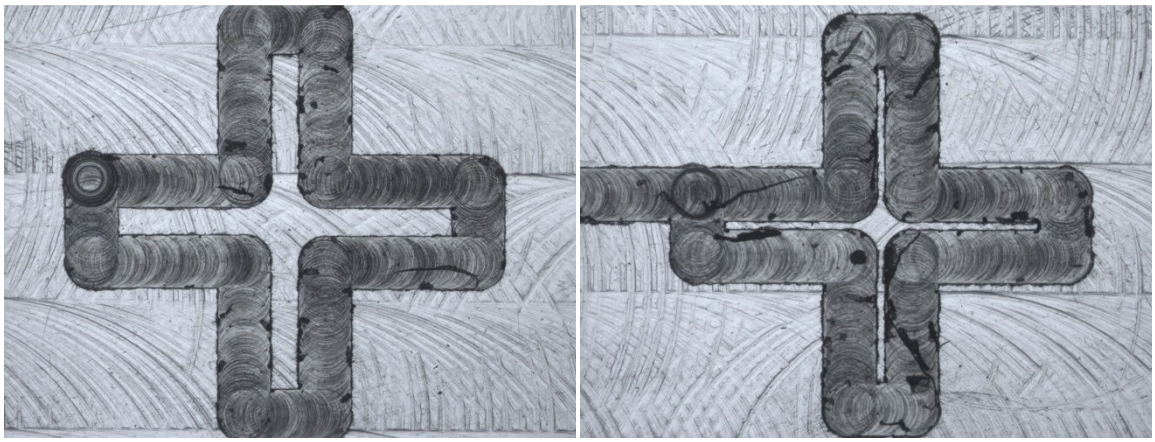

(a) (b)

Figure A.22: Images of the two cross-shaped precision tests with target wall thicknesses of (a) 100 *μm* and (b) 25 *μm*

The width of each arm is measured 5 times in random locations along the arm. The measurement is made by utilizing the parallel line measurement tool of the Leica DMRM that calculates the orthonormal distance between two superimposed parallel lines aligned at the edges of the walls. Figure A.23 shows a characteristic image of the measurements for both the 100 *μm* wall and the 25 *μm* wall.

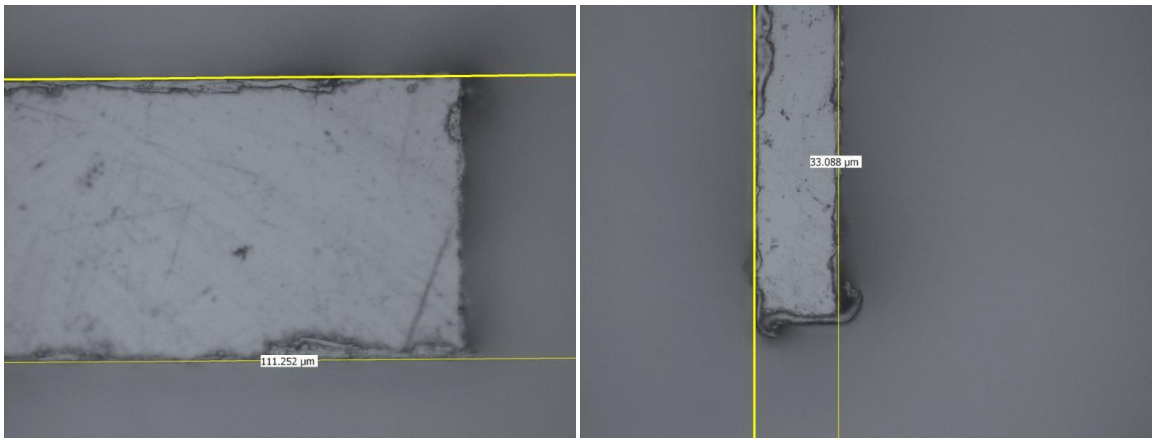

(a) (b)

Figure A 23: Example measurements of the (a) 100 *μm* wall and (b) 25 *μm* wall precision test features created with the low cost/precision ratio micro-mesoscale machining center

The error in wall thickness is calculated independent of errors due to tool size according to Eq. (7).

$$error = (Tool\ Size\ Compensation - Measured\ Tool\ Size) + (Target\ Wall\ Thickness - Measured\ Wall\ Thickness) \quad (7)$$

The mean and standard deviation of error in wall thickness is calculated for each arm. The measured results from both the 100 *μm* and 25 *μm* targets have been consolidated using standard single-variable statistical techniques and the corresponding distributions for error are reported in Table A.12. The mean measured wall thickness characterizes the normal distribution of the errors measured in each arm of the target geometry. The

artifact error distribution characterizes the distribution of measured error across all arms of the artifact.

Table A.12: Distribution of measurements of the wall thicknesses in the precision test

Target Width [µm]	Tool Size Compensation [µm]	Measured Tool Size [µm]	Measured Wall Thickness Distribution [µm]	Error Distribution [µm]	Artifact Error Distribution [µm]
100	220	210.255	108.500±0.120 109.388±0.231 110.930±0.358 108.636±0.144	1.245±0.120 0.365±0.215 1.185±0.359 1.109±0.144	0.976±0.411
25	220	211.955	31.503±0.272 31.503±0.316 31.976±0.306 32.816±0.476	1.096±0.272 1.542±0.316 1.069±0.306 0.368±0.351	1.019±0.485

The results of the precision test show the capability of the machine to produce small features to within 1 *µm*.

A.6 Cost/Precision Analysis

In this section, the final cost of the machine will be evaluated and the cost/precision ratio compared against other machines currently commercially available. A list of costs of the machine components is given in Table A.13.

Table A.13: List of component costs of the testbed machine

Item	Cost
Sherline 5400-CNC micromilling machine stages	$1005.00
MCG IB23002 brushless servos x 3	$1275.00
MCG BMC12L brushless servo drives x 3	$1776.00
NSK HTS1501S spindle	$3030.00
NI 7350 motion controller	$3099.00
Total Cost	**$10,185.00**

Table A.13 reveals that the total cost of the machine is within the target cost of <$15k. This cost can be compared against the approximate costs of commercially available

machines to evaluate the cost/precision ratio. Table A.14 lists a selection of micromilling machines that are currently commercially available, provided as a comparison with the mechatronic-enhanced low-cost machine constructed in this study.

Table A.14: Micromilling machines currently commercially available

Company	Model	Cost	Quoted Positioning Accuracy	Work Volume
Yasda	YMC325	$550,000	Sub-micron	300 x 250 x 250
Sodick	AZ150	$750,000	0.1μm	150 x 150 x 100
Atometric	G4-ULTRA	$150,000	0.6μm positioning, 2 μm along path	101 x 101 x 76
Microlution	363-S	$140,000	2μm	63 x 63 x 63
Kern	Pyramid Nano	$250,000	0.3μm	70 x 70 x 150
This Machine		$10,185	1μm (measured)	228x127x159

The machine developed in this study is approximately an order of magnitude less expensive, while maintaining approximately equivalent positioning accuracy and equivalent work volume. Some of the machines on the list in Table A.14 have a higher quoted positioning accuracy, such as the Sodick and Yasda machines, however, these machines are approaching an additional order of magnitude increase in cost. Given comparative precision capabilities, the low-cost machine created in this study shows a decrease in cost/precision ratio.

Summary

A micro-mesoscale machining center was built with the objective of achieving an improvement in cost/precision ratio over currently commercially-available machines. Custom software was developed to control low-cost hardware to provide standard machine tool control capabilities, improve precision, and allow for implementation of the segmentation methods proposed in this study. Two key mechatronic enhancements: conductive tool registration and velocity-based backlash compensation, were created and implemented.

The inexpensive conductive tool registration method was shown to provide accurate touch-off to within 1 *μm* under the specific condition of the spindle on. Tool size was also seen to be a moderately significant variable, with a larger tool providing a more accurate touch-off. As predicted, lower approach feedrate and higher voltage also resulted in a more accurate touch-off, but only marginally. By an order of magnitude, the most significant variable for accurate touch-off with the conductivity method is the spindle speed. Backlash compensation was measured using an accessible method which only requires access to a microscope. The backlash compensation was shown to be accurate to ±1 *μm*.

Precision tests of the machine with mechatronic enhancements in place have shown the machine to have a positioning precision of 1 *μm* on micromilled features. The final cost of the machine achieved the target cost of <$15k. The final cost/precision ratio was computed and found to provide an order of magnitude improvement over commercially available machines.

References

[1] Okazaki, Y., N. Mishima and K. Ashida, (2004). "Microfactory - Concept, History, and Developments." *Journal of Manufacturing Science and Engineering*, Vol. 126 pp. 837-845.

[2] Ehmann, K.F., D. Bourell, M.L. Culpepper, T.J. Hodgson, T.R. Kurfess, M. Madou, K. Rajurkar and R.E. Devor, (2004). "WTEC Report on International Assessment of Research and Development in Micromanufacturing." *World Technology Evaluation Center, Inc.*

[3] Dimov, S., D.T. Pham, A. Ivanov, K. Popov and K. Fansen, (2004). "Micromilling Strategies: Optimization Issues." *Proceedings of the Institution of Mechanical Engineers, Part B: Journal of Engineering Manufacture*, Vol. 218 No. (7): pp. 731-736.

[4] *Performance Microtool*. Cited 11/2009; Available from: *http://www.pmtnow.com*.

[5] Oberg, E., F.D. Jones, H.L. Horton and H.H. Ryffell, *Machinery's Handbook*. 2000, New York: Industrial Press.

[6] Carpenter, I.D. and P.G. Maropoulos, (2000). "Automatic tool selection for milling operations Part 1: cutting data generation." *Proceedings of the Institution of Mechanical Engineers*, Vol. 214 (Part B): pp. 271-282.

[7] Jun, M.B.G., R.E. Devor and S.G. Kapoor, (2006). "Investigation of the dynamics of microend milling - Part II: model validation and interpretation." *Journal of manufacturing science and engineering*, Vol. 128 pp. 901-912.

[8] Kim, C., J.R. Mayor and J. Ni, (2004). "A static model of chip formation in microscale milling." *Journal of Manufacturing science and engineering*, Vol. 126 pp. 710-718.

[9] Li, H.Z., X.P. Li and X.Q. Chen, (2003). "A novel chatter stability criterion for the modeling and simulation of the dynamic milling process in the time domain." *International Journal of Advanced Manufacturing technology*, Vol. 22 pp. 619-625.

[10] Lacerda, H.B. and V.T. Lima, (2004). "Evaluation of cutting forces and prediction of chatter vibrations in milling." *Journal of the Brazil Society of Mechanical Science & Engineering*, Vol. 26 No. (1): pp. 74-81.

[11] Insperger, T., J. Gradisek, M. Kalveram, G. Stepan, K. Winert and E. Govekar, (2006). "Machine tool chatter and surface location error in milling processes." *Journal of Manufacturing Science and Engineering*, Vol. 128 pp. 913-920.

[12] Liu, X., Devor, R.E., Kapoor, S.G., (2006). "An analytical model for the prediction of minimum chip thickness in micromachining." *Journal of Manufacturing Science and engineering*, Vol. 128 pp. 474-481.

[13] Dornfeld, D., S. Min and Y. Takeuchi, (2006). "Recent Advances in Mechanical Micromachining." *CIRP Annals - Manufacturing Technology*, Vol. 55 No. (2): pp. 745-768.

[14] Stoker, J.J., *Differential Geometry*. 1969, New York: Wiley-interscience.

[15] Sun, Y., J. Wang and D. Guo, (2006). "Guide curve based interpolation scheme of parametric curves for precision CNC machining." *International Journal of Machine Tools & Manufacture*, Vol. 46 No.: pp. 235-242.

[16] Li, R.Q., Y.H. Wang, Z.Y. Wu and Z.N. Chen, (2006). "Automatic generation of an NC machining tool-path for a 3D curve based on polar coordinates." *International Journal of advanced manufacturing technology*, Vol. 27 pp. 1119-1123.

[17] Zhang, C., P. Zhang and F. Cheng, (2001). "Fairing spline curves and surfaces by minimizing energy." *Computer-aided design*, Vol. 33 pp. 913-923.

[18] Tikhon, M., T.J. Ko, S.H. Lee and H.S. Kim, (2004). "NURBS interpolator for constant material removal rate in open NC machine tools." *International Journal of Machine Tools & Manufacture*, Vol. 44 pp. 237-245.

[19] Yang, M. and W. Hong, (2002). "Three-dimensional reference pulse linear and circular interpolators for CNC systems." *International Journal of Production Research*, Vol. 40 No. (2): pp. 425-439.

[20] Zeid, I., *Mastering CAD/CAM*. 2005, New York: McGraw Hill.

[21] Yau, H. and M. Kuo, (2001). "NURBS machining and feed rate adjustment for high-speed cutting of complex sculptured surfaces." *International Journal of Production Research*, Vol. 39 No. (1): pp. 21-41.

[22] Lo, C., (1999). "Real-time generation and control of cutter path for 5-axis CNC machining." *International Journal of Machine Tools & Manufacture*, Vol. 39 pp. 471-488.

[23] Park, J., S. Nam and M. Yang, (2005). "Development of a real-time trajectory generator for NURBS interpolation based on the two-stage interpolation method." *International Journal of Advanced Manufacturing technology*, Vol. 26 pp. 359-365.

[24] Nam, S. and M. Yang, (2004). "A study on a generalized parametric interpolator with real-time jerk-limited acceleration." *Computer-aided design*, Vol. 36 pp. 27-36.

[25] Erkorkmaz, K. and Y. Altintas, (2005). "Quintic Spline Interpolation With Minimal Feed Fluctuation." *Journal of Manufacturing Science and Engineering*, Vol. 127 pp. 338-349.

[26] Cheng, M.-Y., M.-C. Tsai and J.-C. Kuo, (2002). "Real-time NURBS command generators for CNC servo controllers." *International journal of machine tools & manufacture*, Vol. 42 pp. 801-813.

[27] Lartigue, C., F. Thiebaut and T. Maekawa, (2001). "CNC tool path in terms of B-spline curves." *Computer-aided design*, Vol. 33 pp. 307-319.

[28] Chuang, S.-H.F. and J.-L. Shih, (2006). "A novel approach for computing C2-continuous offset of NURBS curves." *International Journal of Advanced Manufacturing Technology*, Vol. 29 pp. 151-158.

[29] Fleisig, R.V. and A.D. Spence, (2001). "A constant feed and reduced angular acceleration interpolation algorithm for multi-axis machining." *Computer-aided design*, Vol. 33 pp. 1-15.

[30] Ren, Y. and Y. Lee, (2004). "Explicit Free-form curve interpolation and error analysis for NC machining of complex surface models." *Computer-Aided Design and Applications*, Vol. 1 No. (1-4): pp. 243-250.

[31] Wang, S., Yu, H., Liao, H., (2006). "A new high-efficiency error compensation system for CNC multi-axis machine tools." *International journal of advanced manufacturing technology*, Vol. 28 pp. 518-526.

[32] Yeh, S. and P. Hsu, (2002). "Adaptive-feedrate interpolation for parametric curves with a confined chord error." *Computer-aided design*, Vol. 34 pp. 229-237.

[33] Zhiming, X., C. Jincheng and F. Zhengjin, (2002). "Perfomance evaluation of a real-time interpolation algorithm for NURBS curves." *International Journal of Advanced Manufacturing Technology*, Vol. 20 pp. 270-276.

[34] Farouki, R.T. and Y. Tsai, (2001). "Exact taylor series coefficients for variable-feedrate CNC curve interpolators." *Computer-aided design*, Vol. 33 pp. 155-165.

[35] Tsai, Y., R.T. Farouki and B. Feldman, (2001). "Performance analysis of CNC interpolators for time-dependent feedrates along PH curves." *Computer aided geometric design*, Vol. 18 pp. 245-265.

[36] Yong, T. and R. Narayanaswami, (2003). "A parametric interpolator with confined chord errors, acceleration and deceleration for NC machining." *Computer-aided design*, Vol. 35 pp. 1249-1259.

[37] Phillip, A.G., S.G. Kapoor and R.E. Devor, (2006). "A new acceleration-based methodology for micro/meso-scale machine tool performance evaluation." *International journal of machine tools & manufacture*, Vol. 46 pp. 1435-1444.

[38] Tutunea-Fatan, O.R. and H. Feng, (2005). "Determination of geometry-based errors for interpolated tool paths in five-axis surface machining." *Journal of manufacturing science and engineering*, Vol. 127 pp. 60-67.

[39] Liang, H., H. Hong and J. Svoboda, (2002). "A combined 3D linear and circular interpolation technique for multi-axis machining." *Journal of manufacturing science and engineering*, Vol. 124 pp. 305-312.

[40] Jun, M.B.G., X. Liu, R. DeVor and S.G. Kapoor, (2006). "Investigation of the dynamics of microend milling - Part I: model development." *Journal of manufacturing science and engineering*, Vol. 128 pp. 893-900.

[41] Borisavljevic, A., M.H. Kimman, P. Tsigkourakos, H. Polinder, H.H. Langen, R.M. Schmidt and J.A. Ferreira, (2009). "Motor Drive for a Novel High-Speed Mico-Milling Spindle." *2009 IEEE/ASME International Conference on Advanced Intelligent Mechatronics*, Vol. 1492-7

[42] Zwyssig, C., J.W. Kolar and S.D. Round, (2009). "Megaspeed Drive Systems: Pushing Beyond 1 Million r/min." *IEEE/ASME Transactions on Mechatronics*, Vol. 14 No. (5): pp. 564-574.

[43] Chen, Y.S., C.C. Chiu and Y.D. Cheng, (2009). "Dynamic Analysis of Disc Spring Effects on the Contact Pressure of the Collet-Spindle Interface in a High-Speed Spindle System." *Proceedings of the Institution of Mechanical Engineers, Part C: Journal of Mechanical Engineering Science*, Vol. 223 No. (5): pp. 1191-1201.

[44] Kosmynin, A.V., V.S. Shchetinin and I.A. Ivanova, (2009). "Using Magnetic Force in the Gas-Static Bearings of High-Speed Spindles." *Russian Engineering Research*, Vol. 29 No. (5): pp. 456-458.

[45] Liu, X., R.E. DeVor and S.G. Kapoor, (2007). "Model-Based Analysis of the Surface Generation in Microendmilling - Part I: Model Development." *Journal of Manufacturing Science and Engineering*, Vol. 129 pp. 453-460.

[46] Cheng, C.W. and M.C. Tsai, (2004). "Real-time variable feed rate NURBS curve interpolator for CNC machining." *International Journal of Advanced Manufacturing Technology*, Vol. 23 pp. 865-873.

[47] Borisavljevic, A., M.H. Kimman, P. Tsigkourakos, H. Polinder, H.H. Langen, R.M. Schmidt and J.A. Ferreira, (2009). "Motor Drive for a Novel High-Speed Micro-Milling Spindle," in *2009 IEEE/ASME International Conference on Advanced Intelligent Mechatronics*. 2009: Singapore.

[48] Zwyssig, C., M. Duerr, D. Hassler and J.W. Kolar, (2007). "An Ultra-High-Speed, 500000 rpm, 1kW Electric Drive System," in *Fourth Power Conversion Conference*. 2007. p. 1577-1583.

[49] Sreeram, S., A.S. Kumar, M. Rahman and M.T. Zaman, (2006). "Optimization of Cutting Parameters in Micro End Milling Operations Under Dry Cutting Conditions Using Genetic Algorithms." *International Journal of Advanced Manufacturing technology*, Vol. 30 pp. 1030-1039.

[50] Boothroyd, G., *Fundamentals of Metal Machining and Machine Tools*. 1975, Washington, D.C.: Scripta Book Company.

[51] *NSK America*. Cited 09/2008; Available from: http://www.nskamericacorp.com/pdf2/e800.pdf.

[52] Bourne, K.A., M.B.G. Jun, S.G. Kapoor and R.E. DeVor, (2008). "An Acoustic Emission-Based Method for Determining Contact Between a Tool and Workpiece at the Microscale." *Journal of Manufacturing Science and Engineering*, Vol. 130 No. (3): pp. 0311011-0311018.

[53] Prakash, J.R.S., M. Rahman, K.A. Senthil and S.C. Lim, (2002). "Model for predicting tool life in micromilling of copper." *Chinese Journal of mechanical engineering*, Vol. 15 pp. 115-120.

[54] Bourne, K., R.E. Devor and S.G. Kapoor, (2006). "Determining Cutting Tool Dimensions and Run-Out Using Acoustic Emissions." No. (EP20060126222).

[55] Benavides, G.L., D.P. Adams and P. Yang, (2001). "Meso-Machining Capabilities." *Sandia Report*

[56] Gandarias, E., S. Dimov, D.T. Pham, A. Ivanov, K. Popov, R. Lizarralde and P.J. Arrazola, (2005). "New Methods for Tool Failure Detection in Micromilling." *Proceedings of the Institution of Mechanical Engineers, Part B: Journal of Engineering Manufacture*, Vol. 220 No. (2): pp. 137-144.

[57] *Atometric, Inc.* Cited 09/2008; Available from: http://www.atometric.com/.